

JAMS

**JOURNAL OF
ASSOCIATED MEDICAL SCIENCES**

Volume 51 Number 3 September-December 2018 E-ISSN: 2539-6056



Journal of Associated Medical Sciences

Aims and scope

The Journal of Associated Medical Sciences belongs to Faculty of Associated Medical Sciences (AMS), Chiang Mai University, Thailand. The journal specifically aims to provide the platform for medical technologists, physical therapists, occupational therapists, radiologic technologists, speech-language pathologists and other related professionals to distribute, share, discuss their research findings, inventions, and innovations in the areas of:

1. Medical Technology
2. Physical Therapy
3. Occupational Therapy
4. Radiologic Technology
5. Communication Disorders
6. Other related fields

Submitted manuscripts within the scope of the journal will be processed strictly following the double-blinded peer review process of the journal. Therefore, the final decision can be completed in 1-3 months average, depending on the number of rounds of revision.

Objectives

The Journal of Associated Medical Sciences aims to publish integrating research papers in areas of Medical Technology, Physical Therapy, Occupational Therapy, Radiologic Technology, and related under peer-reviewed via double-blinded process by at least two internal and external reviewers.

Types of manuscript

Manuscripts may be submitted in the form of review articles, original articles, short communications, as an approximate guide to length:

- **Review articles** must not exceed 20 journal pages (not more than 5,000 words), including 6 tables/figures, and references (maximum 75, recent and relevant).
- **Original articles** must not exceed 15 journal pages (not more than 3,500 words), including 6 tables/figures, and 40 reference (maximum 40, recent and relevant).
- **Short communications** including technical reports, notes, and letters to the editor must not exceed 5 journal pages (not more than 1,500 words), including 2 tables/figures, and references (maximum 10, recent and relevant).

Peer review process

By submitting a manuscripts to Journal of Associated Medical Sciences, the authors agree to subject it to the confidential double-blinded peer-review process. Editors and reviewers are informed that the manuscripts must be considered confidential. After a manuscripts is received, it is assigned by a specific Associate Editor. The Associate Editor prepares a list of expert reviewers, which may include some suggested by the Editor-in-Chief. Authors can indicate specific individuals whom they would like to have excluded as reviewers. Generally, requests to exclude certain potential reviewers will be honored except in fields with a limited number of experts. All potential reviewers are contacted individually to determine availability. Manuscripts files are sent to at least two expert reviewers. Reviewers are asked to complete the review of the manuscripts within 2 weeks and to return a short review form. Based on the reviewers' comments, the Associate Editor recommends a course of action and communicates the reviews and recommendations to the Editor-in-Chief for a final decision.

The Associate Editor considers the comments made by the reviewers and the recommendation of the Editor-in-Chief, selects those comments to be shared with the authors, makes a final decision concerning the manuscripts, and prepares the decision letter for signature by the Editor-in-Chief. If revisions of the manuscripts are suggested, the Associate Editor also recommends who should review the revised paper when resubmitted. Authors are informed of the decision by e-mail; appropriate comments from reviewers and editors are appended.

Publication frequency

Journal of Associated Medical Sciences publishes 3 issues a year

Issue 1: January-April

Issue 2: May-August

Issue 3: September-December

Editor-in-Chief

Preeyanat Vongchan	Chiang Mai University	Thailand
--------------------	-----------------------	----------

Associate Editor

Thanusak Tatu	Chiang Mai University	Thailand
Suchart Kothan	Chiang Mai University	Thailand
Supaporn Chinchai	Chiang Mai University	Thailand
Araya Yankai	Chiang Mai University	Thailand

Editorial Board

Cecilia Li-Tsang	Hong Kong Polytechnic University	Hong Kong
Christopher Lai	Singapore Institute of Technology	Singapore
Clare Hocking	Auckland University of Technology	New Zealand
Darawan Rinchai	Sidra Medicine	Qatar
David Man	Hong Kong Poly Technic University	Hong Kong
Elizabeth Wellington	University of Warwick	United Kingdom
Ganjana Lertmemongkolchai	Khon Kaen University	Thailand
Goonnapa Fucharoen	Khon Kaen University	Thailand
Hans Bäumlér	Universitätsmedizin Berlin	German
Hong Joo Kim	Kyungpook National University	South Korea
Jourdain Gonzague	French National Research Institute for Sustainable Development (IRD)	France
Kesara Na Bangchang	Thammasart University	Thailand
Leonard Henry Joseph	University of Brighton	United Kingdom
Marc Lallemand	Drugs for Neglected Diseases Initiative (DNDi)	Switzerland
Nicole Ngo-Glang-Huang	French National Research Institute for Sustainable Development (IRD)	France
Prawit Janwantanakul	Chulalongkorn University	Thailand
Roongtiwa Vachalathiti	Mahidol University	Thailand
Rumpa Boonsinsukh	Srinakharinwirot University	Thailand
Sakorn Pornprasert	Chiang Mai University	Thailand
Sophie Le Coeur	French Institute for Demographic Studies (INED)	France
Srijit Das	Universiti Kebangsaan Malaysia	Malaysia
Supan Fucharoen	Khon Kaen University	Thailand
Thanaporn Tunprasert	University of Brighton	United Kingdom
Tengku Shahrul Anuar	Universiti Teknologi MARA	Malaysia
Timothy R. Cressey	French National Research Institute for Sustainable Development (IRD)	France
Valerie Wright-St Clair	Auckland University of Technology	New Zealand
Witaya Mathiyakom	University of Southern California	United States of America

Business manager

Rungtiwa Mongkolkerd

Treasurer

Angsumalee Srithiruen

Webpage Administrative Staff

Tapapol Camnoi

Tippawan Sookruay

Prompong Chaiwong

Nopporn Phuangsombat

Journal Impact Factor

The journal's 2017 Impact Factor is 0.237

Journal website

Homepage <https://www.tci-thaijo.org/index.php/bulletinAMS/index>

Journal E-ISSN:

2539-6056

Editorial Office

Faculty of Associated Medical Sciences, Chiang Mai University
110 Inthawaroros Road, Suthep, Muang, Chiang Mai, 50200
Phone 053 935072 Facsimile 053 936042

Disclaimer

Personal views expressed by the contributors in their articles are not necessarily those of the Journal of Associated Medical Sciences, Faculty of Associated Medical Sciences, Chiang Mai University.

Content

- 119** Effect of diagnostic medical X-rays in the range of 50 keV up to 100 keV of energy on ferrous sulfate solution with saturated O₂ gas: preliminary study
*Montree Tungjai** *Apinai Sukpor* *Suchart Kothan* *Suratchanee Phadngam*
- 122** Preliminary study for the prevalence and causes of anemia in pregnant women attending an Antenatal Care Unit in different periods of gestation
Wararat Thongperm¹ *Mantana Chaisen²* *Yuttana Chunchom²* *Supakit Aeduldecha²* *Orawan Saraku^{2*}*
- 128** X-ray scatter correcting methods for digital radiographic imaging
*Hudsaleark Neamin**
- 138** Dosimetric validation of the eclipse Acuros XB dose calculation algorithm for a 6 MV photon beams
Taweap Sanghangthum^{1}* *Yot Phimmakone²* *Sivalee Suriyapee¹*
- 150** Comparison of post processing methods between Java Magnetic Resonance User Interface (jMRUI) and Totally Automatic Robust Quantitation in NMR (TARQUIN) software for liver fat quantification
Duanghathai Pasanta¹ *Montree Tungjai¹* *Sirirat Chancharunee²* *Suchart Kiatwattanacharoen¹* *Suchart Kothan^{1*}*
- 157** Quantification of hepatitis B virus (HBV) DNA and HBV genotyping simultaneously in plasma using real-time polymerase chain reaction
Wootichai Khamduang^{1,2,3}* *Amonrat Pota¹* *Wanvisa Khamlasai¹* *Sayamon Hongjaisee^{1,4}*
Nicole Ngo-Giang-Huong^{1,2} *Wasna Sirirungsri^{1,3}*
- 163** Antioxidant and anti-inflammatory activities of macerated herbal oil in dental pulp cells
Fahsai Kantawong^{1}* *Sutinee Mungkala¹* *Sawinee Tamang¹* *Ruthairat Manaphan¹*
Pichaporn Thaweean¹ *Phenphichar Wanachantararak²*
- 171** Bacterial contamination and their tolerance in banknotes and coins surrounding the area of Chiang Mai University Hospital in Chiang Mai Province
Ponrut Phunpae^{1,3}* *Chanjuti Sriruan¹* *Ratchadaporn Udpaun¹* *Santhana Buamongkol¹* *Sudjai Pawichai¹*
Autchar Ruangpayuk² *Watchawan Chairuangwut¹*

Effect of diagnostic medical X-rays in the range of 50 keV up to 100 keV of energy on ferrous sulfate solution with saturated O₂ gas: preliminary study

Montree Tungjai* Apinai Sukpor Suchart Kothan Suratchanee Phadngam

Department of Radiologic Technology, Faculty of Associated Medical Sciences Chiang Mai University, Chiang Mai, Thailand.

ARTICLE INFO

Article history:

Received 27 April 2018

Accepted as revised 18 July 2018

Available online 18 July 2018

Keywords:

Radiation, Radiation exposure, Diagnostic medical X-rays

ABSTRACT

Background: Ferrous sulfate solution is the most widely used as an aqueous chemical dosimeter. In this preliminary present study, we applied ferrous sulfate solution in diagnostic radiology.

Objectives: The aim of preliminary present study was to measure absorbance spectrum of ferrous sulfate solution after exposure to diagnostic medical X-rays in the range of 50 keV up to 100 keV of energy.

Materials and methods: Diagnostic medical X-rays were generated by a medical X-ray machine. Radiation exposure was measured by mean of ionization chamber. Ferrous sulfate sulfate solution with saturated O₂ gas was irradiated, resulting in ferric ion production in solution. The optical density of irradiated ferrous sulfate solution was determined by spectrophotometer.

Results: A positive correlation was shown in diagnostic medical X-ray energy with radiation exposure. The optical density at a wavelength of 304 nm was increased as a function of X-ray energy.

Conclusion: This preliminary finding suggested that ferrous sulfate solution with saturated O₂ gas showed feasibility to measure radiation dose of diagnostic medical X-rays at 50-100 keV of energy.

Introduction

There are various methods used to measure radiation dosages including air-filled detectors such as Geiger counters and ionization chambers. Solid detectors make use of thermal luminescence detection (TLD) and optically stimulated luminescence (OSL). Such methods are commonly used in radiation measurement due to ease of use compared with chemical or biological systems. However, those methods can be difficult to apply in determining absorbed dose in soft tissue. Consequently, chemical dosimeters are used when absorbed dosages in soft tissue must be determined.

If a chemical dosimeter is constituted of an aqueous solution, it can be predicted that radiation will have a major interaction with water.^{1,2} Moreover, aqueous solutions can be made to fill every variability in the shape of the volume.³

Ferrous sulfate solution is the most widely used as an aqueous chemical dosimeter. Ferrous ion (Fe²⁺) is oxidized to ferric ion (Fe³⁺) by a free radical. This free radical is generated when ionizing radiation deposits energy to solution.⁴ There were several reports mentioned the use of ferrous sulfate solution in measuring radiation dosages.⁵⁻¹⁰ However, these radiation dosages were high radiation energy type or used monochromatic energy. In this preliminary present study, we applied ferrous sulfate solution in diagnostic radiology. The aim of preliminary present study was to measure optical density of ferrous sulfate solution with saturated O₂ gas after exposure to diagnostic medical X-rays in the range of 50 keV up to 100 keV of energy.

* Corresponding author.

Author's Address: Department of Radiologic Technology,
Faculty of Associated Medical Sciences Chiang Mai University,
Chiang Mai 50200 Thailand

** E-mail address: mtungjai@gmail.com

doi: 10.14456/jams.2018.16

E-ISSN: 2539-6056

Materials and methods

Diagnostic medical X-ray generator used is a diagnostic medical X-ray machine (Quantum Medical Imaging, High frequency series™ X-ray Generator 125 kVp, 400 mA) at Department of Radiologic Technology, Faculty of Associated Medical Sciences, Chiang Mai University. This X-ray machine needed to be able to generate several energies of X-rays by adjusting the kilovoltage peak (kVp) setting (Figure 1). Other equipment included a multichannel analyzer (Detector XR-100T-CdTe, Amptek), an ionization chamber (Capintec), barometer, and thermometer. Hydrochloric acid (HCl), sulfuric acid (H₂SO₄), and ferrous ammonium sulfate were the materials used in this study.

Determination of X-ray spectrum

A multichannel analyzer (MCA) was placed perpendicular to the central axis of radiation beam at a distance of 100 cm from X-ray tube. X-ray spectrum was recorded on 50 keV up to 100 keV (100 mAs) of X-ray energy.

Ferrous sulfate solution with saturated O₂ gas

A ferrous sulfate solution contained 1 mM ferrous ammonium sulfate in 0.4 M H₂SO₄, 0.01 M HCl and was saturated with O₂ gas. Solution was prepared using water redistilled in a flask from 1x10⁻⁴ M potassium permanganate solution. All glasses were heated at 100 °C for 6 hours before being used. Ferrous sulfate solution was placed perpendicular to the central axis of radiation beam at distance of 100 cm from the X-ray tube. The irradiated ferrous sulfate solution produced ferric ion in solution. The optical density of irradiated ferrous sulfate solution was determined by spectrophotometer (Agilent 8453).

Measurement of radiation exposure by ionization chamber

Ionization chamber was placed perpendicular to the central axis of radiation beam at a distance of 100 cm from X-ray tube. Radiation exposure was recorded in nanocoulomb (nC). Pressure and temperature at experimental room also was recorded for correcting radiation exposure values.

Statistical analysis

An origin lab program was used for data analysis. Linear correlation analysis was carried out using Pearson correlation. Simple regression analysis was also used for analyzing data.

Results and Discussions

Diagnostic medical X-ray spectra of X-ray energy at 50 keV up to 100 keV (100 mAs) is showed in Figure 1. These X-rays shows continuous spectra that related to previously our report.¹¹

An optical density of ferric ion produced after X-ray irradiation against diagnostic medical X-ray energy is showed in Figure 2. The optical density at a wavelength of 304 nm was increased as a function of X-ray energy. A quantity of ferric ion produced depends on the radiation energy absorbed by ferrous sulfate solution.¹² It seems reasonable that if quantity of ferric ion produced was increased when radiation energy increased, then absorbed dosage would also have increased when radiation energy increased, as well.

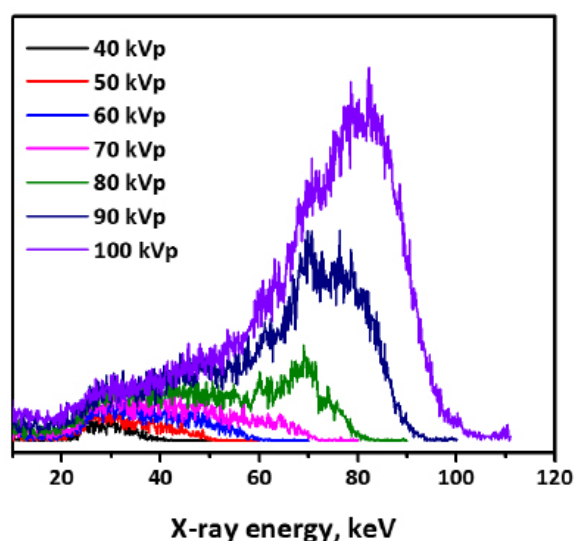


Figure 1. Diagnostic medical X-ray spectra of X-ray energy at 50 - 100 keV (100 mAs).

Radiation exposure against diagnostic medical X-ray energy is showed in Figure 3. Radiation exposure was increased when X-ray energy increased (Pearson's $r=0.992$, $R^2=0.980$). High radiation energy can produce ionization in medium, resulting in radiation exposures that are high.¹³

However, a ferrous sulfate solution was used to measure low energy X-ray dose.¹⁴ In addition, the ferrous sulfate solution could enhance response by added a radiosensitizer under X-ray irradiation.¹⁵ In conclusion, this preliminary finding suggested that the ferrous sulfate solution showed feasibility for use in diagnostic radiology. However, further development and study of it are needed to fully determine feasibility.

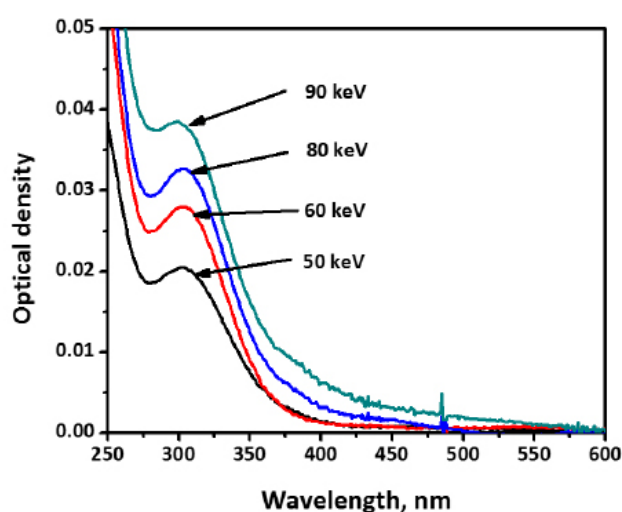


Figure 2. An spectra of ferric ion produced after X-ray irradiation against diagnostic medical X-ray energy.

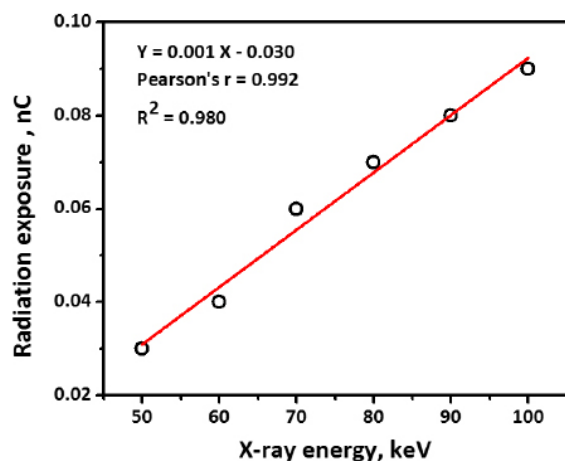


Figure 3. Radiation exposures against diagnostic medical X-ray energy.

Acknowledgements

We would like to thank the Department of Radiologic Technology, Faculty of Associated Medical Sciences, Chiang Mai University, Thailand for allowing us to use of all facilities, and truly appreciate their support throughout this study.

Conflict of interest

None.

References

- [1] Rahn RO, Gerstenberg HM, Vavrina GA. Dosimetry of ionizing radiation using an iodide/iodate aqueous solution. *Appl Radiat Isot.* 2002; 56(3): 525-34.
- [2] Waqar M, Ul-Haq A, Bilal S, Masood M. Comparison of dosimeter response of TLD-100 and ionization chamber for high energy photon beams at KIRAN Karachi in Pakistan. *The Egyptian Journal of Radiology and Nuclear Medicine.* 2017; 48(2): 479-83.
- [3] Miljanić S, Ražem D. The effects of size and shape of the irradiation vessel on the response of some chemical dosimetry systems to photon irradiation. *Radiat Phys Chem.* 1996; 47(4): 653-62.
- [4] Klassen NV, Shortt KR, Seuntjens J, Ross CK. Fricke dosimetry: the difference between $G(\text{Fe}^{3+})$ for ^{60}Co gamma-rays and high-energy x-rays. *Phys Med Biol.* 1999; 44(7): 1609-24.
- [5] de Almeida CE, Ochoa R, Lima MC, David MG, Pires EJ, Peixoto JG, et al. A feasibility study of Fricke dosimetry as an absorbed dose to water standard for Ir HDR sources. *PLoS One.* 2014; 9(12): e115155.
- [6] Malathi N, Sahoo P, Praveen K, Murali N. A novel approach towards development of real time chemical dosimetry using pulsating sensor-based instrumentation. *J Radioanal Nucl Chem.* 2013; 298(2): 963-72.
- [7] Moussous O, Khoudri S, Benguerba M. Characterization of a Fricke dosimeter at high energy photon and electron beams used in radiotherapy. *Australas Phys Eng Sci Med.* 2011; 34(4): 523-8.
- [8] Himit M, Itoh T, Endo S, Fujikawa K, Hoshi M. Dosimetry of mixed neutron and gamma radiation with paired Fricke solutions in light and heavy water. *J Radiat Res.* 1996; 37(2): 97-106.
- [9] Watanabe R, Usami N, Kobayashi K. Oxidation yield of the ferrous ion in a Fricke solution irradiated with monochromatic synchrotron soft X-rays in the 1.8-10 keV region. *Int J Radiat Biol.* 1995; 68(2): 113-20.
- [10] Juárez-Calderón JM, Negrón-Mendoza A, Ramos-Bernal S. Irradiation of ferrous ammonium sulfate for its use as high absorbed dose and low-temperature dosimeter. *Radiat Phys Chem.* 2007; 76(11): 1829-32.
- [11] Tungjai M, Dechsupa N. Assessment of mobile lipids with $^1\text{H-NMR}$ spectroscopy in enriched CD34+ human peripheral blood stem cells/progenitor cells after exposure to polyenergetic medical diagnostic x-rays. *IJABME.* 2014; 7(1): 61-5.
- [12] Schreiner LJ. Review of Fricke gel dosimeters. *Journal of Physics: Conference Series.* 2004;3(1):9.
- [13] Kothan S, Tungjai M. An estimation of x-radiation output using mathematic model. *American Journal of Applied Sciences.* 2011; 8(8): 839-42.
- [14] Austerlitz Cd, Souza V, Villar HP, Cordilha A. The use of fricke dosimetry for low energy x-rays. *Braz Arch Biol Technol.* 2006; 49: 25-30.
- [15] Austerlitz C, Souza VLbd, Campos DMT, Kurachi C, Bagnato V, Sibata C. Enhanced response of the fricke solution doped with hematoporphyrin under X-rays irradiation. *Braz Arch Biol Technol.* 2008; 51: 271-9.

Preliminary study for the prevalence and causes of anemia in pregnant women attending an Antenatal Care Unit in different periods of gestation

Wararat Thongperm¹ Mantana Chaisen² Yuttana Chunchom² Supakit Aueduldecha² Orawan Sarakul^{2*}

¹Department of Medical Technology, Nayong Hospital, Nayong, Trang, Thailand

²School of Allied Health Sciences, Walailak University, Nakhonsithammarat, Thailand

ARTICLE INFO

Article history:

Received 14 February 2018

Accepted as revised 13 June 2018

Available online 4 August 2018

Keywords:

Anemia, pregnancy, iron deficiency, thalassemia

ABSTRACT

Background: One of common complications of pregnancy is an anemia which is effected by various causes. Anemia can develop throughout the pregnancy period and increase in severity upon the gestation times. WHO recommends all pregnant women should attend an antenatal care (ANC) unit in the first trimester of gestation for healthy promotion and complication prevention during pregnancy and after birth.

Objectives: The aim of this preliminary study is to find out the prevalence and causes of anemia in pregnant women who start attending an ANC program at different time points of gestation.

Materials and methods: Cross-sectional study was performed during May 2015 -February 2016. Hematological parameters were examined in all 190 pregnant women attended the ANC unit at Nayong Hospital. Participants were divided into three groups according to period of gestation at the first time of ANC admission. Serum ferritin, thalassemia screening, and hemoglobin typing were determined in anemia cases to analyze causes of anemia. Prevalence of anemia at each time point ANC attended groups were calculated. Mann-Whitney U test was used to compare the different of parameters between the groups.

Results: Prevalence of anemia in all attended pregnant women was 22.1%. According to the period of gestation at the first time of ANC admission, the prevalence of anemia was 17.2% (15 of 87) at the first trimester group, 22.5% (20 of 89) at the second trimester, and 50.0% (7 of 14) at the third trimester group. Levels of hemoglobin and hematocrit of the second and the third groups were significantly different from the first trimester group with $p < 0.05$. MCHC of the third trimester group showed significantly different from both the first and second trimester groups, $p < 0.05$. Causes of anemia were thalassemia/abnormal hemoglobin carriers in 11 cases (5.8%), Iron deficiency anemia (IDA) in 10 cases (5.3%), IDA with thalassemia/abnormal hemoglobin carriers in 6 cases (3.2%), and anemia with other causes in 15 cases (7.9%). For thalassemia cases, HbE trait without α -thalassemia had the highest prevalence (44.4%). There were two cases of severe anemia, which were Hb H-CS disease and IDA.

* Corresponding author.

Author's Address: School of Allied Health Sciences,
Walailak University, Nakhonsithammarat, Thailand

** E-mail address: sorawan@mail.wu.ac.th

doi: 10.14456/jams.2018.17

E-ISSN: 2539-6056

Conclusion: Prevalence of anemia in pregnant women in this presentation was still high and increased throughout the period of gestation. Causes of anemia, such as IDA, can be prevented by early attention to an ANC unit. The promotion

of an ANC program for married couples and adolescent women should be considered to improve maternal and fetal health quality during pregnancy and after-birth.

Introduction

Anemia is a common complication during pregnancy. In 2011, World Health Organization (WHO) reported the prevalence of anemia in pregnant women to be about 41.8% worldwide, which is a higher rate than non-pregnant women.¹ In Thai population, the prevalence of anemia in pregnant women was still high.¹⁻³ Consistent studies had been reported in many areas.^{4, 5} Physiology changed during pregnancy and the increasing requirement of nutrients for red blood cell (RBC) production, both for mother and fetus, leads to anemia in insufficient nutrients taken for the mother.⁸⁻¹² Iron is the main component of RBC and a lack of iron can cause iron deficiency anemia (IDA). IDA is the most common cause of nutrient deficiency anemia in all ages. In pregnant women, at least half of anemia is caused by IDA. During pregnancy, the average amount of iron requirement is about 1200 mg or 4.4 mg/day, of which 450 mg can be used for the mother, about 350 mg for fetus development and 250 mg is lost via the digestion tract.⁹ As the requirement is increased upon the period of gestation, the prevalence of anemia is elevated in the last trimester of gestation. Thalassemia is another cause of anemia in pregnant women.¹¹ About 60% of the Thai population are thalassemia/abnormal hemoglobin carriers.¹⁰ Mothers carrying thalassemic/abnormal hemoglobin genes may have anemia during pregnancy. In high risk couples, meaning parents both carrying the same thalassemic/abnormal genes, the baby will have thalassemic and hemoglobinopathic diseases. There are three types of severe thalassemia diseases in Thailand: homozygous α -thalassemia-1, homozygous β -thalassemia and β -thalassemia/hemoglobin E disease, which are controlled for reducing incidences. These severe types can cause complications for the mother during pregnancy and also affect the fetus development.^{11, 13}

WHO recommends all pregnant women should attend an antenatal care (ANC) unit, which provides a program for the prevention and treatment of health problems throughout the pregnancy. Because of the severity of complications being high risk in the later period of pregnancy, all pregnant women should be screened and prevented for possible complications early on. The full course of ANC consists of attending four times with the first time during 8-12 weeks or the first trimester of gestation.¹⁴ The supplement of necessary nutrients, such as folic acid and iron, will be given to support the increase in demand during pregnancy and reduce the risk of low birth weight, maternal anemia and iron deficiency. Thalassemia risked couples should attend a genetic counseling process and prenatal diagnosis for information acknowledgement about the disease. Thus, an ANC is useful for complications prevention and to improve the quality of the pregnancy throughout the gestation and after delivery. However, anemia is still a common problem in pregnancy and lots of pregnant women are

not concerned about the suitable time for ANC attention. This preliminary study aims to find out the prevalence and causes of anemia in pregnant women who attended an ANC program at different time points of gestation. The data will be informatively used for all pregnant women about anemia and the importance of ANC programs.

Materials and methods

1. Participants and data collection

This study is a cross-sectional study. The subjects were 190 pregnant women, who attended Nayong Hospital in Trang Province, Thailand from May 2015 - February 2016. Period of gestation at the first time of ANC unit submitted and general data was recorded by Laboratory Division of the hospital. This study was approved by the Board of Committee on Ethics, Walailak University, Thailand (No. 15/041). Pregnant women were divided into three groups based on period of gestation at the first time of hospital submission. Group I was 1-12 weeks of gestation, first trimester. Group II was 13-27 weeks of gestation, second trimester, and Group III was 28-40 weeks of gestation, third trimester. Participants with incomplete data were excluded.

2. Hematological parameters and serum ferritin

Blood samples at the first time of hospital submission were collected for hematological parameters testing using a Mindray BC5300 hematology analyzer (Shenzhen, China). Hematological parameters included RBC count (RBC), hemoglobin (Hb), hematocrit (Hct), mean corpuscular volume (MCV), mean corpuscular hemoglobin (MCH), mean cell hemoglobin concentration (MCHC), and red cell distribution width (RDW) results from the hospital were analyzed for anemia evaluation. Serum ferritin (SF) was also tested in anemic cases for iron deficiency determination using the immunologic method, VITROS ECI/ECiQ Immunodiagnostic Systems (Ortho-Clinical Diagnostics, Inc, New York, United States). Hb less than 11 g/dL for the first and third trimester, less than 10.5 g/dL for the second trimester, was defined as anemia.⁷ 15 SF<12 μ g/L with anemia was defined as IDA.¹³ The severity of anemia was categorized as following: mild, Hb 10.0-10.9 g/dl for the first and third trimester and 10.0-10.5 g/dL for the second trimester, moderate, Hb 7.0-9.9 g/dL and severe, Hb<7.0 g/dL.^{6, 13}

3. Thalassemia screening and hemoglobin typing

Thalassemia/abnormal hemoglobin were further studied in pregnant women who had anemia. MCV and dichlorophenol indophenol precipitation (DCIP) were used as the screening tests for Thalassemia/abnormal hemoglobin and hemoglobin E, respectively. Hemoglobin typing was performed by the HPLC technique VARIANT II (Biorad, California, USA) in subjects who had MCV<80 fL and/or DCIP positive. The types and % of hemoglobin were used for

thalassemia classification as described previously.¹⁶ The α -thalassemia was determined by PCR method.

4. Statistical analysis

Data was determined for normality of the distribution using the Kolmogorov-Smirnov test. The difference in parameters between groups was analyzed by the Mann-Whitney U Test. The p value of less than 0.05 was considered significant.

Results

General data

The study included 190 pregnant women who attended

the ANC unit of the hospital. Participants were divided into 3 groups based on period of gestation at the first ANC submission. Number and time of gestation of each group are shown in Table 1. Group I, II and III had 87, 89 and 14 cases, respectively. The average ages of groups I, II, and III were 29.7 ± 9.0 , 25.3 ± 7.1 and 25.2 ± 7.8 years old, respectively. Seventy-six cases (40%) were in the second time of gestation. Another 31.1%, 17.9% and 11.1% of all pregnant women were in the first, third and over 3 times of gestation, respectively.

Table 1 Summarized of 190 cases in total; period of gestation at the first time of ANC registration and times of current gestation.

Period of gestation	Age* (years)	Times of gestation (n)			
		1	2	3	>3
1 st trimester (n=87)	29.7 ± 9.0	27	39	14	7
2 nd trimester (n=89)	25.3 ± 7.1	28	32	18	11
3 th trimester (n=14)	25.2 ± 7.8	4	5	2	3
Total	190	59	76	34	21

* mean \pm SD.

Hematological parameters

At the first time of ANC submission, complete blood count was analyzed for anemia diagnosis. Hb levels of the pregnant women in the first, second, and third trimesters were 12.1 (6.3-15.7), 11.3 (6.7-14.2), and 10.8 (9.2-12.6) g/dL, respectively. Hematocrit levels were 36.0% (22.0-46.1%),

33.3% (24.2-42.0%), and 33.8% (28.8-36.8%) in first, second, and third trimester groups, respectively. The results showed that RBC, Hb, Hct and MCHC between of group I and III were significantly different with $p < 0.05$. Only Hb and Hct showed significantly different between group I and II, $p < 0.05$ (Table 2).

Table 2 Hematological parameters of pregnancy attended the first ANC in different period of gestation.

Period of gestation	RBC (X10 ⁶ / μ L)	Hb (g/dL)	Hct (%)	MCV (fL)	MCH (pg)	MCHC (g/dL)	RDW (%)
1 st trimester (n=87)	4.23 (2.99-5.35)	12.1 (6.3-15.7)	36.0 (22.0-46.1)	85 (58-93)	28.9 (17.7-32.9)	33.9 (28.7-36.0)	12.6 (11.1-26.0)
2 nd trimester (n=89)	4.12 (3.21-5.54)	11.3 ^a (6.7-14.2)	33.3 ^a (24.2-42.0)	85 (53-97)	28.4 (15.5-33.9)	33.7 (27.7-35.6)	12.9 (11.3-25.2)
3 th trimester (n=14)	3.90 ^a (3.53-4.78)	10.8 ^a (9.2-12.6)	33.8 ^a (28.8-36.8)	86 (71-96)	27.8 (22.0-32.8)	32.6 ^{a, b} (30.9-34.5)	12.8 (12.0-18.3)

Data were shown in median (minimum – maximum).

^{a, b} Significantly difference from the 1st and 2nd trimester groups, respectively (Mann-Whitney U test, $p < 0.05$)

Anemia and causes

Participants with anemia accounted for 42 cases in total with a prevalence of 22.1%, which consisted of 11 thalassemia/abnormal haemoglobin carrier cases (5.8%), 10 IDA cases (5.3%), 6 IDA with thalassemia/abnormal haemoglobin carrier cases (3.2%), and 15 anemia with other causes cases (7.9%), as shown in Table 3. The prevalence of anemia was 17.2% (15 of 87 cases) in the first trimester group, 22.5% (20 of 89) in the second trimester, and 50.0% (7 of 14 cases) in the third trimester group. In all anemia subjects, serum ferritin was examined for IDA diagnosis.

MCV and DCIP were used for thalassemia and abnormal haemoglobin screening and confirmed by haemoglobin typing. The results showed an increasing of IDA was upon the period of gestation (Table 3). There were 10 cases of IDA in total, consisting of 3 of 87 cases (3.4%), 5 of 89 cases (5.6%) and 2 of 14 cases (14.3%) in groups I, II and III, respectively. IDA with thalassemia/abnormal haemoglobin carrier was found in 6 cases. Anemia with other causes had 15 cases (7.9%), consisting of 6 cases (6.9%), 8 cases (9.0%) and 1 case (7.1%) in groups I, II and III, respectively. The severity of anemia is categorized by the level of Hb,

as defined in Table 3. There were 35 cases of thalassemia/ abnormal haemoglobin but only 18 cases (51.4%) were in anemia. HbE traits without α -thalassemia had the highest prevalence with 44.4% (Table 4). Only two cases of anemia

were severe, of which one case was in the first trimester and another in the second trimester, which were Hb H-CS disease and IDA, respectively.

Table 3 Prevalence of anemia, causes and severity in the pregnancy attended the first ANC in different period of gestation.

		N (%) Total = 190	Period of gestation		
			1 st trimester (n=87)	2 nd trimester (n=89)	3 th trimester (n=14)
Anemia cases		42 (22.1)	15 (17.2)	20 (22.5)	7 (50.0)
Causes of anemia	Anemia with thalassemia carrier/ abnormal hemoglobin	11 (5.8)	5 (5.7)	4 (4.5)	2 (14.3)
	IDA	10 (5.3)	3 (3.4)	5 (5.6)	2 (14.3)
	IDA with thalassemia carrier/ abnormal hemoglobin	6 (3.2)	1 (1.1)	3 (3.4)	2 (14.3)
	Anemia with other causes	15 (7.9)	6 (6.9)	8 (9.0)	1 (7.1)
Anemia severity		Anemia (cases)	1st trimester	2nd trimester	3th trimester
Categories	Mild	28	12	11	5
	Moderate	12	2	8	2
	Severe	2	1	1	-

Table 4 Types of thalassemia/abnormal hemoglobin and number of cases.

Types of thalassemia/abnormal hemoglobin	Case (n)	Cases with anemia (%)
HbH-CS disease	1	1 (5.6)
α -thalassemia-1 trait	3	3 (1.7)
β -thalassemia trait without α -thalassemia	5	3 (1.7)
HbE trait without α -thalassemia	23	8 (44.4)
HbE trait with α -thalassemia	1	1 (5.6)
Homozygous HbE	1	1 (5.6)
Suspected abnormal Hb	1	0 (0)
Total	35	18 (51.4)

Discussion

Anemia is a condition in which the concentration of hemoglobin is less than normal range. Cut-off value for adult males and females is 13.0 g/dL and 12.0 g/dL, respectively.¹⁷ Hemoglobin is an important component in RBC that plays a role in oxygen being carried throughout the body. The reduction in RBC production or increase in RBC destruction by any causes, either genetic defects or acquired diseases, leads to anemia. Thus, anemia can occur in all ages and worldwide. Pregnant women are the highest risk group of anemia due to the physiology changes during pregnancy.^{7,9,10} The cut-off value of Hb level for the second trimester is lower than the first and third trimesters, which are 10.5 g/dL and 11 g/dL for the second trimester and the first/third trimester, respectively.^{7,15} Following this criteria, the prevalence of anemia among pregnant women in the present study was 17.2%, 22.5 and 50.0% in pregnant

women who attended the ANC program at the first, second and third trimester of gestation, respectively. Causes of increasing in prevalence upon the period of gestation are the iron demand for RBC production and fetus development. In addition, plasma volume which significantly increasing in the second trimester and remain during pregnancy causes hemodilution and induces RBC production.^{7,9,10}

An oral iron supplement is one part of the nutrient supplements provided in all pregnant women who attend programs to reduce the risk of IDA. WHO recommends pregnant women should attend an ANC program early, within 8-12 weeks of gestation, for the comprehensive prevention of possible complications, including anemia.¹⁴ Pregnant women who admit to the ANC in the later period of gestation may have a greater chance of anemia developing due to insufficient iron intake. This result supports the ANC guideline that the prevalence of IDA is highest in the

third trimester ANC admitted group. In addition, this study detect only the SF which is recommended parameter for IDA diagnosis because of its stable, unaffected by recent iron intake, reflects iron stores accurately.^{8, 10} However, SF may elevated in inflammatory, so it might be the limitation of this report. Furthermore, Hct levels detected at 32-34 weeks of gestation in the IDA pregnant women who attended the ANC at the first and second trimester were increased (data not show). This improvement may result from the sufficient replacement of iron supplementation. The less number of pregnant women in the third trimester ANC admitted group in this study may result from the limit in period of data collection. In addition, it may indicate the awareness of maternal in early ANC attention.

Thalassemia is high in prevalence in Thailand.^{18, 19} Thalassemia gene carriers can cause anemia during pregnancy and low birth weight.²⁰ Twenty-six percentage of anemia cases in this report are accounted by thalassemia/abnormal hemoglobin carriers and 14.3% are thalassemia/abnormal hemoglobin carriers with IDA. The most frequent type is hemoglobin E trait, which is consistent with the other parts of Thailand.²¹⁻²³ The genetic counseling and screening program for thalassemia risk couples is an important step for safe pregnancy planning and reducing the incidence of thalassemia.^{11, 24} Thalassemic carrier pregnant women should be advised about complications prevention during pregnancy. In addition, anemia in pregnancy may be caused by folate and vitamin B12 deficiency, glucose-6-phosphate deficiency, Southeast Asian ovalocytosis (SAO) or anemia of chronic diseases.⁸ Nevertheless, this study determined only IDA and thalassemia.

Moreover, severity of anemia during pregnancy affects both maternal and fetal health. In mild cases, anemia may not effect but the insufficient amount of iron in the late period of gestation should be of concern. Weakness or fatigue may occur in moderate cases. For severe cases, the mother may have palpitations, tachycardia, and breathlessness and this may lead to preterm labor.^{8, 15} Although, most anemic pregnant cases in this presentation were mild anemia, the treatment of certain causes or prevention for severity improvement is necessary and should be done early.

Conclusion

This present study indicates that the prevalence of anemia in pregnant women is still high and increases in prevalence upon the period of gestation which may affect the maternal health and fetal development. The promotion of an ANC program for married couples and in adolescent women is necessary to improve the health quality during pregnancy and after-birth both for maternal and fetal health.

Acknowledgements

This study was financially supported by the Institute of Research and Innovation, Walailak University. We would like to thanks the staff of the Department of Medical Technology at Nayong Hospital for supporting us and the

pregnant women who participated in this study.

Conflict of interests:

The authors claimed no conflicts of interests.

References

- [1] WHO. The global prevalence of anaemia in 2011. Geneva: World Health Organization 2015.
- [2] Siriwong O. Anemia in pregnant women attending the Antenatal Care Clinic, Mae Sot Hospital. Thai J Obstet Gynaecol 2012; 20(4): 186-190.
- [3] Suchila Sritippayawan S, Wong P, Chattrapiban T. Iron deficiency anemia during pregnancy in the lower north of Thailand-prevalence and associated factors. Malaysian Journal of Public Health Medicine 2012; 12(2): 1-5.
- [4] Stevens GA, Finucane MM, De-Regil LM, Paciorek CJ, Flaxman SR, Branca F, et al. Global, regional, and national trends in haemoglobin concentration and prevalence of total and severe anaemia in children and pregnant and non-pregnant women for 1995-2011: a systematic analysis of population-representative data. Lancet Glob Health 2013; 1(1): e16-25.
- [5] Gupta PM, Hamner HC, Suchdev PS, Flores-Ayala R, Mei Z. Iron status of toddlers, non-pregnant females, and pregnant females in the United States. Am J Clin Nutr 2017; 106 (Suppl 6): S1640-6.
- [6] Krafft A, Murray-Kolb L, Milman N. Anemia and iron deficiency in pregnancy. J Pregnancy 2012; 2012: 241869. doi: 10.1155/2012/241869
- [7] Milman N. Iron and pregnancy--a delicate balance. Ann Hematol 2006; 85(9): 559-65.
- [8] Sharma JB, Shankar M. Anemia in pregnancy. JIMSA 2010; 23(4): 253-260.
- [9] Chandra S, Tripathi AK, Mishra S, Amzarul M, Vaish AK. Physiological changes in hematological parameters during pregnancy. Indian J Hematol Blood Transfus 2012; 28(3): 144-6.
- [10] Milman N. Iron in pregnancy: How do we secure an appropriate iron status in the mother and child? Ann Nutr Metab 2011; 59(1): 50-4.
- [11] Petrakos G, Andriopoulos P, Tsironi M. Pregnancy in women with thalassemia: challenges and solutions. Int J Womens Health 2016; 8: 441-51.
- [12] Leelahavarong P, Chaikledkaew U, Hongeng S, Kasemsup V, Lubell Y, Teerawattananon Y. A cost-utility and budget impact analysis of allogeneic hematopoietic stem cell transplantation for severe thalassemic patients in Thailand. BMC Health Res Res 2010; 10: 209. doi: 10.1186/1472-6963-10-209.
- [13] Gulino FA, Vitale SG, Fauzia M, Cianci S, Pafumi C, Palumbo MA. Beta-Thalassemia major and pregnancy. Bratisl Lek Listy 2013; 114(9): 523-5.

- [14] WHO. WHO recommendations on antenatal care for a positive pregnancy experience. World Health Organization 2016.
- [15] Cao C, O'Brien KO. Pregnancy and iron homeostasis: an update. *Nutr Rev* 2013 Jan; 71(1): 35-51.
- [16] Hemoglobin quantity and category analysis manual. The committee for hemoglobin quantity and category analysis manual. Nonthaburi: Clinical Research Center, Medical Science 2010 (in Thai).
- [17] WHO. Haemoglobin concentrations for the diagnosis of anaemia and assessment of severity. World Health Organization 2011.
- [18] Fucharoen S, Winichagoon P. Haemoglobinopathies in Southeast Asia. *Indian J Med Res* 2011; 134(4): 498-506.
- [19] Banyatsuppasin W, Jindadamrongwech S, Limrungsikul A, Butthep P. Prevalence of Thalassemia and glucose-6-phosphate dehydrogenase deficiency in newborns and adults at the Ramathibodi Hospital, Bangkok, Thailand. *Hemoglobin* 2017; 41(4-6): 260-6.
- [20] Sirichotiyakul S, Jatavan P, Traisrisilp K, Tongsong T. Pregnancy outcomes among women with homozygous hemoglobin E Disease: A Retrospective Cohort Study. *Matern Child Health J* 2016; 20(11): 2367-71.
- [21] Punyanuch J, Suchada R, Waraporn G, Yaowapa S, Sangkae C, Kittit T, et al. Diagnostic applications of newborn screening for α -thalassaemias, haemoglobins E and H disorders using isoelectric focusing on dry blood spots. *Ann Clin Biochem* 2013; 51(2): 237-47.
- [22] Fucharoen S, Winichagoon P. Clinical and hematologic aspects of hemoglobin E beta-thalassemia. *Curr Opin Hematol* 2000 Mar; 7(2): 106-12.
- [23] Nuntakarn L, Fucharoen S, Fucharoen G, Sanchaisuriya K, Jetsrisuparb A, Wiangnon S. Molecular, hematological and clinical aspects of thalassemia major and thalassemia intermedia associated with Hb E-beta-thalassemia in Northeast Thailand. *Blood Cells Mol Dis* 2009; 42(1): 32-5.
- [24] Engwa GA, Unaegbu M, Unachukwu MN, Njoku M-GC, Agbafor KN, Mbacham WF, et al. Low serum ferritin and G6PD deficiency as potential predictors of anaemia in pregnant women visiting Prime Care Hospital Enugu Nigeria. *BMC Res Notes* 2017; 10(1): 721. doi: 10.1186/s13104-017-3051-5

X-ray scatter correcting methods for digital radiographic imaging

Hudsaleark Neamin*

Department of Radiologic Technology, Faculty of Associated Medical Sciences, Chiang Mai University, Chiang Mai, Thailand

ARTICLE INFO

Article history:

Received 2 July 2018

Accepted as revised 24 July 2018

Available online 4 August 2018

Keywords:

X-ray scattering, x-ray scatter correcting, digital image processing

ABSTRACT

X-ray scattering correction method has been the primary means of enhancing radiographic images for quite some time. X-ray scattering is major deterioration factor that decreases image contrast and increases the image granularity in a radiographic image. However, this can be eliminated by using scatter reduction techniques like air gaps and anti-scatter grids, but the two techniques are cumbersome, and increases patient's radiation dosages. Moreover, it can also cause artifacts whenever anti-scatter grids are used. Recently, commercial software packages have been developed from various x-ray equipment manufacturers that have eliminated the need for anti-scatter grid usage. These recent advancements also allow lower patient dosages. Objective of this review is to summarize and review x-ray scattering and image processing algorithms used for enhancing the performance of the digital image in general radiography. Articles on digital image processing and commercial software for x-ray scatter correcting were thoroughly reviewed to complete this summary. These articles indicate that scatter correcting methods are based on principles of physics which involve of mathematical models of radiographic formation and x-ray scattering estimation methods. One simple model has the total energy absorbed at an image detector forming a primary x-ray plus a scattered x-ray whereby the point spread function of the scattered x-ray is used. Almost all estimations of x-ray scatter are computer simulations. The digital image post-processing algorithms are important factors in the x-ray scattering correction process. Their algorithms are related to mathematical models and the amount of scattering x-rays in an image, and are selected for use based on these considerations. These algorithms include subtraction, de-convolution, and anti-scatter grid simulation techniques. Therefore, x-ray scatter correcting methods for a digital radiographic imaging may be used in general radiography since their image quality is comparable to the images that have used anti-scatter grids, but are also beneficial since radiation dosage can be reduced using this process.

Introduction

X-ray scatter radiation is a major deterioration factor that decreases image contrast and increases granularity in the radiographic imaging. The scatter removing processes like air gaps and anti-scatter grids have been used in the past to improve the image quality, but both of them are

cumbersome and increases the patient's radiation doses. They can also cause radiographic image artifacts. Fortunately, commercial software has been developed from the various x-ray imaging system manufacturers that aim to enhance the correcting processes involved in x-ray scattering without the use of anti-scatter grids in general radiographic imaging examinations. Examples include such products as Virtual Grid, SkyFlow, Intelligent Grid, and Scatter Correction for CXDI Series, SimGrid, and SBSC. They come equipped with digital imaging systems like optional software, and have been approved by the FDA. The image qualities are comparable to the images using anti-scatter grid, but radiation dosages

* Corresponding author.

Author's Address: The Department of Radiologic Technology, Faculty of Associated Medical Sciences, Chiang Mai University, Chiang Mai, Thailand

** E-mail address: hudsaleark.neamin@cmu.ac.th

doi: 10.14456/jams.2018.18

E-ISSN: 2539-6056

can be reduced using these products. These techniques are particularly good for pediatric radiography, bedside radiography of patient who cannot be moved, and dual-energy mammographic imaging. Without a grid, the technologists can work more efficiently. These techniques eliminate unwanted image artifacts due to grid misalignments that may affect images enough to require retakes. Consequently, these products make for better patient care.^{1-5,15}

When a radiographic image is forming, an x-ray passes through the patient or object being examined, and there are three possible directions that each x-ray photon can take. First, it can penetrate the patient without interacting by what is usually called the primary x-ray (the remnant beam). Second, it can interact with the patient and be completely absorbed by depositing its energy. This is usually called the patient absorption dose. Third, it can interact and be scattered from its original direction with or without depositing a part of its energy by what is usually called a scattered x-ray.⁶ In diagnostic radiology, x-ray photons have energy ranges between 17 to 150 keV. This range would also apply to mammography. Three dominant X-ray photon interactions include the photoelectric effect, coherent scatter, and incoherent scatter. To understand radiographic image formation and how to determine the appropriate radiation dose given to patient for enhancing radiographic image quality, we need to understand the interactions of x-ray photons with matter as this relates to photon carry energy, tissue type, and composition of subject to be investigated, especially in the energy ranges used in diagnostic radiology.

Radiographic image formation is one of the radiation transport problems which depends on photon interaction. Generally, photon interaction can be predicted by their probabilities. They depend on energy of photon and the material component, which are themselves random situations. The photon interaction can't easily be solved directly by calculation, but can be estimated by computer application using The Monte Carlo simulation method. Monte Carlo simulation determines the number of x-rays that have penetrated the patient and those that have been absorbed by image detector, as well as the energy deposited in the subject lead to patient dose. The details of scatter x-ray can be demonstrated clearly by Monte Carlo simulations that take into account conditions, various parameters and geometry of user's interesting in their radiation transport problems.

Estimations of the primary x-ray and the amount of scatter x-ray photons are very important parameters for calculating the scatter degradation results, establishing x-ray scatter correction methods, and evaluating which correction method that is the most appropriate. For example, the experimental methods for the Blocker-based techniques and the beam stop techniques use high radiation attenuation materials and a bulk of tissue that is equivalent material for simulating x-ray photons that pass through subjects. The x-ray photons occurring as primary and scatter x-rays are measured by image detector.⁸ The Scatter to Primary Ratio (SPR) and Scatter fraction (SF) are the relationships of primary, scatter, and the total x-ray photons. These ratios can

be calculated from the data found by this experimentation. SPR and SF quantitatively show the degree of scatter generating related to the exposure technique (kV, mAs, filtration, and field size) and the subject thickness. For assessment the quality of clinical images by quantify the scatter degradation in an imaging system. The differential signal to noise ratio (SNR) or contrast to noise ratio (CNR) are used. The other quantitative assessments use physical indicators like contrast improvement, granularity improvement and sharpness, and IQFinv. All of these assessments can be applied to clinical images of various kind of radiographic imaging systems.¹

Primary x-ray makes for useful information to visually separate the different tissue types in an image, but the scatter makes for an unusable exposure because it spreads across the image receptor and adds to the amount of exposure to every tissue in the area within the image. This effect reduces subject contrast and increases the granularity over the entry imaging area.⁷ The combination of primary and scatter x-ray forming in a radiography image described here is a general model. Many authors explain this model by equations, functions, or mathematical models currently used in engineering applications. These models are very beneficial as they introduce important variables and their relationships which are of particular concerns for use in x-ray scatter estimation and correction methods.

For a long time, the image processing algorithm for x-ray scattering correction remained the main method for enhancing a radiographic image. This process calculates the primary x-ray and the scattering radiation from an image captured by an imaging detector. Separating and correcting the scattering part with image processing algorithms leaves only the primary part forming the image. The physics of radiographic image creation and the development of digital image processing methods plays an important role in the x-ray scattering correction process without the use of air gaps or grids. Such a principle demonstrates the potential for use in general radiographic imaging as more commercial software is being developed. These advances reduce radiation dose, improve workflow and efficiency, and thereby make for better patient care. The objective of this review is to briefly describe the scattering x-ray calculation methods, image processing techniques, and the algorithms used for enhancing the quality of the digital image in general radiography.

1. X-ray photon interaction

Within the x-ray diagnostic radiographic energy range of 17-150 keV, three x-ray photon interactions with matter are observed: The photoelectric effect, coherent, and incoherent scattering. These interactions have an influence on the amount of the primary and scatter x-rays which are produced in an x-ray image.

1.1 Photoelectric effect

Photoelectric effect is the dominant process occurring at lower energy portions of the diagnostic x-ray range. It arises when an x-ray photon collides with an electron bound within an atom shell of medium energy level and transfers all its kinetic energy to the electron. If the photon

energy is smaller than the binding energy of the electron in that shell, the x-ray photon can then interact with an electron in the outer shells where binding energy is lower. In the case of x-ray photons, kinetic energy is greater than the binding energy of that shell. Consequently, the x-ray photon can reject the electron making for ionization. The free electron is called a photoelectron and its energy will be the difference between the x-ray photon energy and the binding energy of the atom shell. The free electron can travel in the medium and transfer energy along the path length before becoming absorbed. This process contributes to be the patient's absorption of the radiation dosage. The vacancy left in the atom is filled by electrons in the outer shells producing the characteristic x-ray. This type of x-ray is called a fluorescent x-ray and it can interact with electrons in the outer shells producing new photoelectrons called Auger electrons. Soft tissue of human body consists of the low atomic number materials, so the characteristic x-ray energy suitable for humans is also low, as well. It cannot travel as far and will be re-absorbed into the body.

Probability of a photoelectric event occurrence is called the cross section of photoelectric interaction. To predict the probability that an interaction event will occur, the relationship of the energy of photon and the atomic number of an element can be applied to calculate the probability of the event. Photoelectric effect event is proportional to the atomic number of an element, but is inversely proportional to the energy of the x-ray photon.⁶

1.2 Coherent scatter (Rayleigh scattering, Elastic scattering)

When x-ray photons have less energy than the binding energy of an electron in an atom shell, it collides with that electron. Two interactions may occur in this scattering interaction. First, the Thompson effect can occur whereby the x-ray photon energy is absorbed by an orbit electron. Excitation then takes place to where the photon reemits with original energy. Second, Rayleigh scattering can occur in ways similar to the Thompson effect, but instead photon energy is absorbed by the electron cloud around the atom. The direction of the reemission is at a random angle compared to the original direction of the incoming x-ray photon. To predict this deflection angle,⁷ J.J. Thompson equation is used. It describes the differential cross section of x-ray photons scattered by a free electron, but it does not explain the coherent scattering angle because the tissue being investigated in medical imaging have electrons which are bound to an atom. Not being a free electron, it has been modified by multiplying with an atomic form factor term. This term includes the energy of the incident photon and the atomic number of the material in question. This modified equation can explain scattering angular distributions for different energies of x-ray photons and the element being investigated.⁶

1.3 Incoherent scatter (Compton effect, Inelastic scattering)

In incoherent scattering, the x-ray photon has a higher energy than the binding energy of electron within an atomic shell. When it strikes an electron, it imparts some of its energy to it. The electron is rejected from its shell

while carrying some energy at a departing angle while the x-ray photon is scattered in a direction at an angle to the original direction. Typically, the electrons found at the outer shells of an atom are more likely to be affected by incoherent scattering. The energy of the x-ray photon occurring at an angle after interaction can be approximated using the Principle of Conservation of Energy and Momentum. The energy of electron can be calculated by subtracting the energy of scattering photon from its incident photon energy. The departing angle of electron can be calculated by using energy and the scattering angle of the x-ray photon. The cross section of the Compton Effect event can be calculated using the Klein-Nishina equation.⁶

1.4 Photon interaction and image formation

The distribution of primary x-ray photons over the entry area of the image detector contains useful information to visually separate the different tissue types in a radiographic image through what is called contrast. It is based on the differing attenuation of these tissues. All human tissues are composed of different kinds and proportions of elements, so x-ray attenuation in any type of tissue can be different even in healthy or bad conditions. X-ray attenuation occurs when removal of x-ray photons takes place from an incident beam by absorption or through scattering interaction. This occurs when photons travel along the tissue before being detected by an image detector.

Linear attenuation coefficient (μ), depends on x-ray energy. It is used to describe the amount of attenuated and un-attenuated photons. The linear attenuation coefficient is determined by multiplying the number of the matter's atoms per unit volume and the total cross section of all photon interaction. For x-ray energy ranges used in diagnostic imaging, the total cross section is the three photon interaction cross section. Therefore, the primary x-ray is accounted for using the un-attenuated x-ray and the un-scattered x-rays which have reached the image detector. The intensity of primary x-ray can be calculated by the Beer-Lambert Law using the energy beam, the linear attenuation coefficient of tissue component, their geometry and the distance required for a photon to pass through a medium of matter.⁷ The choice of energy will be a compromise between the patient dosage and high contrast image levels. If the energy is very low, then very few photons will reach the image receptor and the radiation dose to the tissue will be very high. If the energy is too high, then there will be very little difference in transmission through different types of tissue and the contrast in the image will be poor.⁹ When x-ray photons are absorbed by image detector, the photo electron and K-shell characteristic radiation are produced and are also absorbed into the image detector due to the photoelectric effect. Locally, electrons will absorb, but characteristic radiations do not. The mean free path of characteristic radiation which arise from an element by the image detector like Ag, Cs, or Gd are long enough to spread widely. This can lead to loss of efficiency and to image blurring.

The scatter x-ray acts as a background. The factors that increase the amount of scatter radiation are the higher level of photon energy, large field sizes of x-ray beam, and a large body part and/or thicknesses of soft tissue.

The large field size of an x-ray beam and large body parts produce significant amount of scatter radiation, but the higher kV does not produce significant scatter radiation in small body parts. Even in thicknesses found in parts of the body such as the abdomen, the visible fogging of images caused by scatter are comparable when radiographed with 80 kVp and 92 kVp. Scattering interactions do not result in absorption of the photon. The coefficient for the energy-absorptive component of the scatter is due to the transfer of energy to recoil electrons. In general radiography, the rejecting or reducing of x-ray scatter have been implemented using techniques such as grid or air gap, but they are difficult to transport and the patient's radiation dosage may increase up to double when using a grid.⁷

1.5 Monte Carlo simulation

The Monte Carlo method is an effective technique used for simulation of radiation transport in matter. This method employs random sampling from probability distribution of an event for construction of the solution to a physical or mathematical problem. The Monte Carlo simulation for x-ray photons used in the diagnostic energy ranges involves three interaction processes that may occur when a photon passes through any medium. When an incident x-ray photon strikes the surface of a medium, the free path length is determined from an exponential distribution and the interaction site is calculated using the free path length and the direction of the incident photon. Afterward, the type of interaction that will occur is determined from the interaction cross section data. If it is photoelectric effect, the total energy of the x-ray photon is absorbed. If a repeated simulation for the next photon predicts an incoherent scattering, the scattering angle and energy of the scattered photon are determined using the Klein-Nishina equation for the Compton Effect. If it is likely that coherent scattering will occur, the scattering angle is determined using the Thompson equation.⁸

The Monte Carlo simulation uses a large number of x-ray photons in the calculation in order to make a good estimation. It uses the same sophisticated steps in calculation as that of geometric modeling for experimentation and error reduction. It can even speed up the calculation itself. The results of these simulations are energy absorption, scattering, and energy transformation. They are used to describe the primary and scatter behavior in forming the radiographic image formation. Several particle physics Monte Carlo simulation packages currently exist that are widely used in medical physics studies. The most common are EGSx/EGSnr, MCNP/MCNPX, Penelope, GEANT4, and FLUKA. Many researchers use the Monte Carlo method while doing studies on scatter x-ray correction methods. There are x-ray products being sold through vendors that use the Monte Carlo method for calculating the amount of scatter x-ray in each take of image and use it for scatter correction processes designed for reader console software.^{1-5,14}

2. Radiographic image formation, primary, and scatter x-ray models

2.1 The simple model

The radiographic image formation can be described by a simple mathematical model. X-ray energies absorbed at the image detector, $I(x,y)$, are primary and secondary photons as shown by equation number 1. An x-ray source that emits the photons of energies in the diagnostic range allows the ray of the x-ray beam to safely pass through the subject. It falls perpendicular to the image detector and is locally absorbed at the x, y position of the plane of the image detector. The primary photon energies absorbed by the image detector form the image, but the secondary photons create a background signal, as shown by Figure 1.⁹

$$I(x,y) = \text{primary} + \text{secondary} \quad (1)$$

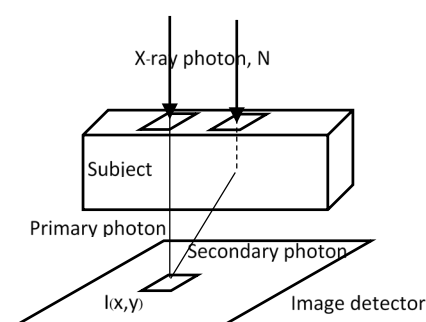


Figure 1 Simple model of the radiographic image formation shows the combination of primary and a secondary x-ray photons striking an image detector.

The x-ray energies absorbed at the image detector can be defined like mathematical integration as shown by equation number 2. The first term is the line integral along the path of primary photons arriving and absorbing at point x, y of image detector plane. The second term is the scatter distribution function of energy absorption efficiency (ϵ), energy range (E_s), and solid angle (Ω). The scatter function S has a complicated dependence on the position and the distribution of tissue within the patient. For many applications, it is sufficient to treat it as a slowly varying function, and involves replacing the very general integral with the value at the center of the image.⁹

$$I(x,y) = N\epsilon(E,0) \text{Exp}\left(-\int \mu(x,y,z)dz\right) + \int \epsilon(E_s,\theta)E_s S(x,y,E_s,\Omega) d\Omega dE_s \quad (2)$$

The usefulness of this simple model is clearly demonstrated in all parameters that are concerned with studying scatter x-rays. This is true not only in a real experiment setup, but also in computer simulations because this equation combines the primary and secondary x-ray photon as the total energy absorbed by image detector. Ryohei ITO *et al.* used this assumption to do the scatter subtracted from the total radiation arriving at the image detector using an algorithm found in some scatter correcting methods.³ Elena Marimón assumes that the image formed by a digital mammography detector is the linear combination of the primary and scatter x-ray photons and uses the convolution based method to estimate the scatter photons.¹¹

2.2 Scatter to Primary Ratio (SPR, STPR) and Scatter fraction (SF)

SPR and SF are the ratio of the intensity of scatter radiation to that of primary radiation. It is useful in determining the degree to which image contrast can be degraded. Evaluation of the characteristics of scattered radiation in diagnostic radiology as a rule will be determined with suitable phantoms, but not with patients.⁷ In many studies, they conduct the experiment with water or PMMA of human size phantoms. Sometimes these studies use a Monte Carlo simulation. Not only is it possible to evaluate the characteristics of scatter, but it is also possible to take measures to check the scatter correction technique. Scatter to Primary Ratio is the magnitude of the scattered to primary x-ray at image detector after having penetrated subject. Scatter fraction is the measured quantity of scatter found in the total image record as shown by the following equations, where S and P are scatter and primary x-ray, respectively.¹¹

$$SPR=S/P \quad (3)$$

$$SF=S/(S+P) \quad (4)$$

SPR and SF can be estimated by the conventional technique set up for scatter in diagnostic radiography. The Blocker based techniques or the beam stop technique are shown in Figure 2.¹¹ These techniques consist of imaging subjects made of high radiation attenuation material such as lead (Pb). Lead stops absorption of almost all of the primary x-rays which are incident on the surface of a phantom. Underneath where the primary x-ray beam stops, a block of material is positioned which has the radiation characteristics equivalent to that of human tissue. It is used to demonstrate the scatter x-ray produced when the beam of x-ray passes through the material and is absorbed by image detector. The beam of the x-ray that cannot pass through Pb block only results in scatter x-rays. The primary and scatter x-ray are found elsewhere in the radiation field. As a result of S and S+P outcomes, they are then being combined to calculate the primary (P), SPR, and SF for this particular experimental setup. By varying the x-ray beam energy and scatter material thicknesses, the primary, SPR and SF of each experiment and the setup geometry can be observed.^{6,7}

Both the SPR and SF increase as the subject thickness increases; thus, for thick body parts, such as the abdomen, scatter radiation is a serious problem. In chest radiography, the equivalent tissue thickness of the lung is approximately one half that of abdomen. However, tissue thicknesses in the chest may vary from 10 to 30 cm in the mediastinum. Cross scatter from one region of chest to another results in SPR for some areas of the chest where thicknesses may exceed those found in abdominal radiography.

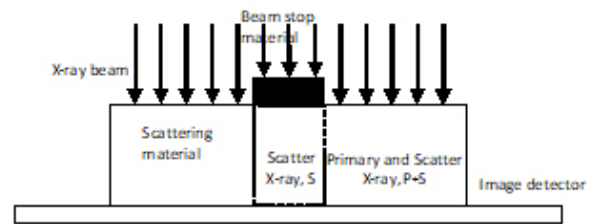


Figure 2 Diagram of the blocker based techniques or the beam stop technique for measuring SPR and SF.

2.3 Scatter point spread function (SPSF)

Point spread function (PDF) is the 2D impulse response function produced from a point source passing through any system. For radiographic imaging, the point spread function represents the spatial distribution of radiation when a narrow beam of x-ray passes through matter as shown in Figure 3(a). PDF is described in polar coordinates $PSF(r,\theta)$. PDF demonstrates how x-ray energies are recorded over imaging area by absorption of the energies of primary and scatter x-rays using image detectors. Therefore, the PDF of image detector $PDF_{detector}(r,\theta)$ can be described by the contribution of primary x-ray $PDF_p(r,\theta)$ and scatter x-ray PDFs (r,θ) .^{10,11} The later can be called a scatter point spread function (SPSF). Generally, the PDFs (r,θ) is normalized to the total energy deposited by the primary x-ray and integration of the normalized PDF would correspond to the SPR value (Scatter to primary ratio) as seen in equations 5 and 6.

$$PDF'_s(r,\theta) = \frac{PDF_s(r,\theta)}{\int_{\theta=0}^{2\pi} \int_{r=0}^{\infty} PSF_p(r,\theta) d\theta dr} \quad (5)$$

$$SPR = \int_{\theta=0}^{2\pi} \int_{r=0}^{\infty} PDF'_s(r,\theta) d\theta dr \quad (6)$$

To estimate the pencil beam SPSF by the conventional technique, an assortment of small to large diameter size of x-ray beam stop subjects are used to measure the SPR for each diameter size of beam stop subject. The relationship between diameter size and SPRs are obtained by using curve fitting method. Therefore, SPR at a zero diameter represents a size of point source and can be extrapolated from this relationship with a unit of area-1. The ratio of scattered x-ray to primary x-ray can be found after penetrating the subject with the x-ray irradiation field that is set to the same size as the x-ray detector. As the STPR increases, the image deteriorates as a subject's habitus become thicker. Therefore, the amount of scattered x-ray does not contribute to the depiction as anatomical structures increase.¹

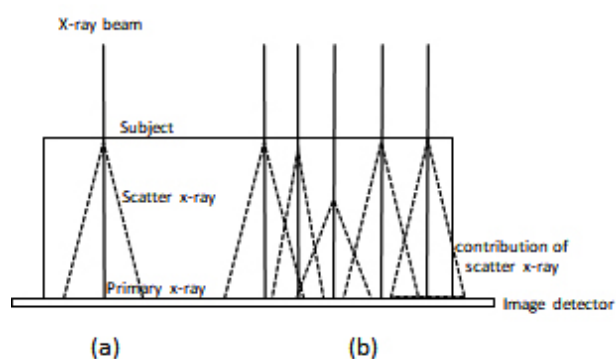


Figure 3 Scatter point spread function (a) single x-ray show SPSF and (b) cumulative SPSS from scatter x-ray distribution over on image.

PDF can be used to estimate scatter forming at image detector as shown by Detlef Mentrup *et al.*² They state that the amount of scatter x-ray depends upon thickness and composition of an object. The total scatter present in the image can be thought of as a superposition of scatter contribution generated by a thin pencil-x-ray beam passing through an object. These are called scatter kernels as shown in Figure 3(b). The superposition of all scatter kernels in the imaging area are used to estimate scatters over an entire image.

2.4 Convolution based scatter estimation

Convolution is a mathematical operation on two functions to produce a third function. In convolution based scatter estimation, the primary x-ray as one function are modified or filtered by the other function typically called a convolution kernel to estimate a result of scatter x-ray distribution at image creation location by the primary x-ray as shown by equation 7.

$$I_s = I_p * h_s \quad (7)$$

I_s , I_p , and h_s are scatter, primary x-ray, and the convolution function, respectively. There are some characteristics of convolution functions that have been revealed in many studies. Detlef Mentrup and Kotre CJ show that scattered radiation is a slowly varying background to image phenomenon. This behavior of scatter x-ray distribution on imaging areas appears similar to that of low spatial frequency. Convolution kernels can be used to explain this characteristic.^{2,14} Love, L. A. and Kruger use a convolution-filtering method to estimate the scatter distribution in images by investigating many convolution kernels and applying them to images of anthropomorphic phantoms. They found that two-dimensional exponential kernels with a full width at half a maximum of 50-150 pixels best reproduced the scatter fields within these images.¹² Elena Marimón approximated the scatter by a two-dimensional low-pass convolution filter of primary image.¹¹ As mentioned before, the radiographic images created from image detectors originate from primary and scatter x-rays. The scatter can be represented as a convolution of primary image with the scattering kernel (h_s).

2.5 Other mathematical models

K. Kim *et al.* defined scatter x-rays as an image degradation function like those used in other fields such as engineering.¹⁷ The desired function could have characteristics like that of scatter deterioration. In this study, dark-channel prior is a more suitable, so this method can be used to restore deterioration to the original image. In other study, some types of noise sources have potential for studying scatter x-rays. Pierre Gravel *et al.* study the statistical properties of noise found in medical images. The types of uncorrelated noises are Gaussian, Poisson, and Rician noise are selected to determine the relationship between an image intensity and noise variation, and to evaluate the corresponding parameters for each type of noise.¹⁹

3. Brief review of scatter x-ray photon estimation techniques

Scatter x-ray has a complicated dependence on position and the distribution of tissue within the patient. For many applications, it is sufficient to treat it as a slowly varying function and to replace the very general integral with the value at the center of the image.⁹ Similarly, some researchers use the low spatial frequency convolution function like a low pass convolution or exponential function to represent the scattered x-ray in an image.^{2,14} The accuracy of the scatter x-ray estimation is very important in order to correct its effect on any image. In this section, there are examples provided of estimation techniques that use scatter correcting algorithms proposed by particular researchers. The estimation techniques can be divided into two groups: There are those techniques which are found in commercial software, and there are the various techniques used by research groups.

Takahiro KAWAMURA *et al.* estimated the scatter x-rays from the thickness of subject which is under radiographically examination. They use the pixel values from image detector area with a subject and without a subject to estimate the thickness. The subject thicknesses and x-ray photon energy are used to estimate amount of scatter x-ray from pre-calculated values of scatter to primary ratio. Each pixel of radiographic image will be used to estimate for the scatter x-ray pattern over entire imaging area.¹ Ryohei ITO *et al.* developed the algorithm that estimates the thickness of subject for each image pixel from a histogram of the original image and made a body thickness image. They use the body thickness image to estimate scatter x-rays from a table or data base of scatter x-ray ratio to object thicknesses. Their algorithm concerns not only a pixel of interest, but also provides insight regarding various surrounding structures.³ Detlef Mentrup *et al.* used the model of scatter point spread function to estimate the scatter for the image under radiographically examination. The scatter kernels used by this model are pre-calculated using a data base in a Monte Carlo simulation which can be adapted to patients with different constitutions. The selection is based on the local pixel value and its spatial gradient. The super position of all scatter kernels over entry image area is the total scatter image.²

IBEX Innovations Ltd. has developed a scatter correcting method called gridless scatter reassignment. This algorithm

measures material type and thickness of subjects in radiographically examinations. The Monte Carlo simulation aids in estimating the scatter x-ray maps from material type and thickness of subject and can be refined until accurate predictions of each subject are obtained.¹² Andreas Fieselmann *et al.* models the scatter radiation in mammography that can be divided into a low-frequency and a high-frequency component. A low-frequency component is a smoothly varying value which added to pixel value of an image. The high-frequency is noise. Fieselmann estimated only a low-frequency component having a scatter point spread function that is simulated by the Monte Carlo method based on subject properties, the geometry, and acquisition parameters.¹⁴

For commercial software package, Takahiro KAWAMURA and Ryohei ITO estimate the scatter value by subject thickness and pre-calculate scatter ratio data base for each pixel over entry image area. Other authors use thickness coupled with aid from Monte Carlo simulations. Among these, the point spread function or convolution kernel scatter models are used. In all estimation techniques, the scatter x-ray patterns are adjusted to specific parameters for each situation of radiographic examination. A particularly interesting one was based on a subject thickness estimation technique. These researchers used the pixel value in image to estimate the thickness of all anatomical parts in order to estimate scatter x-rays on an image. For some research groups, the Monte Carlo simulation is frequently used in conjunction with convolution scatter x-ray models. There is work being done over several modalities in radiological examinations, not only for general radiography, but also in computed tomography and digital breast tomosynthesis. All these applications have benefited from scatter correcting techniques. There are other the examples provided in these articles, as well

Atila Ersahim *et al.* used a two dimensional convolution of the scatter-glare point spread function to estimate scatter x-rays of image. There are functions involving thickness of subject, beam energy, field size, and air gap of imaging geometry. Theses estimations used Lucite as a tissue equivalent material and measured the primary and scatter x-rays with a beam stop technique.¹³ Elena Marimón *et al.* approximates scatter x-ray by a two dimensional low pass convolution filter of the primary image. This approximation was first introduced by a Love and Krunger study. The scatter

point spread function was obtained from the Monte Carlo simulation using a GEANT4 toolkit. The experimental geometry was defined in order to simulate the geometry of a mammography system where the phantom image was acquired.⁸ Danyk A. Y. *et al.* determined the scattering kernel functions using realistic Monte Carlo simulations and robust scattering estimation algorithms. The set of resulting data is subjected to statistically processes in order to identify a set of the most relevant scattering kernels by clustering analysis. The kernel is used to train the classifier for identifying which area of an image that scatter kernels should be applied.¹⁵ O Diaz *et al.* developed a fast kernel-based methodology for scatter field estimation which is more rapid than the Monte Carlo simulation. This method is thickness-dependent scatter kernel and accounts the full geometry in real digital breast tomography. The computational time is more than five time faster than Monte Carlo simulation and the estimation of error is equal to or less than 10%.¹⁶ K. Kim *et al.* proposed a new model-based radiography restoration method based on simple scatter-degradation. The two models included in their work are the Scatter-degradation and Radiography restoration models. The image restoration function was investigated to determine its relevancy as a well suited function. They found that the dark-channel prior is more suitable for any proposed restoration.¹⁷

4. Image processing algorithms

First, a simple model has been proposed in which the primary and scatter x-ray is combined to form the radiographic image. The scatter x-ray is directly removed from the original image. Some authors add image processing steps like noise reduction to remove any deteriorating effects of which they are concerned. Ryohei ITO uses this model for any scatter correcting processes. After scatter estimation, he removes the signal amount corresponding to scattered x-rays in the image. Next, the noise caused by the scattered X-ray component and the graininess is reduced in order to improve the noise reduction processing as indicated in step 4 of diagram in Figure 4.¹³ Andreas Fieselmann subtracted the low-frequency component of scatter from the original image. No more details about image processing steps taken after correction of scatter x-rays were indicated in this work.¹⁴

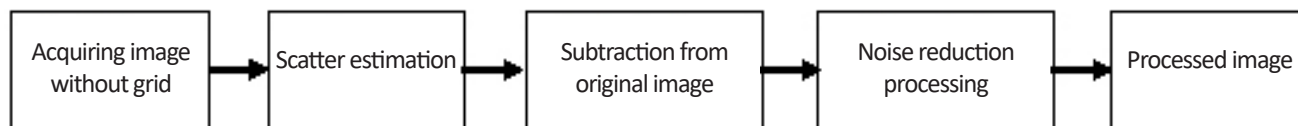


Figure 4 Simple model; scatter is subtracted from original image.

The following is a summary of Grid effect simulation. When a real anti-scatter grid is used, the x-ray photons from patient pass through a grid and are reduced in accordance with the primary and scatter transmission factors of the grid. The scatter x-ray is reduced more than the primary due to grid structure, making the image contrast better. The reduction factors of primary and scatter x-rays are grid ratio, grid frequency, and lead content. This image enhancement method uses the same image processing algorithm that is designed to simulate anti-scatter grid effect. The scatter x-ray estimation technique can calculate the x-ray scatter parts separately from the total signal detected by the image detector and allows the primary x-ray to be calculated immediately. Grid effect simulation

algorithms does the contrast improvement work by calculating the reduction of the primary and scatter x-ray using the same factors found on a real grid. After taking the examination, the resulting image is obtained and is similar to the one that was acquired with an anti-scatter grid.¹

Granularity or noise is the one deterioration factor that arises from scatter x-rays. This component is called "structure less" noise. When a scatter x-ray is reduced, image contrast is improved, but noise effect still remains in an image. A filtering technique can improve the granularity in an image [1]. Grid effect and granularity improvement processes are shown in Figure 5.

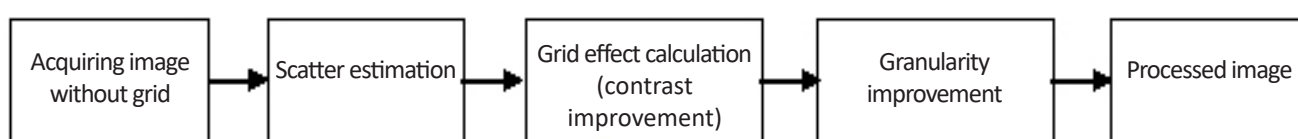


Figure 5 Grid effect simulation and granularity improvement process.

Detlef Mentrup adjusts the scatter x-ray image with a parameter in order to remove parts of them from the original. The resulting image consists of a primary that contains small bits of scatter. The single parameter used to control the algorithm is the grid selectivity which is a quality that is defined in the IEC standard 60627. Scatter

x-ray is removed by subtraction from the original image. Afterward, the image needs to be adjusted to obtain a balance between over and underexposed areas in order to bring out the details in very dark and very bright regions necessary for better image quality² as shown in Figure 6.

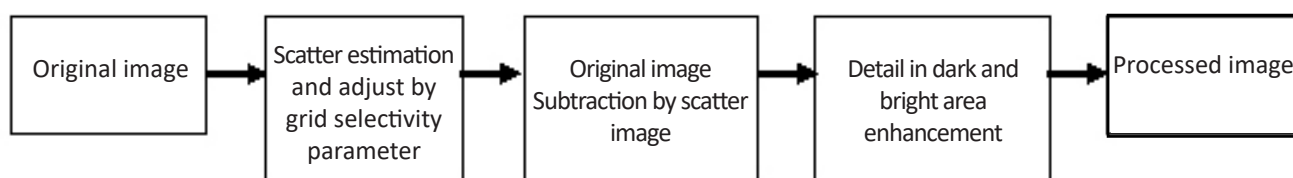


Figure 6 Grid simulation using selectivity parameter for contrast enhancement.

Another technique called the deconvolution model is based on the principle that scatter x-rays are a mathematical convolutions resulting from the primary or the measured image with scatter kernels. Deconvolution or Inverse Fourier Transform can be used to calculate the primary from an original image and the estimated scatter x-rays. J L Ducote advocated using the image deconvolution model to decouple the convolution of scatter from the primary image. The convolution kernel in this work is specified to be used with both primary and scatter. In order to separate the primary x-ray, J L Ducote proposed that the measured image is equal to the convolution of the primary with this specific kernel. The advantage of Inverse Fourier Transform is that it can calculate the primary x-ray which is present in a measured image.²⁰ Danyk, A.Y. developed a scatter correction technique that improves image contrast to near the possible maximum. This work is based on the idea that scatter can be present as the linear combination of the primary and point spread

function or scatter kernel. This work was a simulation study done on a few homogeneous subjects. The measured image is the combination of the primary and the convolution resulting from the primary and scatter kernel. Therefore, the Inverse Fourier Transform can approximate the primary x-ray which is present in measured images in ways similar to the work of J L Ducote. In order to maximize image contrast, clustering analysis and classifiers for identification calculation technique are used.¹⁶

5. Image quality and patient dose assessment

When comparing the scatter correcting image with non-grid and grid image by visual perception method it is found that the scatter correcting image is clearly an improvement over the on-grid images. This is especially true in chest and abdomen radiography.³ Contrast to noise ratio (CNR) is another method currently being used. This method used a Burger and CDRAD phantom and an IQF

(Image quality figure) value to evaluate contrast improvement. Ryohei ITO shows that CNR and IQF_{inv} of image using scatter correcting method is equal to an image using 6:1 grid.³

Signal to noise ratio (SNR) used by IBEX Innovations Ltd to compare SNR of scatter correcting and grid image by imaging a phantom that was made up from a PMMA. The results showed that the mean SNR of scatter correcting images had an improvement by a factor of 1.16.¹²

Contrast improvement factor (CIF) proposed by Detlef Mentrup used CIF to compare the image quality of a water phantom and a Lungman phantom. It was found that there was strong agreement that existed between the ICF obtained with the scatter correcting method and the ICF obtained with the grid. For clinical applications, scatter correcting techniques demonstrated a significantly higher image quality for grid-less bedside chest radiography when patient dosages had decrease by 0.6.²

V. Tóth showed that the scatter correcting software significantly improved image quality of grid-less bedside chest x-ray, but did not reach the level of quality found in a chest x-ray equipped with an anti-scatter grid. User benefits from the significant reduction in patient dose.²¹

Conclusion

The image processing algorithms used for x-ray scattering correction still are the main concepts used for enhancing a radiographic image. Currently, commercial software packages have been developed by various x-ray equipment manufacturers that have largely replaced anti-scatter grid usage. The enhancement algorithms based on scattering estimation and scatter correcting method. Monte Carlo scattering x-ray pre-calculated database and patient thickness estimation technique used to adjust the algorithm for each specific situation of examination. Users will have the benefits of improved image quality, it will allow reduced dosages for patients, and there is a general improvement in efficiency resulting from using these algorithms necessary for improved workflow that will add to the overall improvement in patient care.

Acknowledgements

This article was supported by Department of Radiologic Technology Faculty of Associated medical sciences Chiang Mai University. Finally, I would like to thank you Assoc. Prof. Dr. Suchart Kothan, for recommendations for writing this article.

References

- [1] Takahiro KAWAMURA, Satoshi NAITO, Kayo OKANO, Masahiko YAMADA. Improvement in Image Quality and Workflow of X-ray Examinations using a New Image Processing Method, "Virtual Grid Technology". Fujifilm Research and Development 2015. Available from: http://www.fujifilm.com/about/research/report/060/pdf/index/ff_rd060_004_en.pdf
- [2] Detlef Mentrup, Ulrich Neitzel, Sascha Jockel, Hanns-Ingo Maack, Bernd Menser. Grid-like contrast enhancement for bedside chest radiographs: acquired without anti-scatter grid. European Society of Radiology 2014 March. :1-15
- [3] Ryohei ITO, Tatsuya TAKAGI, Keita YOSHIDA, Akira ISHISAKA. Development of the Intelligent Grid Scattered X-ray Correction Processing System for Digital Radiography.KONICA MINOLTA TECHNOLOGY REPORT 2016 .vol.13: 52-6
- [4] Scatter Correction Excellent image contrast without a grid. Report Scatter Correction reduces radiation dose and offers better ergonomics. Canon Medical Group 2017. Available from: <http://www.mediel.se/assets/download.cfm?file=5878A7AB84FB-43402106C575658472FA>
- [5] Advanced Applications for GC85A. Samsung Healthcare Global Newsletter.[cited 2017 Dec. 17]. Available from: <http://www.samsung.com/global/business/healthcare/Newsletter/201604/gc85a.html>
- [6] Horst Aichinger, Joachim Dierker, Sigrid Joite-Barfuß, Manfred Säbel. Radiation Exposure and Image Quality in X-ray Diagnostic Radiology: Physical Principles and Clinical Applications (2nd). Springer Heidelberg Dordrecht London. New York; 2012
- [7] Quinn B. Carroll. Radiography in the Digital Age Physics Exposure Radiation Biology. Charles C Thomas Publisher. LTD. Springfield Illinois U.S.A.; 2011
- [8] Elena Marimón, Hammadi Nait-Charif, Asmar Khan, Philip A. Marsden, Oliver Diaz. Scatter reduction for grid-less mammography using the convolution based image post-processing technique. Available from: Society of Photo-Optical Instrumentation Engineers <http://spie.org/Publications/Proceedings/Paper/10.1117/12.2255558>
- [9] John G Webster, E Russell Ritenour, Slavik Tabakov, Kwan-Hoong Ng. Webb's Physics of Medical Imaging (Second Edition). CRC Press Taylor&Francis Group Boca Raton London New York; 2012
- [10] D.R. Dance, S.Christofides, A.D.A. Maidment, I.D. McLean, K.H. Ng. Diagnostic Radiology Physics A Handbook for Teachers and Students. IAEA; 2014
- [11] Love, L. A. and Kruger, R. A. Scatter estimation for a digital radiographic system using convolution filtering. Medical Physics 1987; 14(2); 178-85.
- [12] GRIDLESS IMAGING FROM ANY DIGITAL RADIOGRAPHY SYSTEM. IBEX Innovations Ltd. 2017. Available from: <http://ibexinnovations.co.uk/uploads/004-MM-006%20Rev%201.02%20White%20Paper%20-%20SRM.pdf>
- [13] Atila Ersahim, Sabee Molloy, Yao-Jin Qian. A Digital Filtration Technique for Scatter-Glare Correction Based on Thickness Estimation. IEEE transactions on Medical imaging. 1995; 14(3): 587-95

- [14] Fieselmann, A., Fischer, D., Hilal, G., Dennerlein, F., Mertelmeier, T., and Uhlenbrock, D.. Full-field digital mammography with grid-less acquisition and software-based scatter correction: investigation of dose saving and image quality. Available from: Society of Photo-Optical Instrumentation Engineers. http://imaging.ubmmmedica.com/all/editorial/diagnosticimaging/pdfs/RePrint_PRIME.pdf
- [15] Danyk A. Y., Radchenko S. P., Sudakov O. O. Optimization of Grid-less Scattering Compensation in X-ray Imaging: Simulation study. IEEE 37th 2017. International Conference on Electronics and Nanotechnology.
- [16] O Diaz, D R Dance, K C Young, P Elangovan, P R Bakic, K Wells. Estimation of scatter radiation in digital breast Tomosynthesis. *Physics in Medicine & Biology*. 2014; 59(15): 4375-90.
- [17] K. Kim, S. Kang, H. Cho, W. Kang, C. Seo, C. Park, D. Lee, H. Lim, H. Lee, G. Kim, S. Park, J. Park, W. Kim, D. Jeon, T. Woo, J. Oh. A model-based radiography restoration method based on simple scatter-degradation scheme for improving image visibility. *Optics and Lasers in Engineering*. 2018; 60-6.
- [18] Boyu Wang, Kevin Yager, Dantong Yu, and Minh Hoai. X-ray Scattering Image Classification Using Deep Learning. *IEEE Winter Conference on Applications of Computer Vision*. 2017.
- [19] Pierre Gravel, Gilles Beaudoin, Jacques A. De Guise. A Method for Modeling Noise in Medical Images. *IEEE TRANSACTIONS ON MEDICAL IMAGING*. 2004. 23(10); 1221-32.
- [20] J L Ducote, S M Molloi. Scatter correction in digital mammography based on image deconvolution. *Physics in Medicine & Biology*. 55 1295. Institute of Physics and Engineering in Medicine (IPEM).
- [21] V. Tóth, C. Brieskorn, B. Renger, D. Mentrup, S. Jockel, F.Lohöfer, M. M. Schwarz, E. J. Rummeny, P. B. Noël. Evaluation of dose reduction potentials of a novel scatter correction software for bedside chest x-ray imaging. *ECR 2015. European Society of Radiology. Electronic Presentation Online System*.

Dosimetric validation of the eclipse Acuros XB dose calculation algorithm for a 6 MV photon beams

Taweap Sanghangthum^{1*} Yot Phimmakone² Sivalee Suriyapee¹

¹Division of Radiation Oncology, Department of Radiology, Faculty of Medicine, Chulalongkorn University, Bangkok, Thailand.

²Radiotherapy center, Mittaphab Hospital, Ministry of Health, Vientiane, Laos.

ARTICLE INFO

Article history:

Received 23 May 2018

Accepted as revised 24 June 2018

Available online 4 August 2018

Keywords:

Acuros XB; dose accuracy; IAEA TRS 430; IMRT; VMAT

ABSTRACT

Background: Acuros XB (AXB) is a novel algorithm implemented to the commercial vender of Varian Eclipse treatment planning system. It is developed to improve the accuracy of dose calculation in external beam radiotherapy, especially in heterogeneity region.

Objectives: To evaluate dosimetric impact of AXB algorithm in basic beam characteristics and clinical applications according to IAEA TRS 430 protocol.

Materials and methods: Scanning percentage depth doses (PDDs) from CC13 ionization chamber and beam profiles at 10 cm depth from PFD diode of 6 MV from TrueBEAM linear accelerator were obtained in water phantom. Output factors were measured at 10 cm depth using CC13 chamber. Doses of fifteen cases in each 3D-CRT, IMRT, and VMAT techniques in solid phantom and CIRS thorax phantom were measured with CC13 chamber. All measurement results were compared with calculation from Eclipse treatment planning system (TPS) using AXB algorithm.

Results: The results showed good agreement between measured and calculated PDDs with δ_1 (high dose & small dose gradient) less than 1.5% and δ_2 (high dose & large dose gradient) within 1.5 mm. Measured profiles also displayed the coincidence results with TPS, which showed δ_2 less than 2 mm, δ_3 (high dose & small dose gradient) within 3%, δ_4 (low dose & small dose gradient) within 3%, and δ_{50-90} within 2 mm as the recommendation from IAEA TRS 430 protocol. Maximum output factors differences were only -1.54%. Clinical plans exhibited the dose differences between measurement and calculation in 3D-CRT, IMRT, and VMAT of $-0.12 \pm 0.38\%$, $-1.59 \pm 0.93\%$, and $0.87 \pm 1.24\%$ for homogeneous phantom and $0.27 \pm 0.29\%$, $-0.60 \pm 1.05\%$, and $-1.12 \pm 0.44\%$ for inhomogeneous phantom, respectively.

Conclusion: Dose differences between measurement and AXB algorithm calculation are within the recommendation of IAEA TRS 430. AXB algorithm is acceptable for dose calculation in external beam radiotherapy.

Introduction

Radiation therapy is one of the most common methods for cancer treatment by delivering high radiation dose to

the tumor while avoiding the normal tissues from doses receiving above the limitations. The accurate dose calculation in clinical situation is important to the modern practice of radiotherapy. New treatment calculation algorithm can increase the capability in accuracy and precision of radiation dose calculation. Acuros XB (AXB) is a novel algorithm implemented to the commercial vender of Varian Eclipse treatment planning system (TPS) (Varian Medical System, Palo Alto, CA) that was developed to administer accuracy and speed in delivering radiation in external beam

* Corresponding author.

Author's Address: Division of Radiation Oncology, Department of Radiology, Faculty of Medicine, Chulalongkorn University, Bangkok, Thailand.

** E-mail address: mairt34@yahoo.com

doi: 10.14456/jams.2018.19

E-ISSN: 2539-6056

radiotherapy. The linear Boltzmann transport equation is used in this algorithm to mainly improve dose calculation accuracy of heterogeneity materials in patient's body such as lung, bone, air, or non-biologic implants.^{1,2,3} This equation is a set of partial differential equations that govern the transport of particles or radiation through matter. The testing of TPS is recommended as a radiotherapy quality assurance framework. Hoffman L et al.⁴ and Zlfodya JM et al.⁵ evaluated the AXB photon dose calculation algorithm by comparing with previous algorithm, analytical anisotropic algorithm (AAA). They found that output factors and percentage depth doses (PDDs) from AXB were comparable with the data from AAA for the measurement in homogeneous phantom and superior to AAA in heterogeneous phantom. Yeh CY et al.⁶ claimed the comparable accuracy of dose distribution to Monte Carlo methods in clinical treatment planning in nasopharyngeal carcinoma.

IAEA Technical Report Series No. 430 (TRS 430) has established the guideline to assist radiotherapy medical physicist to implement the comprehensiveness in commissioning and quality assurance of computerized TPS including software and algorithm for radiation treatment of cancer.⁷ This report described the testing methods and defined the acceptability criteria for external beam dose calculation compared with dose measurement.

The purpose of this research was to verify the dosimetric accuracy of AXB algorithm in Eclipse TPS according to IAEA TRS 430 protocol in basic beam characteristics in terms of PDDs, beam profiles, and output factors and in clinical situations in 3D-conformal radiotherapy (3D-CRT), intensity modulated radiotherapy (IMRT) and volumetric modulated arc therapy (VMAT) plans.

Materials and methods

All of the results presented in this research were based on the calculated beam data from Eclipse AXB

algorithm version 10.0.31 for a 6 MV photon beams from Varian TrueBeam linear accelerator equipped with a millennium 120 MCL (Varian Medical Systems, Palo Alto, CA, USA).

A. Basic beam characteristics:

The PDDs, in-plane and cross-plane beam profiles and output factors were calculated in virtual water phantom in TPS and compared with the measurement results in Blue phantom (IBA Dosimetry GmbH, Schwarzenbruck, Germany). The PDDs of square field sizes (5x5, 10x10, 20x20, 30x30 cm²) and rectangular field sizes (5x10, 20x10, 30x10 cm²) were scanned using the CC13 ionization chamber, while the beam profiles at 10 cm depth with the same opening field sizes in PDDs were scanned using PFD diode detector (IBA Dosimetry GmbH, Schwarzenbruck, Germany). The output factors were measured in square field sizes (5x5, 8x8, 12x12, 15x15, 20x20, 25x25, 30x30, 35x35 cm²) and rectangular field sizes (10x5, 5x10, 5x15, 5x20, 5x30, 10x15, 10x20, 10x25, 10x30, 20x10, 30x10 cm²) using CC13 chamber in solid water phantom. The PDDs and profiles evaluation was assessed by δ_1 , δ_2 , δ_3 , δ_4 and δ_{50-90} parameters according to IAEA TRS 430⁷ and shows in Figure 1. PDD was evaluated in δ_1 (central beam axis for high dose and small dose gradient of the dose difference at 10 cm depth) and δ_2 (build-up region for high dose and large dose gradient of the distance difference at 90% dose), while the profiles were analyzed in δ_2 (beam profile region for high dose and large dose gradient of the distance difference at 40% dose), δ_3 (outside beam central axis for high dose and small dose gradient of the dose difference at 60% of field from central axis), δ_4 (outside beam edges for low dose and small dose gradient of the dose difference at 20% of the field) and δ_{50-90} for a beam fringe for the distance difference between 50% and 90% dose).

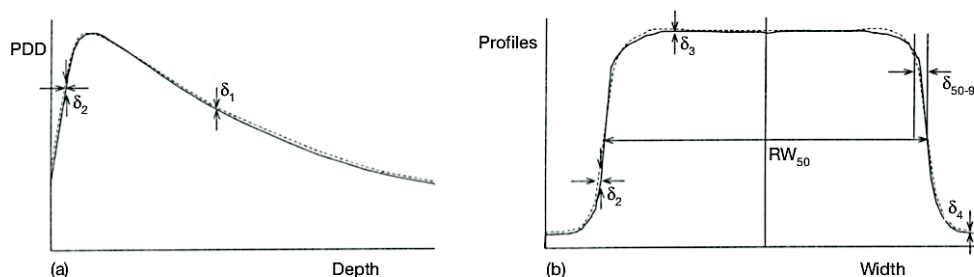


Figure 1 Regions of dose difference evaluation in (a) percentage depth dose, and (b) profile.

B. Clinical applications:

This study compared the dose differences between measurement and calculation in clinical applications for three different techniques; those are 2 to 4-field 3D-CRT, 9-field IMRT and 2.5-arc VMAT. The fifteen cases in each technique with all 6 MV beams were randomly selected in head, chest and pelvic regions and calculated with AXB

algorithm. All of the clinical plans were recalculated and measured in solid water phantom as the homogeneous medium and in CIRS thorax phantom as the inhomogeneous medium as shown in Figure 2 as the example of VMAT QA plan. The size of solid water phantom is 30x30x30 cm³ and the isocenter is at center of phantom. The measurements in both phantoms were performed using CC13 ionization

chamber at isocenter position. Even though this study was performed based on the phantoms measurement, the patient plans were selected to recalculate in phantom. The study

was reviewed and approved by ethical committees of the Faculty of Medicine, Chulalongkorn University.

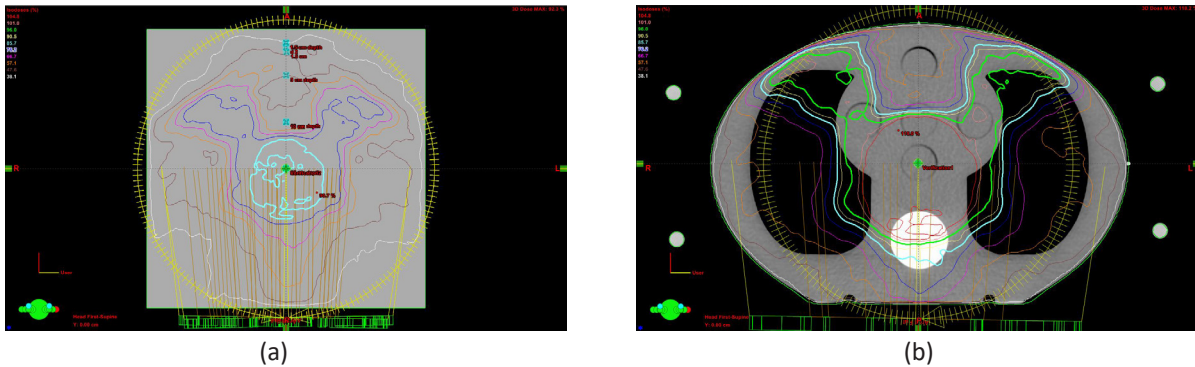


Figure 2 VMAT plan at pelvis region recalculated in (a) solid water phantom and (b) CIRS phantom.

Results

A. Basic beam characteristics:

A.1 Percentage depth doses

Scanning PDD curves along the central axis of 6 MV photon beams in the homogeneous water phantom using CC13 ionization chamber were compared with the calculation

from AXB algorithm and presented in some fields in Figure 3. The open square fields are (a) 10x10 cm² and (b) 20x20 cm², and open rectangular fields are (c) 5x10 cm² and (d) 30x10 cm². The measured PDD data from CC13 chamber are shown in dotted, while the photon dose from AXB calculations are presented in solid lines.

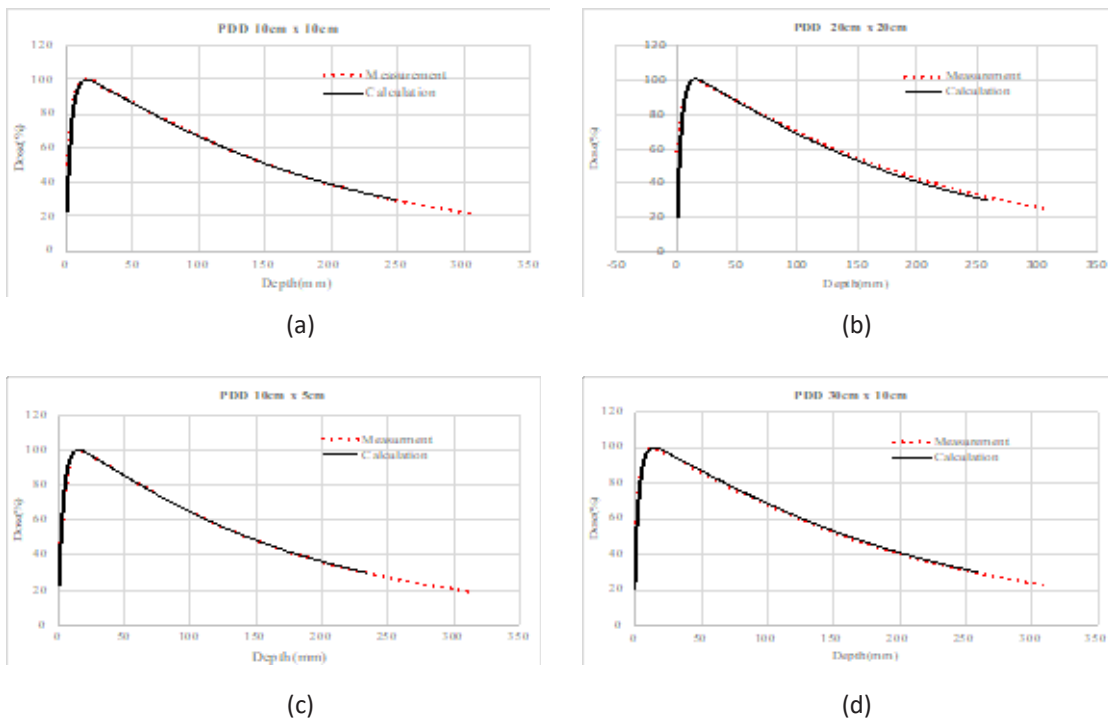


Figure 3 Percentage depth dose curve comparison between measurement and calculation for the square fields of (a) 10x10 cm², (b) 20x20 cm² and rectangular fields of (c) 5x10 cm², (d) 30x10 cm².

Table 1 shows the comparisons of dose differences (δ_1) and distance differences (δ_2) between measurement and calculation for various square and rectangular field sizes. The average dose difference for all test field sizes

between measurement and calculation of δ_1 was only $0.16 \pm 0.64\%$, while the average distance difference of δ_2 was 0.43 ± 0.70 mm.

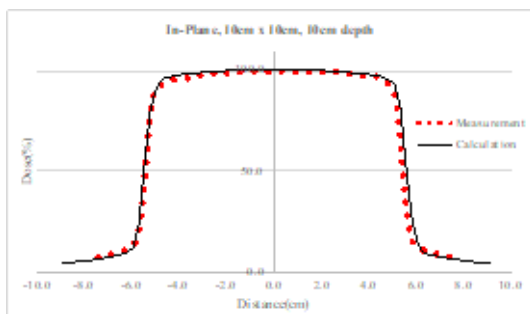
Table 1 Dose (δ_1) and distance (δ_2) differences between measurement and calculation from PDDs in various square and rectangular field sizes for 6 MV photon beams.

Field size (cm ²)	D _{10cm depth}		δ_1 (%)	d _{90% dose}		δ_2 (mm)
	Mea. (%)	Cal. (%)		Mea. (mm)	Cal. (mm)	
5x5	62.40	62.97	0.57	6.38	6.98	0.60
10x10	66.47	66.72	0.25	4.59	6.38	0.79
20x20	69.40	68.24	-1.16	5.25	6.36	1.11
30x30	70.90	71.39	0.49	4.65	5.12	0.47
5x10	64.57	64.45	-0.12	7.76	6.68	-1.08
20x10	67.70	68.24	0.54	5.76	6.36	0.60
30x10	68.00	68.58	0.58	5.71	6.25	0.54
Average			0.16			0.43
Standard deviation			0.64			0.70

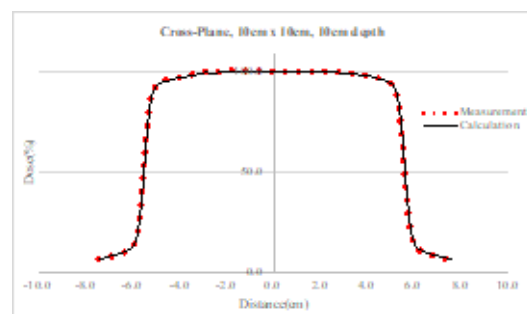
A.2 Beam profiles

Figure 4 displays some beam profiles comparison at 10 cm depth between measurement and calculation for the square fields of (a, e) 10x10 cm² and (b, f) 30x30 cm² and rectangular field size of (c, g) 5x10 cm² and (d, h) 30x10 cm² for in-plane and cross-plane, respectively. The measured

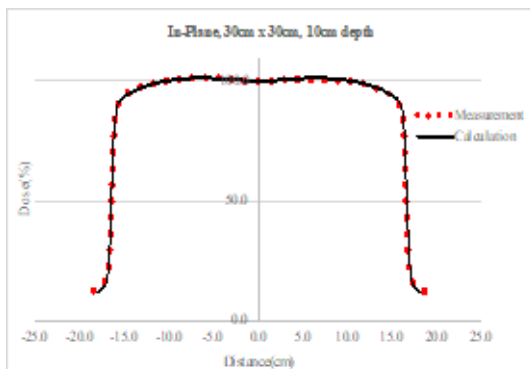
beam profiles data from CC13 chamber are shown in dotted, while the photon dose from AXB calculations are presented in solid lines. Both in-plane and cross-plane profiles showed very good match between measurement and calculation except the penumbra region and at very low dose.



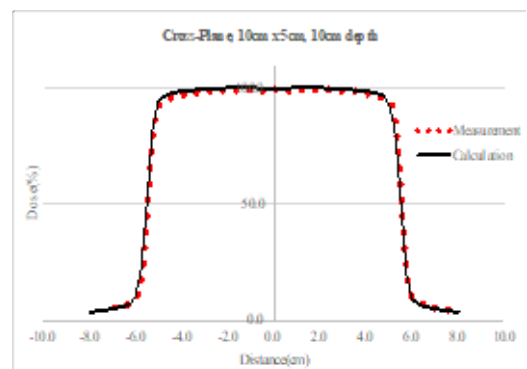
(a)



(e)



(b)



(f)

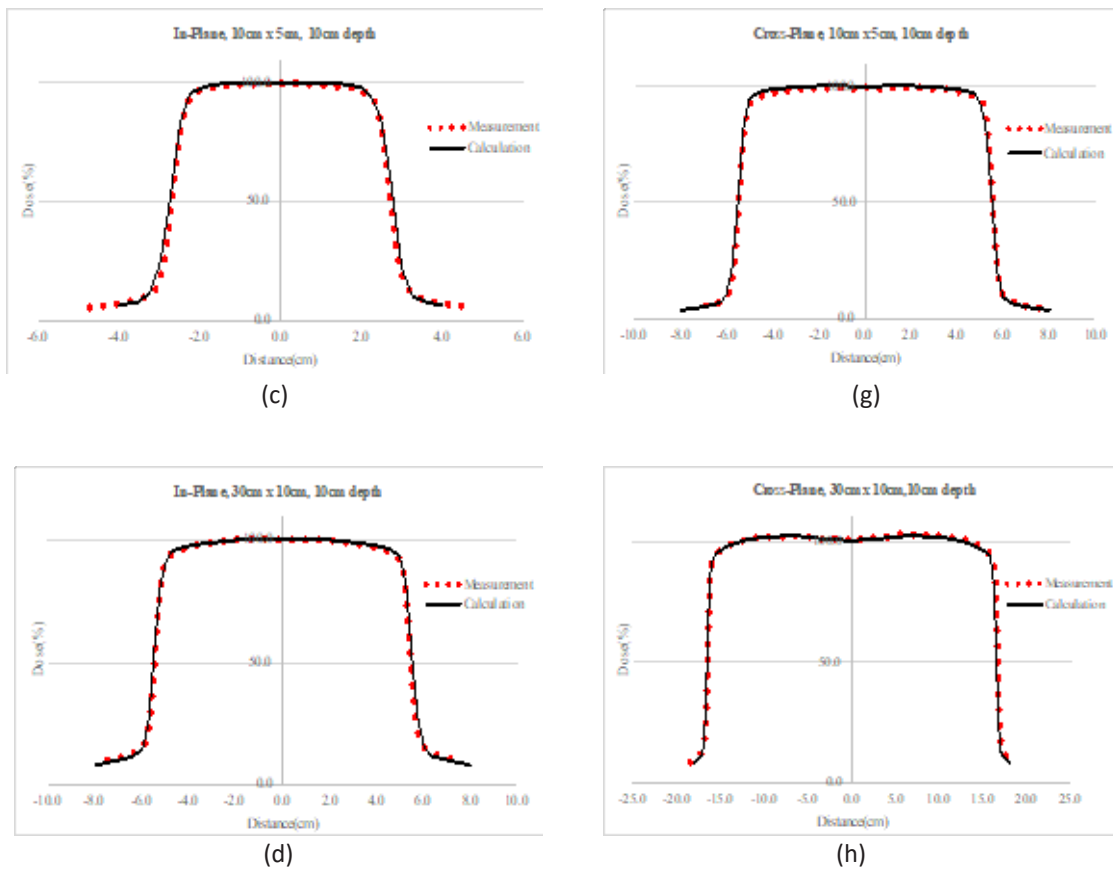


Figure 4 In-plane (a-d) and cross-plane (e-h) profiles comparison between measurement and calculation for field size of 10x10 cm², 30x30 cm², 5x10 cm², and 30x10 cm², respectively.

Table 2 In-plane beam profile comparison between measurement and calculation at 10 cm depth in terms of δ_2 , δ_3 , δ_4 and δ_{50-90} for open square and rectangular field sizes.

F.S (cm ²)	In-plane, 10cm depth											
	d _{40%} dose (mm)		δ_2 (mm)	D _{60%} inner F.S (%)		δ_3 (%)	D _{20%} outer F.S (%)		δ_4 (%)	d _{50%-90%} dose (mm)		δ_{50-90} (mm)
	Mea.	Cal.		Mea.	Cal.		Mea.	Cal.		Mea.	Cal.	
5x5	-27.80	-28.34	-1.54	99.22	99.14	-0.08	8.84	7.84	-1.00	3.35	4.53	1.00
10x10	-55.63	-56.20	-0.57	97.45	98.78	1.33	9.12	8.32	-0.80	4.17	4.41	0.24
20x20	-101.06	-111.41	-1.35	100.99	100.02	-0.97	-	-	-	5.41	5.11	-0.30
30x30	-165.25	-166.27	-1.02	100.83	100.51	-0.32	-	-	-	6.95	6.63	-0.33
10x5	-27.85	-28.47	-0.62	98.75	99.21	0.46	11.11	10.20	-0.91	3.54	4.47	0.93
20x10	-55.24	-56.22	-0.98	98.44	98.47	0.03	11.31	10.29	-1.02	4.26	4.58	0.32
30x10	-55.23	-56.27	-1.04	98.25	98.42	0.17	12.14	11.01	-1.13	4.22	4.62	0.40
Average			-0.87			0.09			-0.97			0.32
Standard deviation			0.30			0.17			0.12			0.53

From Table 2, the average percent dose or distance-to-agreement differences between measurement and calculation of in-plane profile at 10 cm depth for penumbra region of profile for high dose, large dose gradient, δ_2 for 40% dose, was -0.87 ± 0.30 mm with the range from -1.54 mm to -0.57 mm. For the average percent differences of outside central beam axis for high dose and small dose gradient of δ_3 (60% of field size from central axis) was $0.09 \pm 0.17\%$ with the range from -0.97% to 1.33%. The average percent difference for outside beam edges for low dose and small dose gradient, δ_4 for 20% of field size from field edge, was $-0.97 \pm 0.12\%$ with the range from -1.13% to -0.80%. The average difference for beam fringe for the distance from 50% to 90% was 0.32 ± 0.53 mm with the range from -0.33 mm to 1.00 mm.

Table 3 shows the differences of calculated cross-plane

beam profiles from measured data that presents the same trend with the results from Table 2. The average percent deviation between measurement and calculation of cross-plane profile at 10 cm depth for penumbra region of profile for high dose, large dose gradient, δ_2 for 40% dose, was -0.42 ± 0.22 mm with the range from -0.76 mm to -0.09 mm. For the average percent difference of outside central beam axis for high dose and small dose gradient of δ_3 (60% of field size from central axis) was $0.42 \pm 0.29\%$ with the range from -0.20% to 0.65%. The average percent difference for outside beam edges for low dose and small dose gradient, δ_4 for 20% of field size from field edge, was -0.73 ± 0.82 with the range from -1.14% to 0.18%. The average difference for beam fringe for the distance from 50% to 90% was 1.02 ± 0.23 mm with the range from 0.53 mm to 1.18 mm.

Table 3 Cross-plane beam profile comparison between measurement and calculation at 10 cm depth in terms of δ_2 , δ_3 , δ_4 and δ_{50-90} for open square and rectangular field sizes.

F.S. (cm ²)	Cross-plane, 10cm depth											
	d _{40% dose} (mm)		δ_2 (mm)	D _{60% inner F.S} (%)		δ_3 (%)	D _{20% outer F.S} (%)		δ_4 (%)	d _{50%-90%dose} (mm)		δ_{50-90} (mm)
	Mea.	Cal.		Mea.	Cal.		Mea.	Cal.		Mea.	Cal.	
5x5	-28.26	-29.02	-0.76	98.73	99.17	0.44	8.07	8.25	0.18	3.25	3.78	0.53
10x10	-56.28	-56.37	-0.09	98.93	98.73	-0.20	9.40	7.99	-1.14	3.93	5.01	1.08
20x20	-111.11	-111.59	-0.48	99.43	100.02	0.59	-	-	-	4.88	6.05	1.17
30x30	-166.03	-166.60	-0.57	100.00	100.57	0.57	-	-	-	5.98	6.96	0.98
10x5	-55.88	-56.19	-0.31	98.77	99.42	0.65	6.42	5.46	-0.96	3.45	4.59	1.05
20x10	-111.04	-111.27	-0.23	100.33	100.64	0.31	-	-	-	4.20	5.32	1.12
30x10	-165.94	-166.43	-0.49	100.89	101.44	0.55	-	-	-	4.34	5.52	1.18
Average			-0.42			0.42			-0.73			1.02
Standard deviation			0.22			0.29			0.82			0.23

A.3 Output Factors

Table 4 shows the percent output factor differences between measurement and calculation of various square and rectangular fields. The average of output factor difference

between measurement and calculation were $0.61 \pm 0.85\%$ with the maximum of -1.54% at the largest field size of 35x35 cm².

Table 4 Measured and calculated output factors for various square and rectangular fields.

Field size (cm ²)	Measurement	Calculation	Difference (%)
5x5	0.90	0.89	-0.46
8x8	0.97	0.96	-0.37
12x12	1.03	1.03	-0.13
15x15	1.06	1.06	0.02
20x20	1.10	1.10	0.00
25x25	1.13	1.13	0.02
30x30	1.16	1.14	-1.49
35x35	1.17	1.15	-1.54
10x5	0.94	0.93	-1.22
5x10	0.93	0.94	0.59
5x15	0.95	0.96	1.05
5x20	0.95	0.96	1.12
5x30	0.96	0.97	1.14
10x15	1.02	1.03	0.42
10x20	1.04	1.04	0.57
10x25	1.04	1.05	0.71
10x30	1.05	1.06	0.80
20x10	1.04	1.04	-0.44
30x10	1.06	1.05	-0.85
Average			0.61
Standard deviation			0.85

B. Clinical applications

B.1 Homogeneous medium in solid water phantom

Figure 5 is the isocenter dose differences between measurement and calculation for 3D-CRT, IMRT and VMAT plans in head (No. 1 to 5), chest (No. 6 to 10) and pelvic (No. 11 to 15) regions, while the data in Table 5, Table 6, and Table 7 show the results performed for the clinical situation in 3D-CRT, IMRT, and VMAT plans, respectively.

The dose comparison of head, chest and pelvic regions between calculating from Acuros XB and measuring from ionization chamber in homogeneous solid water phantom were very good agreement between with average dose differences of only $-0.12 \pm 0.38\%$ (range from -0.52 to 0.71%), $-1.59 \pm 0.93\%$ (range from -2.95 to -0.18%), and $0.87 \pm 1.24\%$ (range from -1.38 to 2.70%) for 3D-CRT, IMRT, and VMAT plans, respectively.

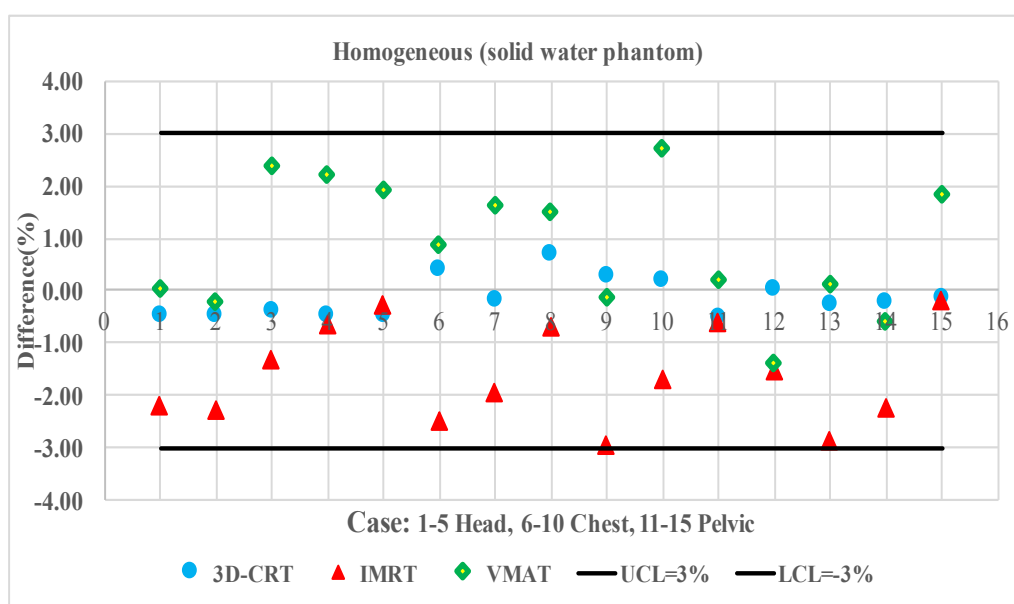


Figure 5 The percentage of dose difference between measurement and calculation in 3D-CRT, IMRT and VMAT plans of head, chest and pelvic regions in homogeneous solid water phantom.

Table 5 Dose difference between measurement and calculation in solid water phantom as the homogeneous medium for 3D-CRT technique.

Case No.	Regions	Measurement (cGy)	Calculation (cGy)	Difference (%)
1	Head	301.35	300	-0.45
2	Head	301.35	300	-0.45
3	Head	301.16	300	-0.38
4	Head	301.40	300	-0.47
5	Head	301.35	300	-0.45
6	Chest	298.76	300	0.42
7	Chest	300.52	300	-0.17
8	Chest	198.58	200	0.71
9	Chest	299.10	300	0.30
10	Chest	199.61	200	0.19
11	Pelvic	180.94	180	-0.52
12	Pelvic	179.96	180	0.02
13	Pelvic	180.45	180	-0.25
14	Pelvic	180.35	180	-0.19
15	Pelvic	180.35	180	-0.14
Average				-0.12
Standard deviation				0.38

Table 6 Dose difference between measurement and calculation in solid water phantom as the homogeneous medium for IMRT technique.

Case No.	Regions	Measurement (cGy)	Calculation (cGy)	Difference (%)
1	Head	306.75	300	-2.20
2	Head	204.69	200	-2.29
3	Head	202.63	200	-1.30
4	Head	201.28	200	-0.63
5	Head	200.53	200	-0.26
6	Chest	205.12	200	-2.49
7	Chest	203.95	200	-1.94
8	Chest	201.36	200	-0.67
9	Chest	206.07	200	-2.95
10	Chest	203.45	200	-1.70
11	Pelvic	181.09	180	-0.60
12	Pelvic	203.08	200	-1.52
13	Pelvic	236.77	230	-2.85
14	Pelvic	229.10	224	-2.22
15	Pelvic	200.37	200	-0.18
Average				-1.59
Standard deviation				0.93

Table 7 Dose difference between measurement and calculation in solid water phantom as the homogeneous medium for VMAT technique.

Case No.	Regions	Measurement (cGy)	Calculation (cGy)	Difference (%)
1	Head	179.91	180	0.05
2	Head	200.44	200	-0.22
3	Head	175.84	180	2.37
4	Head	215.20	220	2.23
5	Head	176.61	180	1.92
6	Chest	118.94	120	0.89
7	Chest	196.80	200	1.63
8	Chest	197.01	200	1.52
9	Chest	212.40	212.1	-0.14
10	Chest	259.00	266	2.70
11	Pelvic	179.65	180	0.19
12	Pelvic	182.51	180	-1.38
13	Pelvic	199.74	200	0.13
14	Pelvic	181.09	180	-0.60
15	Pelvic	294.62	300	1.82
Average				0.87
Standard deviation				1.24

B.2 Inhomogeneous medium in CIRS thorax phantom

Table 8, 9, and 10 are the dose differences between measurement and calculation for 3D-CRT, IMRT, and VMAT plans in CIRS thorax phantom, respectively. The average dose difference in 3D-CRT was only 0.27±0.29% with the range from -0.37% to 0.61%. The average dose difference in IMRT was -0.60±1.05% with the range from -2.27% to 0.53%. The VMAT showed the average dose difference of -1.12±0.44% with the range from -1.90% to -0.34%. The

data are presented in Figure 6 that showed the dose differences for 3D-CRT, IMRT and VMAT plans in CIRS thorax phantom for head (no. 1 to 5), chest (no. 6 to 10) and pelvic (no. 11 to 15) regions. In 3D-CRT, the differences were almost the same pattern with the results from homogeneous phantom. The 3D-CRT (circle) exhibited lesser deviation of dose differences compared with IMRT (triangle) and VMAT (diamond) techniques.

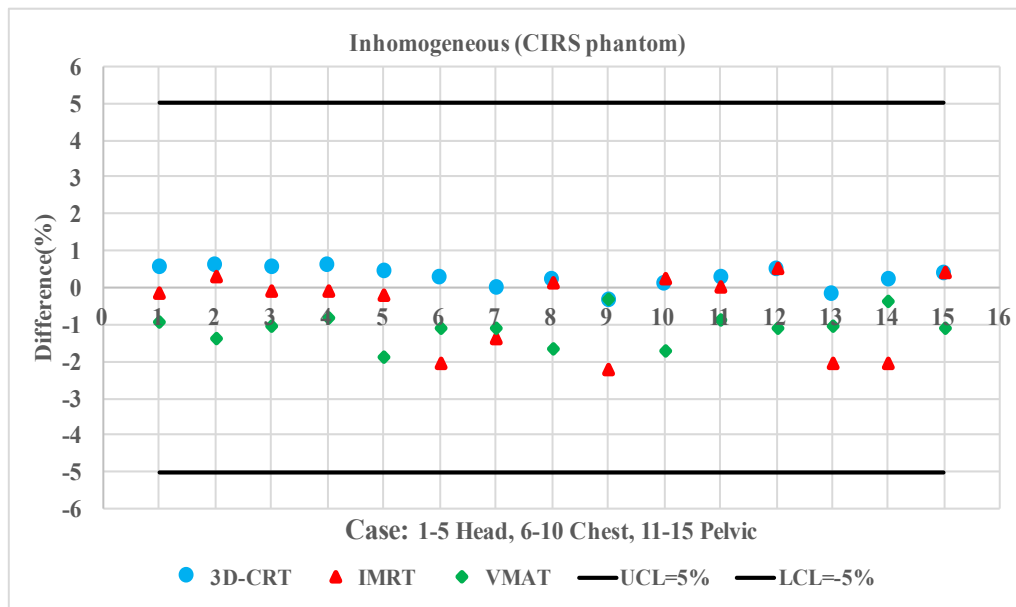


Figure 6 Percentage of dose difference between measurement and calculation in 3D-CRT, IMRT and VMAT plans of head, chest and pelvic region in CIRS thorax inhomogeneous phantom.

Table 8 Dose difference between measurement and calculation in CIRS thorax phantom as the inhomogeneous medium for 3D-CRT technique.

Case No.	Regions	Measurement (cGy)	Calculation (cGy)	Difference (%)
1	Head	298.44	300	0.52
2	Head	298.17	300	0.61
3	Head	298.44	300	0.52
4	Head	298.17	300	0.61
5	Head	298.70	300	0.43
6	Chest	299.24	300	0.25
7	Chest	300.04	300	-0.01
8	Chest	199.60	200	0.20
9	Chest	301.10	300	-0.37
10	Chest	199.84	200	0.08
11	Pelvic	179.17	180	0.46
12	Pelvic	180.32	180	-0.18
13	Pelvic	179.65	180	0.20
14	Pelvic	179.31	180	0.38
15	Pelvic	179.25	180	0.27
Average				0.27
Standard deviation				0.29

Table 9 Dose difference between measurement and calculation in the CIRS thorax phantom as the inhomogeneous medium for IMRT technique.

Case No.	Regions	Measurement (cGy)	Calculation (cGy)	Difference (%)
1	Head	300.51	300	-0.17
2	Head	199.43	200	0.29
3	Head	200.18	200	-0.09
4	Head	200.18	200	-0.09
5	Head	200.45	200	-0.22
6	Chest	202.88	200	-1.42
7	Chest	199.80	200	0.10
8	Chest	204.64	200	-2.27
9	Chest	199.51	200	0.25
10	Chest	202.88	200	-1.42
11	Pelvic	180.04	180	-0.02
12	Pelvic	198.95	200	0.53
13	Pelvic	234.93	230	-2.10
14	Pelvic	228.73	224	-2.07
15	Pelvic	199.22	200	0.39
Average				-0.60
Standard deviation				1.05

Table 10 Dose difference between measurement and calculation in the CIRS thorax phantom as the inhomogeneous medium for VMAT technique.

Case No.	Regions	Measurement (cGy)	Calculation (cGy)	Difference (%)
1	Head	222.08	220	-0.94
2	Head	182.53	180	-1.39
3	Head	202.19	200	-1.08
4	Head	181.53	180	-0.85
5	Head	203.88	200	-1.90
6	Chest	121.38	120	-1.14
7	Chest	303.45	300	-1.14
8	Chest	203.39	200	-1.67
9	Chest	200.68	200	-0.34
10	Chest	203.56	200	-1.17
11	Pelvic	302.65	300	-0.87
12	Pelvic	182.04	180	-1.12
13	Pelvic	204.71	202.5	-1.08
14	Pelvic	200.79	200	-0.39
15	Pelvic	218.46	216	-1.13
Average				-1.12
Standard deviation				0.44

Discussion

A. Basic beam characteristics:

A.1 Percentage depth doses

From Figure 3 and Table 1, the very good agreement between calculated and measured PDD for all fields were observed in the linear part of the curve but slightly difference at the build-up region and at very lower dose of deeper depth. The results of average difference of δ_1 and δ_2 in PDD in this study agreed with Hoffmann L et al.⁴ studied who showed the differences of PDD within 1% in dose and 1 mm in distance to agreement. Following the IAEA TRS 430, the tolerance limit of δ_1 is 2.0% and δ_2 is 2.0 mm. The maximum dose difference at 10 cm depth, δ_1 , was found at -1.16% for 20x20 cm² field size, while the maximum distance difference at 90% dose before buildup region, δ_2 , was 1.11 mm for 20x20 cm² field size. These small errors might be due to the setup uncertainty during measurement and error of dose calculation algorithm in the buildup region.

A.2 Beam profiles

The excellent agreement between measured and calculated beam profiles in both in and cross-planes were found in all field sizes, however, the curves showed slightly differences at the penumbra region and at very low dose. When the quantitative evaluation was used, we found that the differences were within the acceptability criteria for external dose calculation according to IAEA TRS 430 of 2 mm for δ_2 , 3% for δ_3 , 3% for δ_4 , and 2 mm for δ_{50-90} as shown in Table 2 and 3 for in-plane and cross-plane results,

respectively. The δ_4 in the large field from 20 cm in any side cannot interpret the results due to the limitation of water phantom size for beam scanning.

A.3 Output Factors

From the results of output factors, the average difference between measurement and calculation were $0.61 \pm 0.85\%$ and it seems to be the lesser deviation was detected at the smaller field. This study showed slightly larger differences than L. Hoffmann et al.², who presented the maximum deviation of output factor at 0.50% that might be due to the small chamber selected in our measurement that difference from 0.6 cc farmer chamber from Hoffmann. However, our output factor results were still within the limitation of 2.00% for all field sizes.⁷

B. Clinical applications

B.1 Homogeneous medium in solid water phantom

The 3D-CRT plans showed almost comparable and small deviation of isocenter dose difference between planning and calculation in all cases as shown in circle symbol in Figure 5 that might be due to the simple plan in 3D-CRT. On the other hand, the average dose differences of IMRT and VMAT plans were higher than in 3D-CRT technique because IMRT and VMAT were the complicated plans and the chamber position may be located in the high dose gradient region. However, the errors from all of the test cases were still within $\pm 3.00\%$ limitation recommended by IAEA TRS430.³ The results were agreed with Han T et al.⁸ studied who presented the dose differences in the range of 0.10% to 3.60%. The variation among head, chest and

pelvic regions were not much different because these plans were recalculated in homogeneous water phantom. Therefore, the inhomogeneity correction was not considered.

B.2 Inhomogeneous medium in CIRS thorax phantom

The CIRS thorax phantom was selected as the inhomogeneous medium and used to compare the dose differences at isocenter between measurement and calculation. The results showed very good agreement in all treatment regions and techniques as shown in Figure 6 and Table 8 to 10 because Acuros XB algorithm was designed to improve the accuracy dose calculation in heterogeneity medium than the previous calculation algorithm, AAA. The variation of dose difference among regions was not much in 3D-CRT but slightly fluctuated in IMRT and VMAT due to the plan complexity of advanced treatment techniques that very sensitive to position of chamber. Among the regions, IMRT and VMAT plans displayed less variation in head compared to chest and pelvic due to lesser inhomogeneity area in head area.

Conclusion

PDDs and profiles between measurement and calculation are in good agreement except the tails of beam profiles for very small dose and small gradient. The average output differences were $0.61 \pm 0.85\%$. The clinical cases are very excellent agreement between measurement and calculation in both homogeneous (within 3.00%) and inhomogeneous (within 5.00%) phantoms for all 3D, IMRT and VMAT techniques. Therefore, the Acuros XB algorithm is acceptable for dose calculation in external beam radiotherapy in case of isocenter point dose verification. However, to fulfill the verification of dose calculation algorithm in clinical situation, the dose distribution in comparison with gamma criteria analysis should be further study in IMRT and VMAT planning.

Conflicts of interest

Conflicts of interest

References

- [1] Lloyd SA, Ansbacher W. Evaluation of an analytic linear Boltzmann transport equation solver for high-density inhomogeneities. *Med Phys* 2013; 40:0117071-5.
- [2] Gregory AF, Wareing T, Archambault Y, Thompson S. Acuros XB advanced dose calculation for the Eclipse™ treatment planning system. Varian Medical System, Palo, Alto, CA. 2015. Available from: https://www.varian.com/sites/default/files/resource_attachments/AcurosXBClinicalPerspectives_0.pdf
- [3] Vassiliev ON, Wareing TA, McGhee J, Failla G, Salehpour MR, Mourtada F. Validation of a new grid-based Boltzmann equation for solver dose calculation in radiotherapy with photon beams. *Phys Med Biol* 2010; 55: 581-98.
- [4] Hoffmann L, Jørgensen MB, Muren LP, Petersen JB., Clinical validation of the Acuros XB photon dose calculation algorithm, a grid-based Boltzmann equation solver. *Acta Oncol* 2012; 51(3): 376-85.
- [5] Zifodya JM, Challens CH, Hsieh WL, From AAA to Acuros XB-clinical implications of selecting either Acuros XB dose-to-water or dose-to-medium. *Australas Phys Eng Sci Med* 2016; 39(2): 431-9.
- [6] Yeh PCY, Lee CC, Chao TC, Tung CJ. Monte Carlo evaluation of Acuros XB dose calculation Algorithm for intensity modulated radiation therapy of nasopharyngeal carcinoma. *Rad Phys Chem* 2017;140: 419-22.
- [7] International Atomic Energy Agency. Commissioning and quality assurance of computerized planning systems for radiation treatment of cancer: TRS Report No 430. Vienna; Austria: 2004.
- [8] Han T, Mourtada F, Kisling K, Mikell J, Followill D, Howell R. Experimental validation of deterministic Acuros XB algorithm for IMRT and VMAT dose calculations with the Radiological Physics Center's head and neck phantom. *Med Phys* 2012; 39(4): 2193-202.

Comparison of post processing methods between Java Magnetic Resonance User Interface (jMRUI) and Totally Automatic Robust Quantitation in NMR (TARQUIN) software for liver fat quantification

Duanghathai Pasanta¹ Montree Tungjai¹ Sirirat Chancharunee² Suchart Kiatwattanacharoen¹ Suchart Kothan^{1*}

¹Department of Radiologic Technology, Faculty of Associated Medical Sciences, Chiang Mai University, Chiang Mai, Thailand.

²Department of Chemistry, Faculty of Science, Chiang Mai University, Chiang Mai, Thailand

ARTICLE INFO

Article history:

Received 4 June 2018

Accepted as revised July 2018

Available online 4 August 2018

Keywords:

Proton magnetic resonance spectroscopy, liver fat, jMRUI, TARQUIN, post processing

ABSTRACT

Background: Proton magnetic resonance spectroscopy or ¹H MRS is a validated and non-invasive method used for studying liver fat. However, the metabolite spectra obtained by ¹H MRS require a post-processing method for accurate liver fat quantification. Various spectrum analysis software has been developed and is being used in many studies. To the best of our knowledge, no comparisons between spectrum analysis software for liver fat quantification have yet been completed.

Objectives: To compare the post processing methods between java-based graphical for MR user interface packages (jMRUI) and totally automatic robust quantitation in NMR (TARQUIN) software for optimal liver fat quantification.

Materials and methods: ¹H MRS spectrum from the right lobe of the liver was obtained for post processing. Liver fat qualification was done by AMARES algorithms on jMRUI software, and automatic quantification algorithms was initiated by TARQUIN software. A total of 30 subjects participated in this study. Subjects were separated into a control group (n=15) and an overweight group (n=15) for liver fat quantification. Liver lipids at 0.9 ppm (-CH₃ lipids) and 1.3 ppm (-CH₂ lipids) were fitted and quantified. The results obtained from both jMRUI and TARQUIN post processing software packages for both groups were then compared.

Results: A strong and moderate correlation of signal intensity between jMRUI and TARQUIN software was found (total lipids, r=0.836, p<0.001; -CH₂ lipids, r=0.848, p<0.001; -CH₃ lipids, r=0.520, and p<0.003). Liver lipid levels were generally higher in the overweight group. There was a 2.35 times level of change in the overweight group compared to control from jMRUI, and there was a 2.16 times level of change in the overweight group compared to control from TARQUIN. There was no statistical differences between the programs (p=0.762).

Conclusion: Both jMRUI and TARQUIN are feasible post processing tools for ¹H MRS liver spectrum fitting for liver lipids quantification.

Introduction

Non-alcoholic fatty liver disease (NAFLD) is a type of chronic liver disease that is caused by an accumulation

of lipids in hepatocytes.¹ NAFLD is considered to be a global epidemic that leads to many other liver diseases and health complications such as liver inflammation (hepatitis), liver cirrhosis, and hepatocellular carcinoma.^{1, 2} A 25% prevalence rate was found to exist in Asian countries, which is now as high as that of western countries.³ A nationwide study in Thailand from 2015 found that liver-related diseases led Non-alcoholic fatty liver disease (NAFLD) to higher in-hospital mortality rates.⁴ Liver fat

* Corresponding author.

Author's Address: Department of Radiologic Technology, Faculty of Associated Medical Sciences, Chiang Mai University, Chiang Mai, Thailand.

** E-mail address: suchart.kothan@cmu.ac.th

doi: 10.14456/jams.2018.20

E-ISSN: 2539-6056

accumulation can be induced by an excessive fat intake, metabolism impairment, and from being overweight or obese. Thus, an accurate and effective method for liver lipid determination is truly needed.

Proton magnetic resonance spectroscopy (^1H MRS) is a non-invasive technique that is known for its accuracy for liver lipid assessment and is also the primary validation method used for liver lipids assessment.⁵⁻⁷ Being non-invasive, it is a suitable technique for follow up in longitudinal studies done on liver lipids in both clinical and research applications. Previous studies on ^1H MRS have found that body mass index (BMI) is associated with higher levels of liver lipids.^{8,9} However, ^1H MRS liver lipid signals were obtained as spectrum and require post-processing methods for ^1H MRS data. There are many available software packages for data analysis. Two popular ones are java-based graphical for MR user interface package (jMRUI), and totally automatic robust quantitation in NMR (TARQUIN).¹⁰⁻¹² jMRUI is a software package that is freely available on the jMRUI website (<http://www.jmrui.eu>) for non-commercial use. It provides many algorithms for spectra fitting and correction, and was included in an extensive list of literature as a very popular method of data analysis. One popular algorithm for spectrum fitting is the Advanced Method for Accurate, Robust, and Efficient Spectral Fitting or AMARES, which can import prior knowledge for better spectrum fitting.¹³ However, jMRUI requires a user intervention, and a degree of knowledge during the post processing is necessary for accurate quantification. This maybe time consuming, and therefore is not suitable for liver fat assessment in clinical settings. On the other hand, TARQUIN provides an automatic quantification of metabolites based on a basis spectra model in time domain, and contains some preprocessing tools for spectrum fitting.⁶ These features make it a more viable and convenient method for everyday use. To the best of our knowledge, there have been no previous studies done about the comparison of liver lipid assessment between jMRUI and TARQUIN software packages. If this two-quantification model can be used for liver lipid assessment and can differentiate liver lipid levels between normal weight and overweight people, this data will be beneficial in both clinical and research settings. The aim of this study is to compare two software packages for liver lipid assessment in both a normal weight group (BMI 18.5-24.9 kg/m²) and an overweight group (BMI \geq 25 kg/m²).

Materials and methods

Study population

Thirty healthy subjects composed of both males and females aged between 20-35 years of age participated in this study. Inclusion criteria for study subjects is based on the following criteria: i) healthy with no known liver disease, liver injury, and chronic disease such as cancer, diabetes, or hypertension ii) no history of virus hepatitis B and C infection iii) drink alcohol <30 g/day for men and <20 g/day for women¹⁴ iv) engage in moderate physical activity. The subjects were separated into two groups. The control group (n=15) with BMI in normal range (BMI 18.5-

24.9 kg/m²) as determined by the World Health Organization (WHO), and the overweight group (n=15) with BMIs in overweight range (BMI>25 kg/m²).¹⁵ 10 ml of fasting blood was drawn from subjects in both groups and basic laboratory blood tests for blood lipid level were performed. The blood tests focused on cholesterol (Cho), high-density lipoprotein (HDL), very-low density lipoprotein (VLDL), triglyceride (TG), glucose (Glu), and glycosylated hemoglobin A (HbA1c). Low-density lipoprotein (LDL) concentration was calculated from an adjustable LDL estimation equation.^{16,17} Each subject gave their written informed consent after the procedure was fully explained and understood. This study was approved by the Ethics Committee of the Faculty of Associated Medical Science, Chiang Mai University, Chiang Mai, Thailand.

Liver lipids assessment

Magnetic resonance imaging (MRI) 1.5 T Achieva (Philips Medical Systems, Best, The Netherlands) was used in this study. Subjects were told to lie down in a supine position. The SENSE cardiac coil was then placed over the liver with gated respiratory for both image and ^1H MRS acquisition. First, localization images were obtained, then T2 weighted images of liver were obtained in the coronal and sagittal planes (Echo time (TE) =80 ms, Repetition time (TR) =871 ms, and slice thickness =6 mm) to ensure voxel localization. The automatic shimming protocol available on MRI was performed. Later, single-voxel ^1H MRS acquisition for liver lipids assessment was done with Point resolved spectroscopy (PRESS) pulse sequence (TE=43 ms, TR=2000 ms, Number of signal averages =96, Data point =512, and band width=1,000 Hz) with water suppression. Voxel size of 10 \times 10 \times 10 mm was carefully placed in the right lobe of the liver, carefully avoiding any bile ducts and blood vessels.

Spectra analysis

^1H MRS spectra that were obtained from the liver were analyzed by two types of software packages: jMRUI version 6.0 beta and TARQUIN version 4.3.10. jMRUI is a highly flexible software package that provides a wide range of algorithms for ^1H MRS signal processing, and includes preprocessing tools and peak fitting. In this study, an AMARES algorithm was applied for spectra fitting in time domain. Water signal residual was suppressed by Hankel Lanczos singular value decomposition (HLSVD) algorithms that were provided in jMRUI software.¹⁸ Any prior knowledge regarding estimates of liver metabolite peaks was provided for the algorithm, as described in a previous publication.¹⁹ TARQUIN has more advantages than jMRUI since it enables automatic post processing for spectra metabolites, and wide ranges of ^1H MRS data can be accepted. TARQUIN is a time domain fitting algorithm by a least square projection used to determine signal amplitude. Notable features are that TARQUIN imposes soft constraints with basis in-vivo spectra data set that includes macromolecules, lipids, and metabolites to avoid possible over fitting of spectrum.¹⁰ The signal truncation in time domain and HLSVD water removal was applied for baseline correction.²⁰ As it is an automatic process, it will reduce user bias and variability on spectrum analysis. The liver lipids signals of interest on liver spectra was at 0.9 parts per million (ppm) for $-\text{CH}_3$

lipids and 1.3 ppm for -CH₂ lipids. The lipids signals were corrected for T1 and T2 relaxation by a method described elsewhere.²¹ Next, corrected liver lipids signals were calculated into a ratio of each lipid (-CH₃ lipids, -CH₂ lipids) to total lipid (-CH₃ lipids + -CH₂ lipids).

Statistical analysis

All data is expressed as mean±standard deviation (SD), unless state otherwise. All statistical analysis was performed on SPSS version 17.0 (SPSS Inc., Chicago). The Kolmogorov Smirnov test was used to determine data distribution. Comparison of blood laboratory tests between groups were performed using Mann-Whitney U test. Comparisons of lipids ratio to total lipids and liver lipids signal intensity were performed between each software package using a pair sample t-test. A Pearson correlation was used to assess the relationship between signal intensity from each of lipid group obtained by jMRUI and TARQUIN. P<0.05 were considered statistically significant.

Results

All subjects were invited to participate in this study during the period of January 2017 to March 2017. A total of 30 subjects were given blood tests and ¹H MRS was performed for liver fat at the Associated Medical Sciences Clinical Service Center, Chiang Mai University. The age, BMI, and laboratory blood test results of study subjects are shown in Table 1. Laboratory blood test results showed significantly higher BMI, TG, Glu, and significantly lower HDL in the overweight group compared to control group. LDL, HbA1c, and Cho was also found to be higher in the overweight group, but this tendency was not statistically

significant. The representative ¹H MRS liver spectra fitting from both programs are shown in Figure 1. The water suppressed spectra show the liver lipids peaks at the following chemical shifts: -CH₃ lipids (0.9 ppm) and -CH₂ lipids (1.3 ppm). These two lipids signal intensities were then calculated into total liver lipids. Coefficient co-variation (CV) of liver lipids signal intensity and total liver lipids were similar for both groups (data not shown). In general, -CH₃ lipids, -CH₂ lipids, and total lipids in overweight group showed higher signal intensity than in the control group. In addition, CV values showed consistency among the signal intensities obtained from each group when analyzed across the software packages. Scatter plots of signal intensity of liver lipids between two software packages are shown in Figure 2. The Pearson correlation coefficient showed a strong positive correlation of signal intensity obtained from both programs. However, the correlation of -CH₃ lipids signal intensity between the two software packages was found to be moderate, but remained statistically significant. Total lipids of control group were set as the reference value as total lipid for the comparison of liver fat between the groups and is shown in Figure 3. The figure reveals increasing liver fat in both algorithms as having a similar pattern, and this tendency was not found to be statistically significant across the software packages. However, it should be noted that total liver lipids acquired from TARQUIN were slightly lower by around 18%. The -CH₃ lipids and -CH₂ lipids were then calculated into ratio to total lipids (-CH₃ lipids + -CH₂ lipids) as shown in Table 2. Lipids ratio from -CH₃ lipids and -CH₂ lipids to total is almost the same value in the same lipids group, with no significant correlation taking place between jMRUI and TARQUIN.

Table 1 Characterize of subjects from control group and overweight group.

	Control group (n=15)	Overweight group (n=15)	P-values
Sex (male/female)	(8/7)	(11/4)	-
age	22.0±1.0	22.8±2.1	0.762
BMI	20.8±2.2	29.1±1.4	<0.001*
Cho	195.8±37.2	212.5±37.5	0.751
Tri	71.9±20.3	110.7±58.3	0.022*
HDL	59.2±12.4	49.2±8.1	0.004*
LDL	120.2±32.9	140.7±34.4	0.496
Glu	82.2±4.6	90.3±4.7	0.002*
HbA1c	5.2±0.3	5.4±0.3	0.142

Note: *P<0.05 indicated statistically significant

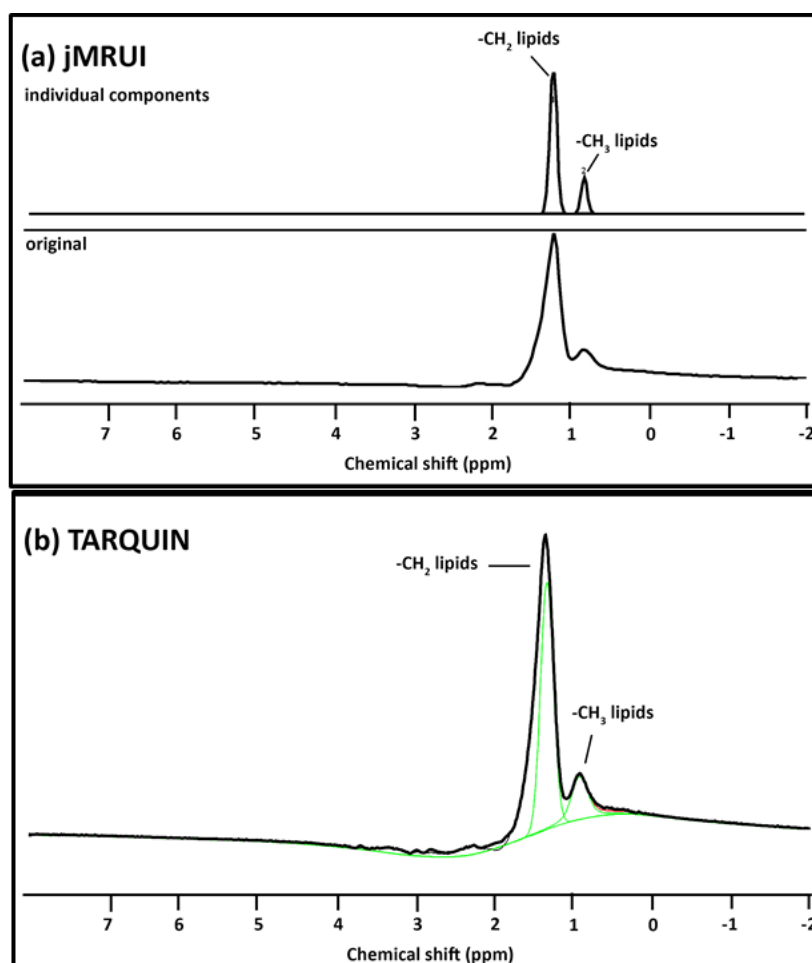


Figure 1 Representative liver spectra with suppressed water signal. (a) jMRUI show fitted signal (top) original signal (bottom) and (b) TARQUIN software package show fitted signal (green) original signal (black). ppm; part per million.

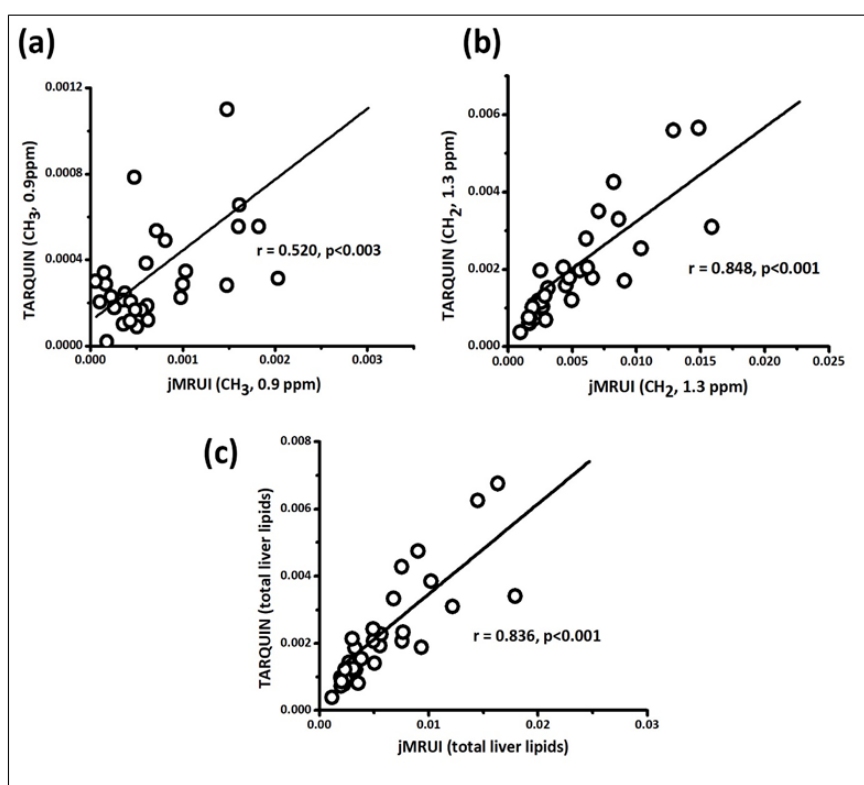


Figure 2 Association between signal intensity of liver lipids between jMRUI and TARQUIN software package from both groups (a) signal intensity of -CH₃ lipids (b) signal intensity of -CH₂ lipids (c) signal intensity of total lipids.

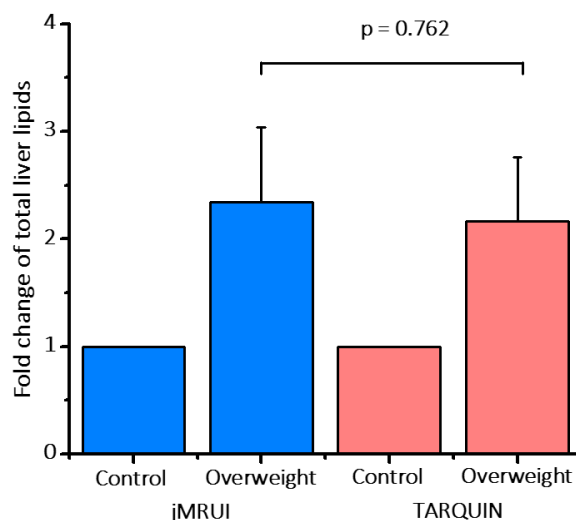


Figure 3 Folds change of signal intensity of total liver lipids from jMRUI and TARQUIN software packages with control group as reference value.

Table 2 Liver lipids signals ratio to total lipids and from each group.

	Control		Overweight	
	-CH ₃ lipids/total liver lipids	-CH ₂ lipids/total liver lipids	-CH ₃ lipids/total liver lipids	-CH ₂ lipids/total liver lipids
jMRUI	0.14±0.06	0.86±0.06	0.12±0.07	0.87±0.07
TARQUIN	0.16±0.05	0.84±0.05	0.13±0.03	0.87±0.03
P-values	0.182	0.182	0.977	0.977

Note: jMRUI, java-based graphical for MR user interface package; TARQUIN, totally automatic robust quantitation in NMR

Discussion

Number of NAFLD cases and its prevalence are rising significantly from 15% in 2005 to 24% globally in 2010.^{1, 22} Moreover, NAFLD has found to often be accompanied with obesity, dyslipidemia, insulin resistance, and other metabolic syndromes.²³⁻²⁵ Liver fat accumulation of more than 5% is considered as NAFLD.²⁴ This widespread problem underscores the need for an accurate and non-invasive technique for liver fat assessment for both clinical applications and research to be developed. While biopsy is the gold standard for assessing liver lipids and is widely available in hospitals, it is an invasive technique, and also is not suitable for longitudinal follow ups of liver lipids in response to therapeutic treatment. In this study, the characteristics of each subject are as expected in a study design of this type. The overweight group show statistically higher TG and lower levels of HDL, which are risk factors for cardiovascular diseases. This result was consistent with previous studies that examined a higher risk of cardiovascular disease and dyslipidemia occurring at BMI=21 kg/m².^{26, 27}

Furthermore, blood glucose and BMI were also significantly higher in the overweight group. This results further supports the idea that increasing BMI is associated with a higher risk of insulin resistance.²⁸ ¹H MRS spectra of liver were acquired and post processing by jMRUI and TARQUIN was performed. jMRUI is a widely accepted tool

used in various types of liver lipids studies, and is proven to be accurate for determining the levels of hepatic fat.^{19, 29} However, the jMRUI software package require user interaction for spectrum fitting, and may result in over fitting of liver lipids. On the other hand, TARQUIN is the automated spectrum fitting algorithm that does require a bit of user knowledge, but involves less user interaction than jMRUI. In this current study, lipids signal intensity from each group is shown in the liver spectrum and total liver lipids was calculated. The signal intensity from overweight group was higher than that of the control group, which is consistent with previous studies of higher liver lipids among the overweight and obese.^{30, 31} Signal intensity of each lipids group was not significantly different across the programs with the CV value also determined to be consistent; having a close relationship of signal intensity to that obtained from jMRUI and TARQUIN. The degree of change of liver lipids in the overweight group from both software package is similar, and was not significantly different. These finding suggests that both jMRUI and TARQUIN can assess liver lipids levels without noticeable differences occurring across the programs. Furthermore, both jMRUI and TARQUIN are able to give consistent results from different liver lipids levels in the overweight group. This finding, while preliminary, suggests that both jMRUI and TARQUIN are useful tools that can be

used interchangeably for liver lipids assessment. The automated nature of TARQUIN may ensure greater accessibility and ease of post processing of ^1H MRS spectrum without the influence or bias of user in liver lipid quantification.

Conclusion

This study reveals the correlation of liver lipids results from java-based graphical for MR user interface package (jMRUI) and totally automatic robust quantitation in NMR (TARQUIN) software packages. It can be asserted that both programs can be used for liver fat quantification study and can differentiate liver fat levels between groups of interest.

Conflicts of interest

The authors declare that they have no conflicts of interest.

References

- [1] Younossi Z, Anstee QM, Marietti M, Hardy T, Henry L, Eslam M, et al. Global burden of NAFLD and NASH: trends, predictions, risk factors and prevention. *Nature reviews Gastroenterology & hepatology*. 2018; 15(1): 11-20.
- [2] Anstee QM, Targher G, Day CP. Progression of NAFLD to diabetes mellitus, cardiovascular disease or cirrhosis. *Nature reviews Gastroenterology & hepatology*. 2013; 10(6): 330-44.
- [3] Fan J-G, Kim S-U, Wong VW-S. New trends on obesity and NAFLD in Asia. *Journal of Hepatology*. 2017; 67(4): 862-73.
- [4] Poovorawan K, Treeprasertsuk S, Thepsuthammarat K, Wilairatana P, Kitsahawong B, Phaosawasdi K. The burden of cirrhosis and impact of universal coverage public health care system in Thailand: Nationwide study. *Annals of hepatology*. 2015; 14(6): 862-8.
- [5] Cowin GJ, Jonsson JR, Bauer JD, Ash S, Ali A, Osland EJ, et al. Magnetic resonance imaging and spectroscopy for monitoring liver steatosis. *Journal of magnetic resonance imaging: JMRI*. 2008; 28(4): 937-45.
- [6] Idilman IS, Keskin O, Celik A, Savas B, Elhan AH, Idilman R, et al. A comparison of liver fat content as determined by magnetic resonance imaging-proton density fat fraction and MRS versus liver histology in non-alcoholic fatty liver disease. *Acta radiologica (Stockholm, Sweden)*. 2016; 57(3): 271-8.
- [7] Cassidy FH, Yokoo T, Aganovic L, Hanna RF, Bydder M, Middleton MS, et al. Fatty liver disease: MR imaging techniques for the detection and quantification of liver steatosis. *Radiographics: a review publication of the Radiological Society of North America, Inc*. 2009; 29(1): 231-60.
- [8] Lallukka S, Sädevirta S, Kallio MT, Luukkonen PK, Zhou Y, Hakkarainen A, et al. Predictors of Liver Fat and Stiffness in Non-Alcoholic Fatty Liver Disease (NAFLD) – an 11-Year Prospective Study. *Scientific Reports*. 2017; 7(1): 14561.
- [9] Traussnigg S, Kienbacher C, Gajdosik M, Valkovic L, Halilbasic E, Stift J, et al. Ultra-high-field magnetic resonance spectroscopy in non-alcoholic fatty liver disease: Novel mechanistic and diagnostic insights of energy metabolism in non-alcoholic steatohepatitis and advanced fibrosis. *Liver international : official journal of the International Association for the Study of the Liver*. 2017; 37(10): 1544-53.
- [10] Wilson M, Reynolds G, Kauppinen RA, Arvanitis TN, Peet AC. A constrained least-squares approach to the automated quantitation of in vivo (^1H) magnetic resonance spectroscopy data. *Magnetic resonance in medicine*. 2011; 65(1): 1-12.
- [11] Naressi A, Couturier C, Devos JM, Janssen M, Mangeat C, de Beer R, et al. Java-based graphical user interface for the MRUI quantitation package. *Magma (New York, NY)*. 2001; 12(2-3): 141-52.
- [12] Dcf Stefan D, Cesare F, Andrasescu A, Popa E, Lazariev A, Vescovo E, et al. Quantitation of magnetic resonance spectroscopy signals: The jMRUI software package 2009. p.104035.
- [13] Vanhamme L, van den Boogaart A, Van Huffel S. Improved method for accurate and efficient quantification of MRS data with use of prior knowledge. *Journal of magnetic resonance (San Diego, Calif)*. 1997; 129(1): 35-43.
- [14] Vilar-Gomez E, Martinez-Perez Y, Calzadilla-Bertot L, Torres-Gonzalez A, Gra-Oramas B, Gonzalez-Fabian L, et al. Weight Loss Through Lifestyle Modification Significantly Reduces Features of Nonalcoholic Steatohepatitis. *Gastroenterology*. 2015; 149(2): 367-78.e5; quiz e14-5.
- [15] Physical status: the use and interpretation of anthropometry. Report of a WHO Expert Committee. *World Health Organization technical report series*. 1995; 854: 1-452.
- [16] Martin SS, Blaha MJ, Elshazly MB, Toth PP, Kwiterovich PO, Blumenthal RS, et al. Comparison of a novel method vs the Friedewald equation for estimating low-density lipoprotein cholesterol levels from the standard lipid profile. *Jama*. 2013; 310(19): 2061-8.
- [17] Sathiyakumar V, Park J, Golozar A, Lazo M, Quispe R, Guallar E, et al. Fasting Versus Nonfasting and Low-Density Lipoprotein Cholesterol Accuracy. *Circulation*. 2018; 137(1): 10-9.
- [18] Pijnappel WWF, Boogaart A, de Beer R, van Ormondt D. Svd-Based Quantification of Magnetic-Resonance Signals 1992. p. 122-34.

- [19] Ouwerkerk R, Pettigrew RI, Gharib AM. Liver metabolite concentrations measured with ¹H MR spectroscopy. *Radiology*. 2012; 265(2): 565-75.
- [20] Vanhamme L, Fierro RD, Van Huffel S, de Beer R. Fast Removal of Residual Water in Proton Spectra. *Journal of magnetic resonance (San Diego, Calif: 1997)*. 1998; 132(2): 197-203.
- [21] Lallukka S, Sädevirta S, T. Kallio M, K. Luukkonen P, Zhou Y, Hakkarainen A, et al. Predictors of Liver Fat and Stiffness in Non-Alcoholic Fatty Liver Disease (NAFLD) – an 11-Year Prospective Study 2017.
- [22] Younossi ZM, Koenig AB, Abdelatif D, Fazel Y, Henry L, Wymer M. Global epidemiology of nonalcoholic fatty liver disease-Meta-analytic assessment of prevalence, incidence, and outcomes. *Hepatology (Baltimore, Md)*. 2016; 64(1): 73-84.
- [23] Haas JT, Francque S, Staels B. Pathophysiology and Mechanisms of Nonalcoholic Fatty Liver Disease. *Annu Rev Physiol*. 2016; 78: 181-205.
- [24] Szczepaniak LS, Nurenberg P, Leonard D, Browning JD, Reingold JS, Grundy S, et al. Magnetic resonance spectroscopy to measure hepatic triglyceride content: prevalence of hepatic steatosis in the general population. *American journal of physiology Endocrinology and metabolism*. 2005; 288(2): E462-8.
- [25] Ruhl CE, Everhart JE. Determinants of the association of overweight with elevated serum alanine aminotransferase activity in the United States. *Gastroenterology*. 2003; 124(1): 71-9.
- [26] Klop B, Elte JW, Cabezas MC. Dyslipidemia in obesity: mechanisms and potential targets. *Nutrients*. 2013; 5(4): 1218-40.
- [27] Kopelman P. Health risks associated with overweight and obesity. *Obesity reviews : an official journal of the International Association for the Study of Obesity*. 2007; 8 Suppl 1: 13-7.
- [28] Esteghamati A, Khalilzadeh O, Anvari M, Ahadi MS, Abbasi M, Rashidi A. Metabolic syndrome and insulin resistance significantly correlate with body mass index. *Archives of medical research*. 2008; 39(8): 803-8.
- [29] Meisamy S, Hines CD, Hamilton G, Sirlin CB, McKenzie CA, Yu H, et al. Quantification of hepatic steatosis with T1-independent, T2-corrected MR imaging with spectral modeling of fat: blinded comparison with MR spectroscopy. *Radiology*. 2011; 258(3): 767-75.
- [30] Huh JH, Kim KJ, Kim SU, Han SH, Han KH, Cha BS, et al. Obesity is more closely related with hepatic steatosis and fibrosis measured by transient elastography than metabolic health status. *Metabolism: clinical and experimental*. 2017; 66: 23-31.
- [31] Ezzat WM, Ragab S, Ismail NA, Elhosary YA, ElBaky AMNEA, Farouk H, et al. Frequency of non-alcoholic fatty liver disease in overweight/obese children and adults: Clinical, sonographic picture and biochemical assessment. *Journal of Genetic Engineering and Biotechnology*. 2012; 10(2): 221-7.

Quantification of hepatitis B virus (HBV) DNA and HBV genotyping simultaneously in plasma using real-time polymerase chain reaction

Woottichai Khamduang^{1,2,3*} Amonrat Pota¹ Wanvisa Khamlasai¹ Sayamon Hongjaisee^{1,4}
Nicole Ngo-Giang-Huong^{1,2} Wasna Sirirungsri^{1,3}

¹Department of Medical Technology, Faculty of Associated Medical Sciences, Chiang Mai University, Chiang Mai, Thailand

²Institut de Recherche pour le Développement (IRD) Unité Mixte Internationale 174-PHPT, Chiang Mai, Thailand

³Infectious Disease Research Unit (IDRU), Division of Clinical Microbiology, Department of Medical Technology, Faculty of Associated Medical Sciences, Chiang Mai University, Chiang Mai, Thailand

⁴Research Institute for Health Sciences, Chiang Mai University, Chiang Mai, Thailand

ARTICLE INFO

Article history:

Received 13 June 2018

Accepted as revised 15 August 2018

Available online 23 August 2018

Keywords:

Hepatitis B virus, quantification of HBV DNA, HBV genotyping, FRET real-time polymerase chain reaction,

ABSTRACT

Background: in Thailand, an estimated three million people are chronically infected with hepatitis B virus (HBV), mostly with genotypes C and B. Level of HBV replication as measured by quantification of HBV DNA in blood is crucial for management of chronic hepatitis B. However, HBV DNA measurement is not widely used due to limited availability and high cost of the test.

Objectives: To establish an assay for both HBV DNA load and HBV genotyping based on Fluorescence Resonance Energy Transfer (FRET) real-time polymerase chain reaction (PCR) technique and evaluate it using clinical samples.

Materials and methods: Published primers and FRET probes were used. Whole genome clones of HBV genotype B and C were used as reference. HBV DNA was extracted from clinical samples using a commercial platform (Abbott *m2000sp* system) and was then measured with the LightCycler® (Roche Diagnostics Applied Science). Results obtained with the in-house assay were compared to those obtained with COBAS® TaqMan® HBV Test, v2.0 (as a reference).

Results: We established an in-house assay with a sensitivity of 100 IU/mL of HBV DNA. Measurement of HBV DNA in 36 clinical samples showed a high correlation between HBV DNA load measured with in-house real-time PCR assay ($R=0.946$), compared to the reference assay. This assay identified HBV genotype B and genotype C based on the melting temperature peaks, 61-64 °C and 52-56 °C, respectively, and identified the presence of mixed HBV B and C genotypes if the minor population represents 10% or more of the whole population. HBV genotyping was possible in 22 of 28 samples with HBV DNA load above 2.00 log₁₀ IU/mL: 4 (18%) were genotype B and 18 (82%) were genotype C.

Conclusion: This in-house real-time PCR assay showed good performance for HBV DNA quantification in clinical samples and could distinguish B or C genotypes. It can represent an alternative to commercial assays for clinical use.

Introduction

Hepatitis B virus (HBV) infection is a major public

health problem worldwide, in particular in Asia where three-quarters of people with chronic hepatitis B infection live.¹ Individuals with chronic HBV infection are at high risk of developing severe complications such as liver fibrosis, cirrhosis and hepatocellular carcinoma. The main goal of therapy for patients with chronic HBV infection is to prevent disease progression and occurrence of complications. The

* Corresponding author.

Author's Address: Department of Medical Technology, Faculty of Associated Medical Sciences, Chiang Mai University, Chiang Mai, Thailand

** E-mail address: woottichai.k@cmu.ac.th

doi: 10.14456/jams.2018.21

E-ISSN: 2539-6056

level of HBV replication, assessed by quantification of HBV DNA in blood, is the strongest single predictive biomarker associated with disease progression and the long-term outcome of chronic HBV infection. Quantification of HBV DNA is thus crucial for appropriate management of patients with chronic HBV infection. The HBV DNA level varies during the different phase of HBV infection² and is used to define the phase of infection, make decision to start and assess the response to antiviral therapy.¹ In the 2015 World Health Organization (WHO) guidelines for the prevention, care, and treatment of persons living with chronic hepatitis B infection, quantification of HBV DNA is strongly recommended for initiation of treatment and monitoring of chronic infections.³ HBV genotype B and C are predominant in South East Asia, including in Thailand.⁴ Genotype C is associated with a high viral replication, experienced delayed HBeAg seroconversion, development of cirrhosis and hepatocellular carcinoma and non-response to interferon-based therapy.⁵⁻⁸

In Thailand, HBV infection is endemic. Currently, an estimated three million people are chronically infected predominantly with HBV genotype C or B.^{4,9} One criterion for treatment initiation in chronically HBV-infected patients recommended by the Thai Association for the Study of the Liver is a plasma HBV DNA above 2,000 IU/mL.¹⁰ In the context of elimination of viral hepatitis, it is expected that a large number of patients will need to be assessed for HBV replication level. However, HBV DNA assays currently available are commercial assays that are not affordable for many settings. We thus aimed to establish an assay which can measure HBV DNA load and HBV genotyping simultaneously based on Fluorescence Resonance Energy Transfer (FRET) real-time polymerase chain reaction (PCR) technique and evaluate it using clinical samples.

Materials and methods

Optimization of the real-time PCR assay

We used primers and FRET probes that were previous published.¹¹ The assay was based on probes hybridization. We focused on HBV genotype B and C the 2 predominant genotypes in Thailand.⁴ Reference strains of HBV genotype B and C were obtained after cloning whole genome of known HBV isolates.

To identify the optimal reaction conditions, we tested 6 different conditions with concentrations of primers and probes vary from 0.2 to 0.7 μ M. The final volume of PCR reaction was 20 μ L including 1X master mix, 2 mM MgCl₂ and 100 fg DNA template. PCR conditions were an initial denaturation step of 95 °C for 10 minutes, followed by 45 cycles of 95 °C for 5 seconds, 53 °C for 10 seconds, and 72 °C for 20 seconds. HBV DNA load was quantified by real-time detection of the emitted fluorescence at the annealing step of each PCR cycle (Roche LightCycler® 2.0 real time system).

To determine the limit of detection of the assay, 10-fold serial dilutions of HBV genotype B and C standard controls starting from 8 log₁₀ IU/mL were mixed in ratio 1:1 and tested as described above.

Evaluation of in-house assay using clinical samples

Clinical samples were obtained from the remaining EDTA plasma samples of HBV-infected individuals who received an HBV DNA load test using the COBAS® AmpliPrep/COBAS® TaqMan® HBV test v2.0 (Roche molecular diagnostics) at the Clinical Microbiology Laboratory Service Unit (CMSU), Associated Medical Sciences-Clinical Service Center (AMS-CSC). To ensure that the clinical samples tested in this study cover the range of all HBV DNA levels, we selected 4-5 plasma samples at each log₁₀ of HBV DNA level.

HBV DNA was extracted from patient's plasma using a commercial automatic DNA extractor (m2000sp Instrument, Abbott laboratories, USA) and the level of HBV DNA was then measured using the in-house real-time PCR on the Roche LightCycler® 2.0 real time system (Roche Diagnostics Applied Science). Results were compared to those obtained from COBAS® TaqMan® HBV Test version 2.0 as reference (Roche diagnostic GmbH, Mannheim, Germany).

HBV genotyping using the in-house real-time PCR assay

After the PCR was completed, HBV genotype B and C were identified by analyzing the melting curve and melting temperature of each genotype. To determine the ability of the assay to detect mix infection of genotype B and C, we analyzed the melting curve of various proportions of HBV standard genotype B and C with the final concentration at 5 log₁₀ IU/mL. HBV DNA quantification was performed using Roche LightCycler® 2.0 real time system and melting temperature peaks were identified in the melting curve.

To verify the genotypes identified by the melting temperature peaks, all samples with detectable HBV DNA were genotyped using a single tube semi-nested multiplex PCR technique which amplified products were visualized with gel electrophoresis.¹³ If the results between the 2 techniques were discrepant, sample's amplicons were then sequenced using primers targeting viral surface and polymerase genes, and the BigDye Terminator Mix V.1.1 (Applied Biosystems).¹² The sequences were aligned using the Bioedit software. HBV genotype was then identified by phylogenetic analysis using clustalW software.

Statistical analysis

Correlation analysis and Bland-Altman plot were generated to compare HBV DNA quantification using the two techniques. The Cohen's Kappa statistical test was used to compare the concordance of the two methods for HBV genotyping. All data analyses were performed using STATA™ version 10.1 software (Statacorp, College Station, TX).

Results

Development of real-time PCR assay for measuring of HBV DNA load and HBV genotyping

We tested 6 experimental conditions to identify the optimal concentrations of primers and probes. The condition corresponding to the concentration of 0.5 μ M for each primer and 0.2 μ M for each probe provided the best result with a high fluorescent signal (Cycle Threshold for

detection of HBV genotype B and C were 25.38 and 27.55, respectively) and lesser amount of reagents and was thus selected for the subsequent analyses. The sensitivity (limit

of detection) of this assay for HBV DNA detection was 100 IU/mL of HBV DNA (Table 1).

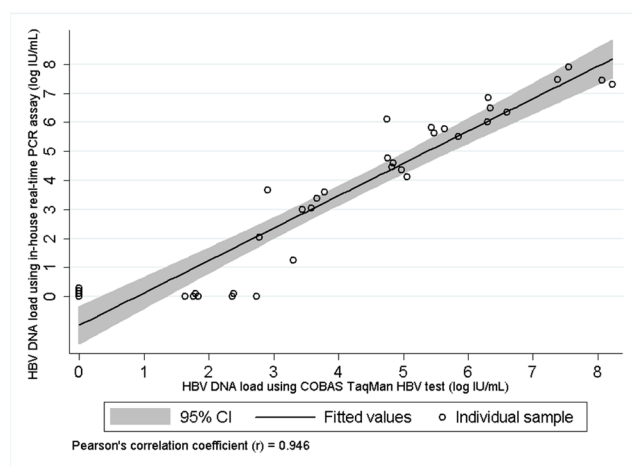
Table 1 Cycle threshold values derived from amplification plots of various concentrations of mixed standard HBV genotype B and C controls (ratio 1:1).

Concentration of standard HBV controls (IU/mL)	Cycle threshold of 1 st run	Cycle threshold of 2 nd run	Mean cycle threshold
100,000,000 (8 Log ₁₀)	15.63	15.78	15.71
10,000,000 (7 Log ₁₀)	20.83	20.93	20.88
1,000,000 (6 Log ₁₀)	24.70	24.25	24.48
100,000 (5 Log ₁₀)	27.72	27.65	27.69
10,000 (4 Log ₁₀)	31.15	31.98	31.57
1,000 (3 Log ₁₀)	36.02	35.63	35.83
100 (2 Log ₁₀)	38.23	38.45	38.34
10 (1 Log ₁₀)	Undetectable	Undetectable	Undetectable
1 (0 Log ₁₀)	Undetectable	Undetectable	Undetectable
0.1 (-1 Log ₁₀)	Undetectable	Undetectable	Undetectable
0.01 (-2 Log ₁₀)	Undetectable	Undetectable	Undetectable

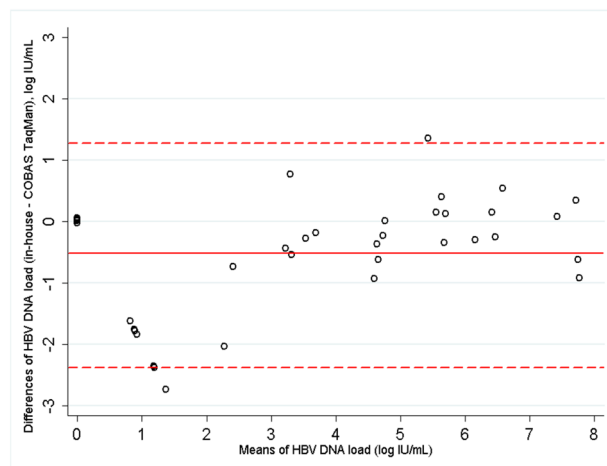
Evaluation of in-house assay for HBV quantification and genotyping

Thirty-six clinical samples were tested for HBV DNA quantification with both in-house real-time PCR assay and the COBAS® TaqMan® HBV Test v2.0 (reference assay). There was a high correlation between the two assays (Figure 1) and an excellent linear relationship (Pearson's correlation coefficient, $r=0.946$) (Figure 1A). Bland-Altman analysis showed the mean difference (in-house HBV DNA

assay – COBAS® TaqMan® HBV Test) was $-0.54 \log_{10}$ IU/mL with standard deviation (SD) of $0.95 \log_{10}$ IU/mL (Figure 1B). The in-house HBV DNA PCR assay could not quantify 7 samples with HBV DNA level ranged from 1.63 - $2.74 \log_{10}$ IU/mL measured by COBAS® TaqMan® HBV test. If only samples with HBV DNA above $3 \log_{10}$ IU/mL measuring by the reference method were considered for Bland-Altman analysis ($n=23$), the mean difference was improved to $-0.22 \log_{10}$ IU/mL with SD of $0.64 \log_{10}$ IU/mL.



(A)



(B)

Figure 1 Log₁₀-transformed HBV DNA level results of 36 samples with both Roche COBAS® TaqMan® HBV test and in-house real-time HBV DNA assays. (A) Correlation between plasma HBV DNA levels measured with the Roche assay and the in-house HBV real-time assay. The line indicates the best fit of the data to a linear regression. (B) Bland-Altman plot of HBV DNA obtained with two assays. Solid line represents the mean difference and the upper and lower dashed lines represent ± 1.96 standard deviation.

Detection of mixed genotype infection

Standard HBV genotype B showed a range of melting temperature peaks around 61-64 °C and standard genotype C showed a range around 52-56 °C (Figure 2). We assessed the melting temperature peaks of mixture of various ratio of standard genotype B and C. The results indicated mixed genotype infection could be detected with a sensitivity of 10%, i.e. viral population representing 10% or more of the whole population (Table 2).

Using the in-house assay, HBV genotype could be clearly identified in 22 of 28 samples tested (79%), 4 (18%)

were genotype B and 18 (82%) were genotype C. By a single tube semi-nested multiplex PCR technique, 15 of these 22 samples were successfully verified HBV genotype: 2 samples with genotype B and 13 samples with genotype C (Table 3). The concordance of the two methods for HBV genotyping was considered to be fair (Kappa=0.41, 95%CI: 0.13-0.68). Of the 6 samples with discrepant results between the 2 techniques, analysis of the HBV sequences showed that 2 samples were genotype B, 4 were C, which were corresponding to the results obtained from the technique based on real-time PCR.

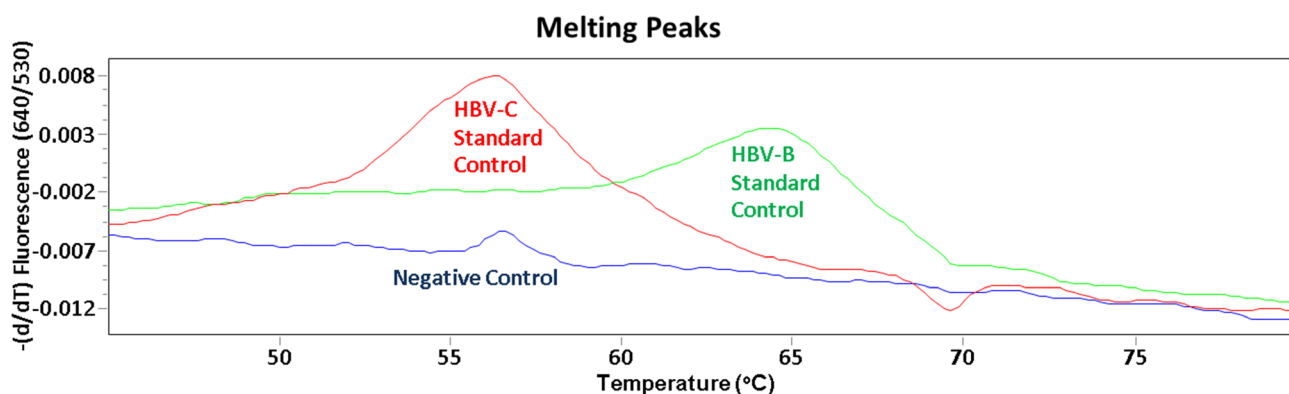


Figure 2 Melting peaks of HBV standard genotype B and C. Plotted as the derivative of fluorescence versus temperature.

Table 2 Melting temperature peaks according to HBV standard genotype B:C ratio.

Genotype B: Genotype C ratio	Melting temperature peak 1	Melting temperature peak 2
100:0	None	62.59
95:5	None	61.86
90:10	52.99	61.53
80:20	53.46	61.26
50:50	54.37	62.53
20:80	55.28	62.35
10:90	55.88	62.86
5:95	55.15	None
0:100	55.57	None
Control	None	None

Table 3 Comparison of HBV genotyping methods: in-house real-time PCR versus single tube semi-nested multiplex PCR.

Genotyping		in-house real-time PCR		
		B	C	Total
single tube semi-nested multiplex PCR	B	2	-	2
	C	-	13	13
	B and C	1	1	2
	Indeterminate	1	3	4
	Not done	-	1	1
	Total	4	18	22

Discussion

We established and evaluated a FRET PCR assay using clinical samples from HBV-infected patients in Thailand. This assay can be used to simultaneously quantify HBV DNA and also identify genotype B or C infecting the patient. This assay displayed a high sensitivity and very good correlation with the COBAS® TaqMan® assay. It was possible to detect a minor virus population representing 10% or more of the whole population.

We evaluated our assay against the COBAS® TaqMan® HBV Test v2.0. Comparison of HBV DNA results showed a high correlation of HBV DNA load between the 2 assays with an excellent linear relationship. However, the correlation was lower for HBV DNA level below 3 log₁₀ IU/mL. This is probably due to the low amount of DNA extract input (10 µL) used in this assay as compared to the input (50 µL) used in the reference assay. However, this 3 log₁₀ IU/mL threshold may not be relevant for clinical use since several guidelines, including the Thai guidelines, for HBV management do not recommend treatment for persons with normal ALT levels and low levels of HBV replication (<2,000 IU/mL).^{3,10}

Furthermore, our assay was able to accurately identify HBV genotypes as compared to the single tube semi-nested multiplex PCR technique in 71.4% (15 of 21). However, our assay could also identify HBV genotype in 6 samples that could not be clearly identified with the single tube semi-nested multiplex PCR technique. This discrepancy may be due to the high sensitivity of in-house assay based on real-time PCR while the single tube semi-nested multiplex PCR technique is a conventional technique and use gel electrophoresis for detection of PCR products. The whole process (viral isolation, quantification, and genotyping) of this assay takes about 4 hours and its cost is estimated to be 2-3 times cheaper than the commercial HBV DNA quantification assays.

However, this study has some limitations which include: 1) the lack of DNA internal control for extraction step, however the results of HBV DNA highly correlated between the 2 assays, and 2) the low number of clinical samples tested. Additional testing is probably needed to confirm and validate the performance of this assay.

In conclusion, we have established a real-time PCR assay for simultaneous quantification of HBV DNA and HBV genotyping in plasma that can be used in Thailand and in the Asia Pacific region where HBV genotype B and C are circulating. This assay may represent a cheaper alternative to current commercial assays for the quantification of HBV DNA and contribute to appropriate management of patients with chronic HBV infection.

Acknowledgements

This study was supported by the research supporting grant 2014 from the Faculty of Associated Medical Sciences, Chiang Mai University. We thank the Clinical Microbiology Laboratory Service Unit (CMSU) for sample collection, the Diagnostic Laboratory, Maharajnakorn Chiangmai Hospital, Faculty of Medicine, Chiang Mai University, and the IRD-UMI174/PHPT laboratory for providing useful help

and workplace. We thank Ms. Laddawan Laomanit and Ms. Phornphimon Moolnoi for sequencing and analyzing HBV genotype.

Conflict of interest:

The authors declare that they have no conflict of interest.

References

- [1] Sarin SK, Kumar M, Lau GK, Abbas Z, Chan HL, Chen CJ, et al. Asian-Pacific clinical practice guidelines on the management of hepatitis B: a 2015 update. *Hepatology* 2016; 10(1): 1-98. doi: 10.1007/s12072-015-9675-410.1007/s12072-015-9675-4.
- [2] Ganem D, Prince AM. Hepatitis B virus infection--natural history and clinical consequences. *N Engl J Med* 2004; 350(11): 1118-29.
- [3] World Health Organization (WHO). Guidelines for the prevention, care and treatment of persons with chronic hepatitis B infection. Geneva: World Health Organization; 2015.
- [4] Suwannakarn K, Tangkijvanich P, Thawornsuk N, Theamboonlers A, Tharmaphornpilas P, Yoocharoen P, et al. Molecular epidemiological study of hepatitis B virus in Thailand based on the analysis of pre-S and S genes. *Hepatology* 2008; 38(3): 244-51.
- [5] Tangkijvanich P, Mahachai V, Komolmit P, Fongsarun J, Theamboonlers A, Poovorawan Y. Clinical and virological differences between hepatitis B virus genotypes B and C: a case-control study. *J Med Assoc Thai* 2004; 87 Suppl 2: S223-7.
- [6] Duong TN, Horiike N, Michitaka K, Yan C, Mizokami M, Tanaka Y, et al. Comparison of genotypes C and D of the hepatitis B virus in Japan: a clinical and molecular biological study. *J Med Virol* 2004; 72(4): 551-7. doi: 10.1002/jmv.20044.
- [7] Kao JH, Chen PJ, Lai MY, Chen DS. Hepatitis B genotypes correlate with clinical outcomes in patients with chronic hepatitis B. *Gastroenterology* 2000; 118(3): 554-9.
- [8] Kao JH, Wu NH, Chen PJ, Lai MY, Chen DS. Hepatitis B genotypes and the response to interferon therapy. *J Hepatology* 2000; 33(6): 998-1002. doi: S0168-8278(00)80135-X.
- [9] Leroi C, Adam P, Khamduang W, Kawilapat S, Ngo-Giang-Huong N, Ongwandee S, et al. Prevalence of chronic hepatitis B virus infection in Thailand: a systematic review and meta-analysis. *Int J Infect Dis* 2016; 51: 36-43. doi: S1201-9712(16)31144-4 [pii]10.1016/j.ijid.2016.08.017.

- [10] Thai Association for the Study of the Liver. Thailand practice guideline for management of chronic hepatitis B and C. Bangkok: Thai Association for the Study of the Liver; 2015.
- [11] Yeh SH, Tsai CY, Kao JH, Liu CJ, Kuo TJ, Lin MW, et al. Quantification and genotyping of hepatitis B virus in a single reaction by real-time PCR and melting curve analysis. *J Hepatol* 2004; 41(4): 659-66. doi: S0168-8278(04)00300-9 [pii]10.1016/j.jhep.2004.06.031.
- [12] Khamduang W, Gaudy-Graffin C, Ngo-Giang-Huong N, Jourdain G, Moreau A, Borkird T, et al. Analysis of residual perinatal transmission of hepatitis B virus (HBV) and of genetic variants in human immunodeficiency virus and HBV co-infected women and their offspring. *J Clin Virol* 2013; 58(2): 415-21. doi: 10.1016/j.jcv.2013.06.025S1386-6532(13)00257-6.
- [13] Naito H, Hayashi S, Abe K. Rapid and specific genotyping system for hepatitis B virus corresponding to six major genotypes by PCR using type-specific primers. *J Clin Microbiol* 2001; 39(1): 362-4. doi: 10.1128/JCM.39.1.362-364.2001.

Antioxidant and anti-inflammatory activities of macerated herbal oil in dental pulp cells

Fahsai Kantawong^{1*} Sutinee Mungkala¹ Sawinee Tamang¹ Ruthairat Manaphan¹
Pichaporn Thaweean¹ Phenphichar Wanachantararak²

¹Department of Medical Technology, Faculty of Associated Medical Sciences, Chiang Mai University, Chiang Mai, Thailand

²The Dental Research Center, Faculty of Dentistry, Chiang Mai University, Chiang Mai, Thailand

ARTICLE INFO

Article history:

Received 31 May 2018

Accepted as revised 21 August 2018

Available online 29 August 2018

Keywords:

Macerated herbal oil, Dental Pulp Cells,
Anti-inflammation, Anti-Oxidant

ABSTRACT

Background: Sesame oil was used as an oil-pulling mouthwash to reduce the microorganisms that cause gum diseases. Herbs can be used in combination with sesame oil in oral health care. The previous study showed that macerated herbal oil decreased inflammation in human mesenchymal stem cells (HMSCs). It could be hypothesized that the addition of herbs should improve the efficiency in oil pulling.

Objectives: This study aimed to improve the efficiency of sesame oil for oral healthcare and to compare the total phenolic contents and antioxidant activities between sesame oil and macerated herbal oil. Moreover, this study compared the anti-inflammation activities between sesame oil and macerated herbal oil on lipopolysaccharide (LPS)-induced dental pulp cells (DPCs).

Materials and methods: The amount of total phenolic content was determined using Folin-Ciocalteu reagent. Antioxidant activity was investigated using DPPH assay and ferric-reducing power assay. MTT assay was used to determine cytotoxic effect and gene expression was studied using real-time PCR technique.

Results: The phenolic concentration in sesame and macerated herbal oils were not significantly different. However, antioxidant assays indicated that the antioxidant activity of macerated herbal oil was significantly higher than that of sesame oil. Both oils showed no cytotoxic effect on DPCs. Both oils also induced cell proliferation and increased expression of the thioredoxin (TXN) gene. Inflammation of DPCs were induced by LPS and treated with herbal oil or sesame oil to study cyclooxygenase-2 (COX-2) and interleukin-6 (IL-6) gene expression. The results of real-time PCR showed a decrease of COX-2 and IL-6 gene expression when LPS-induced DPCs were treated with macerated herbal oil compared to sesame oil.

Conclusion: Macerated herbal oil presented many benefits over sesame oil, including anti-oxidation and anti-inflammation activities. Therefore, adding herbs to sesame oil for oil pulling might protect against periodontal disease.

Introduction

Oil pulling has been used extensively as a traditional Indian folk remedy to prevent tooth decay, oral malodor, and bleeding gums.^{1, 2} Asian people have been gargling

vegetable oil as a mouthwash for thousands of years. It is believed that when the oil is moving in the mouth, it will pull out microorganisms from the teeth, gums and tongue. Oils commonly used in oil pulling include sesame, coconut and sunflower oils.

Peedikayil et al. found that coconut oil pulling could be an effective adjuvant procedure in decreasing plaque formation and plaque induced gingivitis.³ Sesame has been shown to help relieve infections by reducing *Streptococcus mutans* in plaque and saliva.² Some studies have demonstrated

* Corresponding author.

Author's Address: Department of Medical Technology, Faculty of Associated Medical Sciences, Chiang Mai University, Chiang Mai, Thailand

** E-mail address: fahsai.k@cmu.ac.th

doi: 10.14456/jams.2018.22

E-ISSN: 2539-6056

that the efficacies of sesame oil and chlorhexidine mouthwash were equivalent. For example, Asokan et al. reported that sesame oil pulling was as effective as chlorhexidine mouthwash against halitosis and microorganisms.⁴ Sood et al. demonstrated that sesame oil pulling was as effective as chlorhexidine in reducing oral malodor and the microbes that cause it.⁵ Sesame seeds mainly contain oleic and linoleic acid⁶; these substances act as anti-inflammatories by reducing IL-6 and COX-2 expression.⁷ COX-2 and IL-6 were considered as inflammatory enzymes and inflammatory cytokines, respectively.^{8,9} Given these properties, sesame oil can be used as an oil-pulling mouthwash to reduce the microorganisms that cause gum disease.

Herbs can be used in combination with sesame oil in oral health care.¹⁰⁻¹² Many of the herbs used in this research, including *Zingiber montanum*, *Zingiber zerumbet*, *Plantago major* Linn, *Amomum biflorum* Jack, and the peels and leaves of *Citrus hystrix*, have been shown to have medicinal properties.¹³⁻¹⁷ Previous study indicated that the rhizome of *Zingiber montanum* possessed antioxidant and anti-inflammatory activities.¹³ Recently, Verma et al. demonstrated the antimicrobial activities of *Zingiber montanum* essential oil against bacteria and fungi.¹⁸ *Zerumbone* from *Zingiber zerumbet* was reported to reduce the inflammatory response of acute lung injury via expression of ICAM-1, IL-1 β , and MIP-2.¹⁹ *Plantago major* extract protected renal tissue against doxorubicin-induced renal inflammation.²⁰ Hexane extract of the peels of *Citrus hystrix* fruits showed cytotoxicity against human pancreatic cancer cells.²¹

These herbs were simmered in hot sesame oil; a method similar to the maceration method that has been applied to vegetable oils and herbs since ancient times.²² Our previous study showed that macerated herbal oil decreased inflammation in human mesenchymal stem cells (HMSCs).²³ This study tried to modify the macerated herbal oil for dental care purpose and hypothesized that herbs, in addition to their various medicinal properties, could increase the oil-pulling efficiency of sesame oil. The aims of this study are to: 1) compare the total phenolic content and the antioxidant and anti-inflammatory activities of sesame oil against macerated herbal oil and 2) study the toxicity of sesame oil and macerated herbal oil on DPCs.

Materials and methods

Preparation of macerated herbal oil

The preparation of macerated herbal oil was modified from the previous study.²³ All the fresh herbs were washed and sliced. A volume of 750 ml of cold-pressed sesame oil (purchased from a local manufacturer) was heated with 250 g of crushed cockle shell on a charcoal stove for 10 min. 100 g of *Zingiber cassumunar*, 160 g of *Zingiber zerumbet*, 200 g of *Plantago major* Linn, 150 g of *Citrus hystrix* peels, 70 g of *Citrus hystrix* leaves, and 100 g of *Amomum biflorum* were added into the heated sesame oil. All the components were slowly stirred for 1.5 h. The oil was left overnight, then centrifuged at 2,000 rpm for 15 min. The herb residual was precipitated and the oil was separated into a new container. Clear yellow oil with the soft aroma

of the herbs was aliquoted in closed containers before storing at 4 °C until use. The previous recipe and the modified recipe were shown in Table 1.

Table 1 Previous recipe²³ and the modified recipe.

Components	Weight percent (wt%) Previous study	Weight percent (wt%) Present study
Sesame oil	47	40
Crushed cockle shells	10	14
<i>Zingiber cassumunar</i> Roxb.	13	6
<i>Zingiber zerumbet</i>	7	9
<i>Plantago major</i> Linn	2	12
Peels of <i>Citrus hystrix</i>	7	9
Leaves of <i>Citrus hystrix</i>	2	4
<i>Amomum biflorum</i>	3	6
Menthol	5	-
Camphor	2	-
Borneol	2	-
Total	100	100

Total phenolic content

The total phenolic content was performed as described in the previous study.²³ The sesame oil and macerated herbal oil were diluted with dimethyl sulfoxide (DMSO) to the dilutions of 1:2, 1:4, 1:8, 1:16, 1:32, 1:64, and 1:128. Thereafter, 50 μ l of each dilution was mixed with 2.5 ml Folin Ciocalteu reagent, and 2.0 ml Na₂CO₃ was added and mixed, before incubating at 45°C for 15 min. A blue color was observed, and the absorbance was measured at a wavelength of 764 nm. The mixture of 2.5 ml Folin Ciocalteu reagent and 2.0 ml Na₂CO₃ was used as blank for the zero setting. A standard calibration curve was prepared using different concentrations of gallic acid in DMSO. Three replicate assays were performed for each dilution, and the total phenolic concentrations were calculated from the standard curve and reported as mg/ml equivalent to standard gallic acid.

Antioxidant activity

The antioxidant activities were performed as described in the previous study²³.

(1) DPPH (1,1-diphenyl-2-picrylhydrazyl) radical scavenging Assay

The sesame oil and macerated herbal oil were diluted with DMSO to the dilutions of 1:2, 1:4, 1:8, 1:16, 1:32, 1:64, and 1:128. Then, 50 μ l of each dilution was mixed with 2,950 μ l of 2,2-diphenyl-1-picrylhydrazyl (DPPH) reagent. The mixture was allowed to react in the dark at room temperature for 15 min. The absorbance was measured at a wavelength of 515 nm using distilled water to set zero. Standard trolox was used as the positive control. DMSO solution of volume 2,950 μ l plus 50 μ l of each dilution was used as a sample blank. DPPH solution of volume 2,950 μ l plus 50 μ l DMSO was used as a control for calculation. Three replicate assays were performed for each dilution, and the %DPPH inhibition was calculated from the following

equation:

$$\% \text{ inhibition} = \frac{\text{Absorbance Blank} - \text{Absorbance Sample}}{\text{Absorbance Blank}} \times 100$$

(2) Ferric-reducing power activit

The ferric-reducing power activity was performed as described in the previous study.²³ The sesame oil and macerated herbal oil were diluted with DMSO to the dilutions of 1:2, 1:4, 1:8, 1:16, 1:32, 1:64, and 1:128. For reducing power, 2.5 μ l of each dilution of sesame oil or macerated herbal oil was mixed with 2.5 ml PBS. Then 2.5 ml of 1% potassium ferricyanide ($K_3Fe(CN)_6$) was added to the mixture and incubated at 50 °C for 20 min. After the reaction cooled down, 2.5 ml of 10% trichloroacetic acid was added and mixed. The reaction was centrifuged at 3,000 rpm for 10 min. A volume of 2.5 ml of the supernatant was separated and mixed with 2.5 ml of deionized water. A volume of 0.5 ml of 0.1% ferric chloride was added to the reaction and allowed to stand for 10 min. The absorbance was measured at 700 nm. Three replicate assays were performed for the statistical analysis. Various concentrations of butylated hydroxytoluene (BHT) in DMSO were used to generate a standard curve. The reducing power was calculated from the standard curve and reported as reducing power equivalent to BHT.

DPCs isolation

Ethical approval by the Ethics Committee of the Faculty of Dentistry, Chiang Mai University (40/2559) was obtained for this study. DPCs were prepared as described previously by Fahsai et al.²⁴ Briefly, the gum tissue was removed with a scalpel blade No. 15, and the teeth were wiped with povidone-iodine for 2 min, then wiped with 70% ethanol for 2 min to remove bacteria. The teeth were notched at a dentogingival junction with a chisel before immersion in 15 ml plastic tubes containing complete Dulbecco Modified Eagle Medium (complete DMEM). The teeth were then washed twice with phosphate buffer saline (PBS) and once with complete DMEM. The teeth were separated into two parts at a dentogingival junction and a sterile endodontic spoon was used to scoop pulp tissue that was then placed onto a glass dish. The tissue was sliced into small pieces with a sterile blade and cultured in complete DMEM at 37 °C and 5% CO₂. Medium was changed every other day. The DPCs grew out of a piece of tissue until 1-2 weeks. Cells were digested and grown in tissue culture flasks. Cells (passage 4) were seeded into a 24-well plate at a density of 2.5×10^4 cells/well. Cells were allowed to adhere for 24 h in complete Dulbecco's Modified Eagle Medium/F12 (DMEM/F12) at 37 °C and 5% CO₂.

MTT assay

Cell viability was determined using the MTT assay. Briefly, the sesame oil or macerated herbal oil was diluted in DMSO to the dilutions of 1:4, 1:8, 1:16, 1:32, 1:64 and 1:128. Then 100 μ l of each dilution was added to 10 ml of complete media. Thus, the final concentrations of the oil in 1 ml media were 2.5, 1.25, 0.625, 0.3125, and 0.156 μ l

of oil/ml of media. The entire media was discarded and replaced with sesame oil or macerated herbal oil supplemented media. The cell culture was maintained at a temperature of 37 °C in a 5% CO₂ incubator for 48 h. The macerated herbal oil supplemented media was discarded and replaced with 0.5 ml of MTT reagent (0.5 mg in 1 ml media). The reaction was maintained at 37°C and 5% CO₂ for 3 h. The MTT supplemented media was discarded and 1 ml of DMSO was added. The absorbance of the formazan product was measured at 540 nm and the background was corrected at 630 nm. The percentage of the cell viability was compared to that of control, which was cultured in media plus DMSO (100 μ l DMSO in 10 ml media). Three replicate assays were performed for the statistical analysis.

TXN gene expression

The expression of TXN gene was previously described in our study.²³ DPCs (passage 4) were seeded into 6-well plates at a density of 5×10^4 cells/well. Sesame oil and macerated herbal oil was diluted in DMEM / F12 at a concentration of 0.2 μ l of oil / ml of media (for control group, 0.2 μ l of DMSO was diluted in DMEM / F12). Media was added to the seeded cells and then incubated at 37 °C with 5% CO₂ for 21 days. Media was changed twice a week. Cells were trypsinized and washed with PBS; cell pellets were used for further RNA extraction. RNA extraction was performed using High Pure Isolation Kit as suggested by the manufacturer. Total RNA was transcribed into cDNA by the following steps: 16 μ l of total RNA was mixed with 4 μ l of 5x iScript RT supermix. The reaction took place in an Eppendorf Mastercycler using the following protocol: 1) cDNA priming at 37 °C for 15 min, 2) transcription at 50 °C for 5 min and 3) inactivation at 98 °C for 5 min. NO-RT reaction was prepared as a negative control. DNA elimination was performed using rDNase (Macherey-Nagel). 1 μ l of rDNase was added to 10 μ l of total RNA following by incubation at 37 °C for 15 min. RT-PCR was performed using SYBR Green Mastermix (SensiFAST SYBR® No-ROX Kit-Bioline). Briefly, cDNA was diluted 1:10 and the 10- μ l reaction was composed of 5 μ l of SYBR Green RT-PCR master mix, 1 μ L of cDNA template, 3.5 μ l of distilled water, and 0.25 μ M of target-specific primer. RT-PCR was performed in LightCycler480 (Roche) and the polymerase chain reaction protocol consisted of 95 °C pre-incubation for 2 min, followed by 40 cycles of 95 °C for 5 sec, 60 °C for 10 sec, and 72 °C for 10 sec. The melting peak analysis was performed at 95 °C for 5 sec, 65 °C for 1 min, and 97 °C continuous. The cooling step was performed at 40 °C for 30 sec. GAPDH was used as a reference gene. The relative quantification was performed using LightCycler® 480 software 1.5. The list of primers is shown in Table 2.

Table 2 Human target genes & reference gene for Relative Quantitative RT-PCR.

Target genes	Primer sequences (5'->3')
Cyclooxygenase-2 (COX-2)	F: CCCTTGGGTGTCAAAGGTAA
	R: GCCCTCGCTTATGATCTGTC
Interleukin-6 (IL-6)	F: GGTACATCCTCGACGGCATCT
	R: GCCTCTTTGCTGCTTTTAC
Thioredoxin (TXN1)	F: ACGCTGCAGGTGATAAAC
	R: CTGACAGTCATCCACATCTAC
Glyceraldehyde-3-phosphate dehydrogenase (GAPDH)	F: AAGGGCTCATGACCACAGTC
	R: GGATGACCTTGCCACAG

Anti-inflammation assay

DPCs (passage 4) were seeded into 6-well plates at a density of 1×10^5 cells/well and incubated at 37 °C and 5% CO₂ for 48 h. Treatment was performed as follows: cells cultured in DMEM/F12 and vehicle (C), cells cultured in DMEM/F12 with sesame oil 0.2 µl/1 ml of media (S), cells

cultured in DMEM/F12 with macerated herbal oil 0.2 µl/ 1 ml of media (H), cells cultured in LPS 4 µg / ml in DMEM F12 (L), cells cultured in sesame oil 0.2 µl/1 ml and LPS 4 µg/ml in DMEM/F12 (L+S) and cells cultured in macerated herbal oil 0.2 µl/1 ml and LPS 4 µg/ml in DMEM/F12 (L+H). After 48 h, cells were washed and trypsinized. RNA extraction, reverse transcription and real-time PCR were performed as mentioned in the protocol

Results**Total phenolic content**

The phenolic content of sesame oil dilutions of 1:2, 1:4, 1:8, 1:16, 1:32, 1:64, and 1:128 were equivalent to standard gallic acid concentrations of 2.50, 0.39, 0.59, 0.21, 0.09, 0.05, 0.02 mg / ml, respectively (Figure. 1A). The phenolic content of macerated herbal oil dilutions of 1:2, 1:4, 1:8, 1:16, 1:32, 1:64, and 1:128 were equivalent to standard gallic acid concentrations of 2.17, 0.86, 0.49, 0.27, 0.11, 0.05, 0.02 mg/ml, respectively (Figure. 1B). The total phenolic content of the sesame and macerated herbal oils did not differ significantly (Figure. 1C).

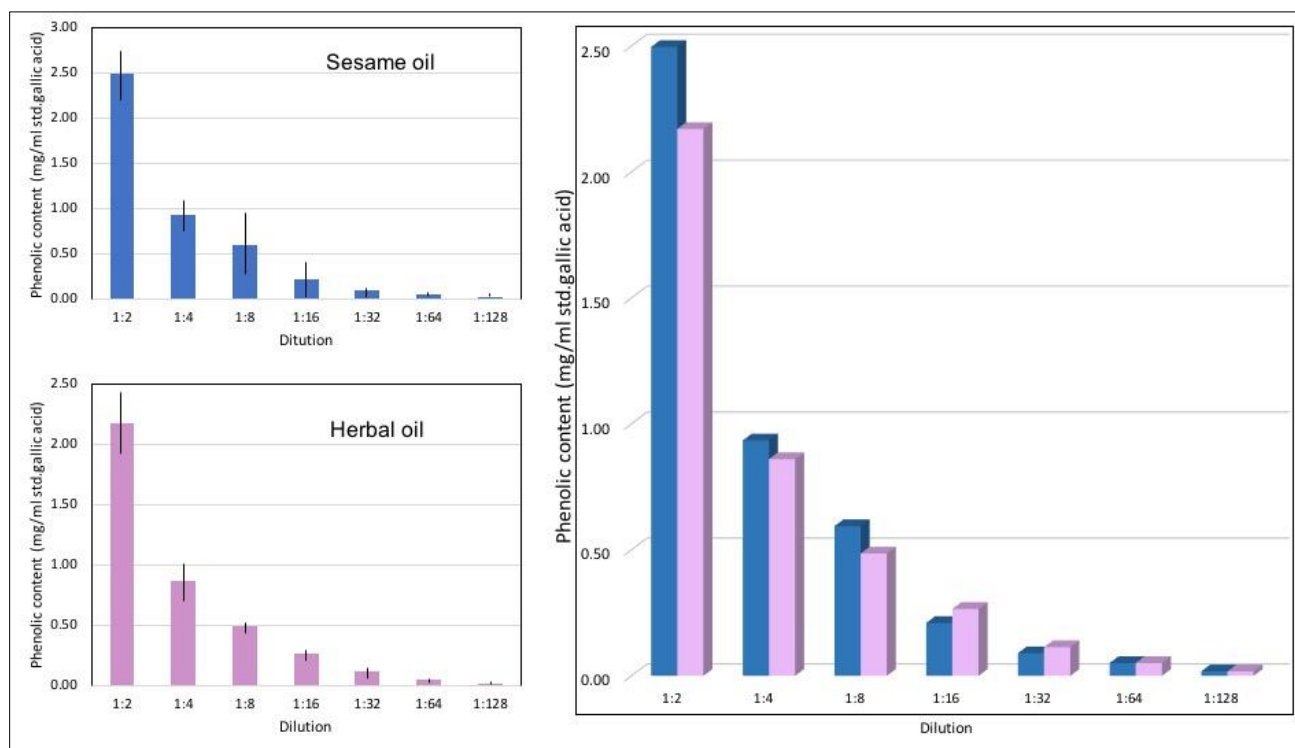


Figure 1 Total phenolic content: This figure shows the total phenolic content of sesame oil in comparison with macerated herbal oil using gallic acid as a standard. The phenolic content of the two oils does not differ significantly.

Antioxidant activity

(1) DPPH assay

From the DPPH assay, the % inhibitions of sesame oil dilutions of 1:2, 1:4, 1:8, 1:16, 1:32, 1:64, and 1:128 were 27.53, 13.84, 3.88, 2.30, 1.00, 1.00, and 0.62, respectively (Figure. 2A). The % inhibitions of macerated herbal oil dilutions of 1:2, 1:4, 1:8, 1:16, 1:32, 1:64, and 1:128 were 49.87, 24.13, 10.82, 5.93, 3.97, 2.29, and 2.17, respectively (Figure. 2B). The antioxidant activity of the macerated herbal oil dilutions was significantly higher than the sesame oil (Figure. 2C).

(2) Ferric reducing power activity

This analysis determined the oils' ability to reduce Fe^{3+} to Fe^{2+} . Sesame oil dilutions of 1:2, 1:4, 1:8, 1:16, and 1:32 had reducing activity equivalent to standard BHT concentrations of 0.42, 0.29, 0.12, 0.10, 0.08 $\mu\text{g/ml}$, respectively (Figure. 2D). Macerated herbal oil dilutions of 1:2, 1:4, 1:8, 1:16, and 1:32 had reducing activity equivalent to standard BHT concentrations of 0.47, 0.36, 0.26, 0.19, 0.14 $\mu\text{g/ml}$, respectively (Figure. 2E). The reducing power of macerated herbal oil was statistically higher than sesame oil (Figure. 2F).

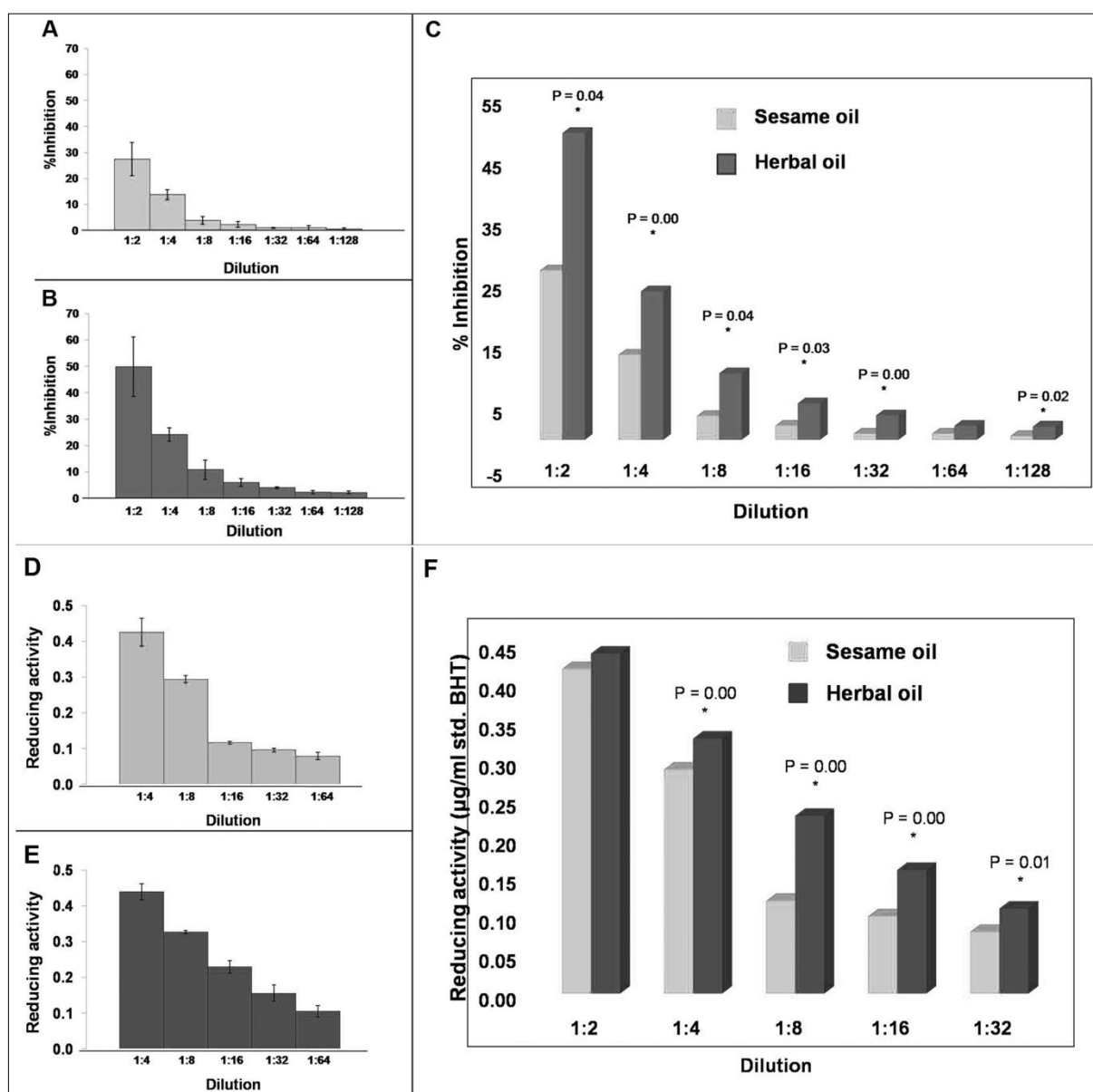


Figure 2 (2A, 2B and 2C) DPPH assay: Macerated herbal oil is significantly more efficient at scavenging DPPH radicals than sesame oil. (2D, 2E and 2F) Ferric reducing power activity: The macerated herbal oil is more capable of reducing Fe^{3+} to Fe^{2+} than sesame oil, with BHT as the standard.

MTT assay

The MTT assay demonstrated that the sesame and macerated herbal oils were not toxic to DPCs; both oils resulted in significant cell proliferation (Figure. 3A & 3B). The % cell viability did not differ significantly between

sesame oil and macerated herbal oil (Figure. 3C) except at the concentration 12.5 μ l of oil/ml of media, sesame oil induced more pronounced cell proliferation than herbal oil.

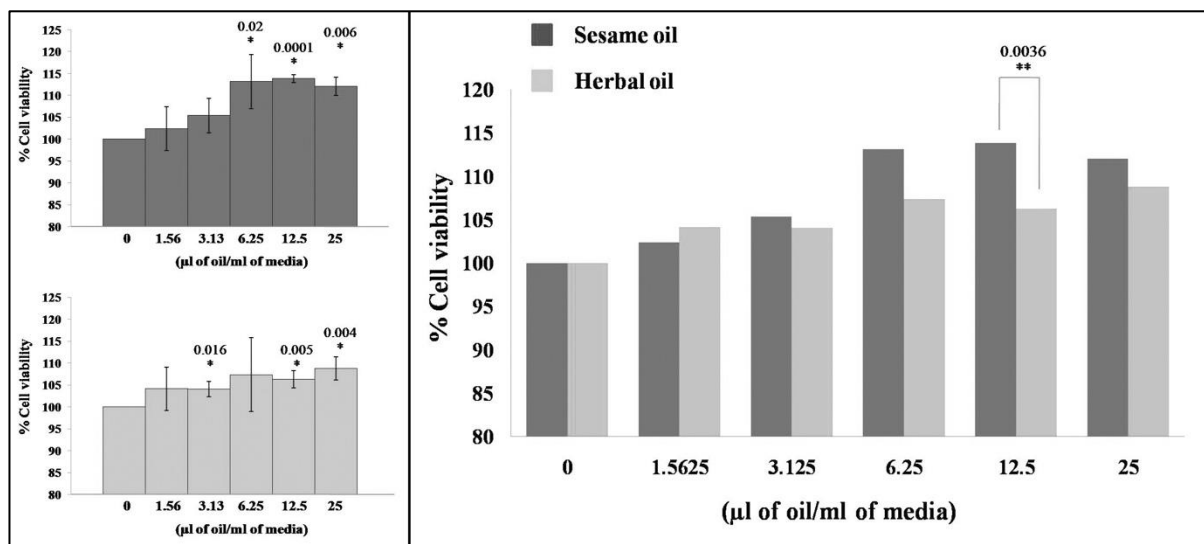


Figure 3 MTT assay: The graphs show the relationship between the concentration of sesame oil & macerated herbal oil versus % viability of DPCs (Figure. 3A & 3B). Sesame oil and macerated herbal oil are not toxic to DPCs and both of them display cell proliferation activity (Figure. 3C).

Antioxidant gene expression

Figure. 4A compared the TXN gene expression of the control group versus DPCs treated with sesame oil and

macerated herbal oil. The expression of TXN gene increased significantly in DPCs cultured in the presence of macerated herbal oils and sesame oil.

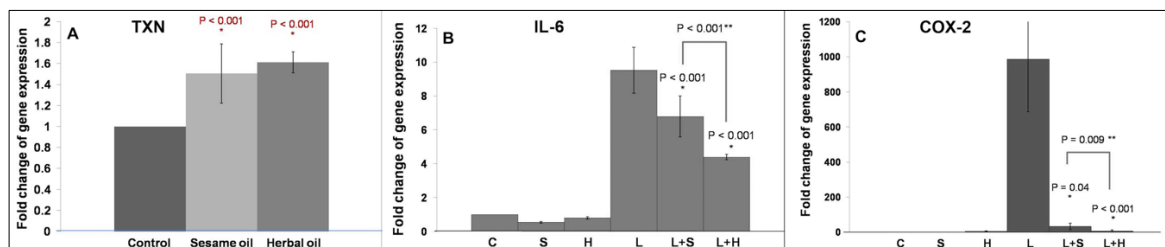


Figure 4 (4A) TXN gene expression: Sesame oil and macerated herbal oil increase TXN gene expression. (4B and 4C) Anti-inflammation assay: Both sesame oil and macerated herbal oil reduce COX-2 and IL-6 gene expression. C = cells cultured in DMEM/F12 with vehicle (DMSO). S = cells cultured in DMEM/F12 with sesame oil (0.2 μ l/ml). H = cells cultured in DMEM/F12 with macerated herbal oil (0.2 μ l/ml). L = cells cultured in DMEM/F12 with LPS (4 μ g/ml). L+S = cells cultured in DMEM/F12 with sesame oil (0.2 μ l/ml) and LPS (4 μ g/ml). L+H = cells cultured in DMEM/F12 with macerated herbal oil (0.2 μ l/ml) and LPS (4 μ g/ml). * = significant at $p < 0.05$.

Anti-inflammatory activity

Sesame oil and macerated herbal oil reduced gene expression of COX-2 and IL-6 in DPCs that had induced inflammation from LPS (4 μ g/ml) compared to the positive control treated with LPS alone (Figure. 4B & 4C). Oil pulling with sesame oil has been shown to significantly reduce plaque-induced gingivitis.²⁵ This study proved that sesame oil inhibited the expression of COX-2 and IL-6, which might be the mechanism of its anti-inflammatory effect. Sesame oil showed anti-inflammatory effects on DPCs, without cytotoxicity. Moreover, COX-2 and IL-6 decreased significantly, when macerated herbal oil was supplemented to LPS-treated cells.

Discussion

Herbal medicine can be applied to improve the efficacy of sesame oil. Adding herbs to hot sesame oil by a method called hot oil maceration produces macerated herbal oil. This study found that sesame oil contains phenolic compounds, and adding herbs does not significantly affect the total phenolic content. However, a previous report indicated that the efficiency of maceration for extracting phenolic compounds is low.²⁶ Sesame and macerated herbal oils exhibited antioxidant activity through scavenging of DPPH radicals; they also showed ferric-reducing properties. The macerated herbal oil's ability to scavenge DPPH radicals and its reducing properties are statistically higher than the sesame oil.

The total phenolic contents of sesame oil and macerated herbal oil were not different. However, antioxidant and anti-inflammatory activities of macerated herbal oil were superior which indicated that the potential antioxidant and anti-inflammatory activities in macerated herbal oil might come from the combination of phenolic compounds in sesame oil and other non-phenolic compounds from the added herbs.

It appears that sesame oil induced dental pulp cell proliferation. These results support that sesame oil has potential for oil pulling; adding herbs may provide even more benefits. Our previous study showed that macerated herbal oil reduced inflammation in HMSCs.²³ In the present, study the proportion of each component was modified. The previous study was found that macerated herbal oil has toxicity at the concentration ≥ 2.5 $\mu\text{l/ml}$ in complete DMEM.²³ Thus, menthol, camphor, and borneol were excluded from this study and the toxicity was not present anymore (Figure. 3). The macerated herbal oil slightly induced cell proliferation. Moreover, this study demonstrated that treatment with sesame or macerated herbal oils significantly induced the antioxidant gene (Figure. 4A). This result correlated well with previous studies by Yeh et al. that demonstrated that phenolic acid induced antioxidant enzyme expression.^{27, 28}

This study demonstrated that macerated herbal oil is a better antioxidant and anti-inflammatory than sesame oil. The anti-microorganism assay was performed with *Streptococcus mutans* and *Candida albican* (data not shown); neither sesame oil nor macerated herbal oil demonstrated anti-microorganism activity (data not shown). The sesame oil and macerated herbal oil did not inhibit *Streptococcus mutans* and *Candida albican* (data not shown). This result is supported by Asokan et al., who found that sesamin and sesamol isolated from sesame oil showed no antibacterial effect against oral microorganisms, such as *Streptococcus mutans*, *Streptococcus mitis* and *Streptococcus viridians*.²⁹ This result also correlated with Jauhari et al., who found that oil pulling does not provide any additional benefit as an antimicrobial agent in reducing the bacterial colonization of an individual.³⁰ However, it is possible that the saponification and emulsification process, which enhances its mechanical cleaning action, should be considered as an underlying mechanism.²⁹ Given this mechanism, together with the anti-inflammatory effect, sesame oil can be used in oil pulling, with the addition of herbs increasing its efficacy.

In conclusion, the macerated herbal oil showed no statistical difference in total phenolic content compared to sesame oil. The macerated herbal oil did, however, display superior antioxidant activity compared to sesame oil. Neither sesame oil nor macerated herbal oils were cytotoxic to DPCs, and both induced cell proliferation and increased TXN gene expression in DPCs. The presence of macerated herbal oil and sesame oil attenuated the LPS-induced expression of COX-2 and IL-6 genes. Macerated herbal oil reduced expression of COX-2 and IL-6 better than sesame oil. Adding herbs to produce macerated herbal oil improved the efficiency of sesame oil, offering potential as an alternative oral health care product.

Conflict of interest:

The authors have no conflicting interests.

Acknowledgements

This work was supported by the Faculty of Associated Medical Sciences, Chiang Mai University, Thailand.

References

- [1] Asokan S. Oil pulling therapy. Indian J Dent Res. 2008;19(2): 169. doi: 10.4103/0970-9290.40476.
- [2] Asokan S, Rathan J, Muthu MS, Rathna PV, Emmadi P, Raghuraman, et al. Effect of oil pulling on Streptococcus mutans count in plaque and saliva using Dentocult SM Strip mutans test: a randomized, controlled, triple-blind study. J Indian Soc Pedod Prev Dent. 2008;26(1): 12-7. doi: 10.4103/0970-4388.40315.
- [3] Peedikayil FC, Sreenivasan P, Narayanan A. Effect of coconut oil in plaque related gingivitis - A preliminary report. Niger Med J. 2015;56(2): 143-7. doi: 10.4103/0300-1652.153406.
- [4] Asokan S, Kumar RS, Emmadi P, Raghuraman R, Sivakumar N. Effect of oil pulling on halitosis and microorganisms causing halitosis: a randomized controlled pilot trial. J Indian Soc Pedod Prev Dent. 2011;29(2): 90-4. doi: 10.4103/0970-4388.84678.
- [5] Sood P, Devi M A, Narang R, V S, Makkar DK. Comparative efficacy of oil pulling and chlorhexidine on oral malodor: a randomized controlled trial. J Clin Diagn Res. 2014;8(11): ZC18-21. doi: 10.7860/JCDR/2014/9393.5112.
- [6] Makinde FM, Akinoso R. Comparison between the nutritional quality of flour obtained from raw, roasted and fermented sesame (*Sesamum indicum* L.) seed grown in Nigeria. Acta Sci Pol Technol Aliment. 2014;13(3): 309-19.
- [7] Fostok SF, Ezzeddine RA, Homaidan FR, Al-Saghir JA, Salloum RG, Saliba NA, et al. Interleukin-6 and Cyclooxygenase-2 downregulation by fatty-acid fractions of *Ranunculus constantinopolitanus*. BMC Complement Altern Med. 2009;9: 44. doi: 10.1186/1472-6882-9-44.
- [8] Xing Z, Gaudie J, Cox G, Baumann H, Jordana M, Lei XF, et al. IL-6 is an antiinflammatory cytokine required for controlling local or systemic acute inflammatory responses. J Clin Invest. 1998;101(2): 311-20.
- [9] Scheller J, Chalaris A, Schmidt-Arras D, Rose-John S. The pro- and anti-inflammatory properties of the cytokine interleukin-6. Biochim Biophys Acta. 2011;1813(5): 878-88. doi: 10.1016/j.bbam-cr.2011.01.034.
- [10] Sastravaha G, Yotnuengnit P, Booncong P, Sangtherapitkul P. Adjunctive periodontal treatment with *Centella asiatica* and *Punica granatum* extracts. A preliminary study. J Int Acad Periodontol. 2003;5(4): 106-15.

- [11] Kadam A, Prasad BS, Bagadia D, Hiremath VR. Effect of Ayurvedic herbs on control of plaque and gingivitis: A randomized controlled trial. *Ayu*. 2011;32(4): 532-5. doi: 10.4103/0974-8520.96128.
- [12] Kumar G, Jalaluddin M, Rout P, Mohanty R, Dileep CL. Emerging trends of herbal care in dentistry. *J Clin Diagn Res*. 2013;7(8): 1827-9. doi: 10.7860/JCDR/2013/6339.3282.
- [13] Bua-in S, Paisooksantivatana Y. Essential Oil and Antioxidant Activity of Cassumunar Ginger (Zingiberaceae: Zingiber montanum (Koenig) Link ex Dietr.) Collected from Various Parts of Thailand. *Kasetsart J (Nat Sci)*. 2009;43: 467 - 75.
- [14] Zakaria ZA, Mohamad AS, Ahmad MS, Mokhtar AF, Israif DA, Lajis NH, et al. Preliminary analysis of the anti-inflammatory activity of essential oils of Zingiber zerumbet. *Biol Res Nurs*. 2011;13(4): 425-32. doi: 10.1177/1099800410386590.
- [15] Stenholm A, Göransson U, Bohlin L. Bioassay-guided supercritical fluid extraction of cyclooxygenase-2 inhibiting substances in *Plantago major* L. *Phytochem Anal*. 2013;24(2): 176-83. doi: 10.1002/pca.2398.
- [16] Abirami A, Gunasekaran Siddhuraju, Perumal. In vitro antioxidant, anti-diabetic, cholinesterase and tyrosinase inhibitory potential of fresh juice from *Citrus hystrix* and *C. maxima* fruits. *Food Science and Human Wellness*. 2014;3(1): 16-25. doi: 10.1016/j.fshw.2014.02.001.
- [17] Singtothong C, Gagnon MJ, Legault J. Chemical composition and biological activity of the essential oil of *Amomum biflorum*. *Nat Prod Commun*. 2013;8(2): 265-7.
- [18] Verma RS, Joshi N, Padalia RC, Singh VR, Goswami P, Verma SK, et al. Chemical composition and antibacterial, antifungal, allelopathic and acetylcholinesterase inhibitory activities of cassumunar-ginger. *Journal of the Science of Food and Agriculture*. 2018;98(1): 321-7. doi: 10.1002/jsfa.8474.
- [19] Lee CY, Chen SP, Su CH, Ho YC, Yang ML, Lee SS, et al. Zerumbone from Zingiber zerumbet Ameliorates Lipopolysaccharide-Induced ICAM-1 and Cytokines Expression via p38 MAPK/JNK-IkB/NF-κB Pathway in Mouse Model of Acute Lung Injury. *Chin J Physiol*. 2018;61(3): 171-80. doi: 10.4077/CJP.2018.BAG562.
- [20] Entezari Heravi N, Hosseinian S, Naji Ebrahimi Yazd Z, Shafei MN, Ebrahimzadeh Bideskan A, Shahraki S, et al. Doxorubicin-induced renal inflammation in rats: Protective role of *Avicenna* J *Phytomed*. 2018;8(2): 179-87.
- [21] Sun S, Phrutivorapongkul A, Dibwe DF, Balachandran C, Awale S. Chemical Constituents of Thai Citrus *hystrix* and Their Antiausterity Activity against the PANC-1 Human Pancreatic Cancer Cell Line. *J Nat Prod*. 2018. doi: 10.1021/acs.jnatprod.8b00405.
- [22] Ayadi MA, Grati-Kamoun N, Attia H. Physico-chemical change and heat stability of extra virgin olive oils flavoured by selected Tunisian aromatic plants. *Food Chem Toxicol*. 2009;47(10): 2613-9. doi: 10.1016/j.fct.2009.07.024.
- [23] Kantawong F, Singhatong S, Srilamay A, Boonyuen K, Mooti N, Wanachantararak P, et al. Properties of macerated herbal oil. *Bioimpacts*. 2017;7(1): 13-23. doi: 10.15171/bi.2017.03.
- [24] Kantawong F, Thaweean P, Mungkala S, Tamang S, Manaphan R, Wanachantararak P, et al. Mucus of *Achatina fulica* stimulates mineralization and inflammatory response in dental pulp cells. *Turk J Biol*. 2016;40(2): 353-9. doi:10.3906/biy-1505-29.
- [25] Asokan S, Emmadi P, Chamundeswari R. Effect of oil pulling on plaque induced gingivitis: a randomized, controlled, triple-blind study. *Indian J Dent Res*. 2009;20(1): 47-51.
- [26] Khoddami A, Wilkes MA, Roberts TH. Techniques for analysis of plant phenolic compounds. *Molecules*. 2013;18(2): 2328-75. doi: 10.3390/molecules18022328.
- [27] Yeh CT, Yen GC. Induction of hepatic antioxidant enzymes by phenolic acids in rats is accompanied by increased levels of multidrug resistance-associated protein 3 mRNA expression. *J Nutr*. 2006;136(1): 11-5.
- [28] Yeh CT, Ching LC, Yen GC. Inducing gene expression of cardiac antioxidant enzymes by dietary phenolic acids in rats. *J Nutr Biochem*. 2009;20(3): 163-71. doi: 10.1016/j.jnutbio.2008.01.005.
- [29] Asokan S, Rathinasamy TK, Inbamani N, Menon T, Kumar SS, Emmadi P, et al. Mechanism of oil-pulling therapy - in vitro study. *Indian J Dent Res*. 2011;22(1): 34-7. doi: 10.4103/0970-9290.79971.
- [30] Jauhari D, Srivastava N, Rana V, Chandna P. Comparative Evaluation of the Effects of Fluoride Mouthrinse, Herbal Mouthrinse and Oil Pulling on the Caries Activity and Streptococcus mutans Count using Oratest and Dentocult SM Strip Mutans Kit. *Int J Clin Pediatr Dent*. 2015;8(2): 114-8. doi: 10.5005/jp-journals-10005-1295.

Bacterial contamination and their tolerance in banknotes and coins surrounding the area of Chiang Mai University Hospital in Chiang Mai Province

Ponrut Phunpae^{1,3*} Chanjuti Sriruan¹ Ratchadaporn Udpaun¹ Santhana Buamongkol¹ Sudjai Pawichai¹
Autchar Ruangpayuk² Watchawan Chairuangwut¹

¹Division of Clinical Microbiology, Department of Medical Technology, Faculty of Associated Medical Sciences, Chiang Mai University, Thailand

²Department of Medical Technology, Amphawa Hospital, Samut Songkhram, Thailand

³Infectious Diseases Research Unit (IDRU), Faculty of Associated Medical Sciences, Chiang Mai University, Thailand

ARTICLE INFO

Article history:

Received 23 July 2018

Accepted as revised 27 August 2018

Available online 31 August 2018

Keywords:

Thai banknotes, Thai coins, bacteria contamination, bacterial tolerance

ABSTRACT

Background: Currency including banknotes and coins are used in everyday life by everyone. It is, therefore, a universal medium for carrying potentially pathogenic bacteria which can spread and cause infection in the population. Thus, it is of interest to study the bacterial contamination in currency used daily in Chiang Mai province, of which there is scant information.

Objectives: To study the quantity and types of bacterial contamination on banknotes and coins circulating in the area surrounding Chiang Mai University Hospital in Chiang Mai province and examine the tolerance of detected bacteria on the currency.

Materials and methods: Banknotes and coins, totaling 343 samples, were collected from circulation in the area surrounding Chiang Mai University Hospital in Chiang Mai. The bacterial contamination was studied based on culture methods and identified by morphological and biochemical tests. To examine the bacterial tolerance, the contaminated bacteria recovered from the currency, including *Staphylococcus aureus*, *Escherichia coli*, *Pseudomonas aeruginosa* and *Acinetobacter baumannii*, were tested. These bacteria were inoculated on banknotes and coins and the viability of the bacteria at various time points was examined.

Results: The amount of bacterial contamination on banknotes, which are linen fibers, was higher than those on coins, which are opaque metals. The gram-positive bacteria were found in a higher amount than gram-negative bacteria, in both banknotes and coins. Human skin flora and pathogenic bacteria, especially *S. aureus* and pathogenic Enterobacteriaceae, were detected. The bacterial tolerance study revealed that *S. aureus*, the gram-positive cocci, showed a decrease of viability on banknotes and coins within 6 hours. Meanwhile, gram-negative bacilli presented a decrease of viability in 6 and 1 hours on banknotes and coins, respectively. The bacterial tolerance testing by used and unused currency showed the same results.

Conclusion: All banknotes and coins circulating in the area surrounding Chiang Mai University Hospital in Chiang Mai province were demonstrated to be contaminated with bacteria, some of which might be pathogens and dangerous to users. Gram-positive bacteria has higher tolerance than gram-negative bacteria on currency. Bacterial tolerance on banknotes is longer than on coins. The knowledge obtained is advantageous for people in general as an awareness of these harmful bacteria when using the currency.

* Corresponding author.

Author's Address: Division of Clinical Microbiology, Department of Medical Technology, Faculty of Associated Medical Sciences, Chiang Mai University, Thailand

** E-mail address: pphunpae@hotmail.com

doi: 10.14456/jams.2018.23

E-ISSN: 2539-6056

Introduction

Currency, including banknotes and coins, are fomites ubiquitously handled and transferred in the course of our daily lives. Therefore, they have a high chance of becoming contaminated with bacteria. Many reports showed that a large amount of bacterial contamination appeared on banknotes in circulation.¹⁻³ This may lead to the spread of bacterial infection in people and the environment.⁴⁻⁶

Generally, money is transferred from hand to hand between healthy and/or pathogen infected people with repetitive contact thereafter. Contamination of bacteria on currency may come from mucus, cough, sneeze and wound secretion. Moreover, someone who holds banknotes and coins temporarily between his/her lip can bring in contamination from the environment. Thus, banknotes and coins are presented as a universal medium that carries potentially pathogenic bacteria.^{4,7} Without the awareness of the dangers, there is a high chance of bacterial infection in people when using contaminated currency.

The currency used in Thailand is comprised of Thai banknotes and Thai coins that are issued under the supervision of and manufactured by the Bank of Thailand and The Treasury Department. In the year 2016, numerous Thai coins were used in circulation, mainly in 25, 50 Satang, 1, 2, 5 and 10 Baht denominations; around the country, there were approximately 3321, 2407, 14,991, 1614, 3118 and 1816 million coins, respectively.⁸ Moreover, a large amount of banknotes, including 20, 50, 100, 500 and 1000 Baht were used in circulation: 88.4, 7.3, 14.1, 0.6 and 1.3 million notes, respectively.⁹ The bacteria contamination on banknotes and coins may originate from the production, storage and usage.^{10,11} There is an unpredictable chance and rare opportunity of cleaning or disinfecting money,¹² therefore, this may enhance pathogenic bacteria transmission. Consequently, bacterial contamination of currency may be a risk factor in the development of a public health problem.

Most bacterial contamination on banknotes and coins were reported, including coagulase-negative staphylococci, commonly from human natural skin flora, and gram-positive spore-forming bacilli, especially *Bacillus* spp., which are environmental organisms.³ Moreover, other potential pathogen bacteria, including *Staphylococcus aureus*, *Streptococcus* spp., *Escherichia coli*, *Proteus* spp., *Klebsiella* spp., *Enterobacter* spp., *Pseudomonas* spp., *Acinetobacter* spp., and *Salmonella* spp. are also commonly found.¹³ Some of these bacteria have been reported to survive well on the skin and can be transferred from hand to fabrics as well as from fabrics to hand.^{11,14} Thus, bacterial contamination related to currency is a significant topic which is reported from many parts of the world. However, the study of bacterial contamination of Thai banknotes and coins is scanty. In the present study, we determined the number and types of bacterial contamination of banknotes and coins circulating in the area surrounding Chiang Mai University Hospital in Chiang Mai province. The tolerance of bacteria on the currency was also examined.

Materials and methods

The currency used in this study

Currency, banknotes and coins used in this study were collected from those in common circulation in Chiang Mai. Different denominations of used banknotes and coins in a non-damaged state were randomly collected from people, patients, health care workers and students between April and September, 2016, in the hospital area and around the Faculty of Associated Medical Sciences, Chiang Mai University, as well as from the Treasury Department in Chiang Mai province. Meanwhile, unused new currency was obtained from a commercial bank and the Treasury Department in Chiang Mai.

Thai coins, including 25, 50 Satang and 2 Baht, consisting of 92% copper, 6% aluminum and 2% nickel were used to represent the commonly used copper alloy coin. One, 5 and 10 Baht, the commonly nickel alloy coins, consist of 75% copper and 25% nickel. Ten Baht coins also contain a ring inside comprised of 92% copper, 6% aluminum and 2% nickel.⁸ In addition, Thai banknotes used in this study were 20, 50, 100, 500 and 1000 Baht banknotes made from a cotton-linen blend.⁹

Between 20 and 30 samples were collected for each used denomination, totaling 343 samples. The new currency was collected in 27 samples per denomination for contamination study and tolerance test.

Sample processing

The banknotes or coins were placed individually into sterile polypropylene plastic bags, then transported to the Microbiology laboratory at the Faculty of Associated Medical Sciences, Chiang Mai University. Money was stored at room temperature until inoculation, which was carried out within 2 hours after collection.⁷

Extraction of bacteria from the banknotes and coins¹²

To study the number and types of bacterial contamination on banknotes and coins, each banknote and coin was aseptically placed individually into sterile tubes containing 20 and 10 ml of trypticase soy broth (TSB) (BD, Heidelberg, Germany), respectively. The samples were shaken for 30 minutes in an air conditioned room at 25 °C to remove the microorganisms from the currency into the medium. After that, the currency was aseptically removed with forceps.

Qualitative and quantitative bacterial analysis.⁷

The currency bacteria extracting media was diluted ten-fold and 0.1 ml of each dilution was spread onto sterile Petri dishes containing tryptic soy agar (BD), blood agar (Oxoid) and MacConkey (BD). The dishes were incubated aerobically for 24–48 hours at 35 °C.¹⁵ The colonies growing on media were counted using darkfield quebec colony counters (Reichert Technologies, USA). The total viable cells, referred to as colony forming units (CFU) per cm² and CFU per banknote and coin, were calculated. The isolated bacteria were identified by Gram staining, characterized on the basis of colony morphology and biochemical characteristics.¹⁰

The study of tolerance of bacteria on currency

Four bacterial species which were recovered in this study, including *Staphylococcus aureus* (gram-positive cocci bacteria), *Escherichia coli*, *Pseudomonas aeruginosa* and *Acinetobacter baumannii* (gram-negative bacilli bacteria), were used. All bacteria were subcultured individually at 37 °C in aerobic conditions and subsequently maintained on TSA (BD). Overnight cultures were prepared in tryptic soy broth (BD) at 37 °C. Broth cultures of each strain was prepared to equal the turbidity of a 0.5 McFarland standard (1×10^8 CFU/mL) using densitometer with the assistance of optical density followed by 1 in 100 dilution to obtain 1×10^6 CFU/ml. Unused or used banknotes and coins were sterilized using autoclaves at 121 °C, 15 lbs/in² for 15 minutes before use in the experiment. Then, bacteria at 10^6 CFU/ml 100 µl were spread onto unused new or used banknotes and 20 µl onto unused new or used coins, which then waited to dry in a biosafety cabinet. The bacteria from each sample were then extracted as described in qualitative and quantitative bacterial analysis. The survival of bacteria was studied¹⁶ at 0, 10, 30, 60 and 360 minutes after inoculation.

Results

Quantification and type of bacteria isolated from banknotes and coins circulating in Chiang Mai province

The mean number of viable bacteria isolated from circulating currency in Chiang Mai province were 58×10^2 CFU per cm² of banknote, $11,559 \times 10^2$ CFU per banknote, 41×10^2 CFU per cm² of coin and 466×10^2 CFU per coin, for all banknotes and coins studied. These results indicated that the amount of bacterial contamination on banknotes contained in linen fibers was much higher than that on coins, which are opaque metals.

As shown in Tables 1 and 2, gram-positive bacteria were found in a higher number than gram-negative bacteria, both in banknotes and coins. On banknotes, the recovery of gram-positive and gram-negative bacteria was $6,222 \times 10^2$ and $5,337 \times 10^2$ CFU/ banknotes, respectively (Table 1). The same pattern was observed in metal coins where the number of gram-positive and gram-negative bacteria was 242×10^2 and 224×10^2 CFU/coin, respectively (Table 2).

On the used banknotes, the highest to lowest number of bacteria was present in the following order

of denominations: 20, 100, 500, 1000 and 50 Baht banknote. Most microorganism recovered from banknotes were gram-positive bacteria, including coagulase-negative staphylococci, *Bacillus* spp., *Staphylococcus aureus*, *Enterococcus* spp., *Streptococcus* spp., *Micrococcus* spp., and other gram-positive bacteria (Table 1). However, gram-positive cocci catalase test positive *Micrococcus* spp., and gram-positive bacilli, including diphtheroid bacilli, were detected in low numbers in the tested currency (Table 1).

Various species of gram-negative bacteria in the Enterobacteriaceae family, comprised of *Enterobacter cloacae*, *Enterobacter aerogenes*, *Enterobacter sakazakii*, *Klebsiella ozaenae*, *Klebsiella pneumoniae*, *Citrobacter koseri* and *Escherichia coli* were recovered from the tested banknotes. Moreover, non-fermenting bacteria, including *Acinetobacter baumannii*, *Acinetobacter lwoffii*, *Pseudomonas aeruginosa* and *Stenotrophomonas maltophilia* were also detected (Table 1).

On the used coins, the highest to lowest number of bacteria was present in the following order of denominations: 1, 5, 10 Baht, 50 Satang, 2 Baht and 25 Satang coins (Table 2). Most bacteria recovered from coins were gram-positive including coagulase-negative staphylococci, *S. aureus*, *Streptococcus* spp., *Enterococcus* spp., *Bacillus* spp., Diphtheroid bacilli, *Micrococcus* spp., and other gram-positive bacteria (Table 2). In addition, a large number of gram-negative bacteria, including Enterobacteriaceae and non-fermenting bacteria, were detected on coins (Table 2).

It was found that in 100% of the samples in common circulation studied, both used banknotes and coins were contaminated with bacteria. However, no bacteria was found in unused new banknotes and coins obtained from the Treasury Office and the banks. It was found that gram-positive bacteria were detected at a higher rate than gram-negative bacteria. Interestingly, *E. coli*, the member of coliform enteric bacteria, was also detected in used banknotes and coins. Additionally, gram-negative bacilli non-fermented group, which may cause hospital acquired infection,¹⁷ comprised of *A. baumannii*, *P. aeruginosa*, *S. maltophilia* and *A. lwoffii*, were also detected in the tested currency. However, many of the bacterial contaminations in the tested currency were identified as commensalism bacteria, especially coagulase-negative *Staphylococcus* spp., *Bacillus* spp., *Micrococcus* spp., and *Neisseria* spp.

Table 1 Amount of bacterial isolation from banknotes in circulation in areas surrounding Chiang Mai University Hospital in Chiang Mai Province.

Microorganisms Bacteria	Frequency of isolation as total viable counts* (x 10 ² CFU) Banknotes (denominations; Baht)					Total viable countx10 ² CFU (%)
	20 Baht	50 Baht	100 Baht	500 Baht	1000 Baht	
Coagulase-negative staphylococci	668±0.14	143±1.1	810 ± 0.25	686 ± 0.23	254±0.32	2560±2.04 (22.1)
<i>Staphylococcus aureus</i>	146±0.41	1±0.71	103±0.21	129±0.43	28±0.33	422±2.09 (3.7)
<i>Streptococcus</i> spp.	15±0.32	16±0.43	23±0.22	17±0.75	28 ± 0.56	100±2.28 (0.9)
<i>Enterococcus faecalis</i>	23±0.87	9±0.98	18±0.23	7±0.11	5 ± 0.32	61±2.51 (0.5)
<i>Enterococcus</i> spp.	44±0.76	23±0.79	32±0.42	80±0.77	54±0.98	233±3.72 (2.0)
<i>Bacillus</i> spp.	697±0.11	302±0.23	389±0.55	337±1.02	366±0.45	2090±2.36 (18.1)
Diphtheroid bacilli	86±0.43	23±0.22	162±0.56	79±0.21	35 ± 0.13	385±1.55 (3.3)
<i>Micrococcus</i> spp.	23±0.54	9±0.33	19±0.87	22±0.43	23 ± 88	96±3.05 (0.8)

Table 1 Amount of bacterial isolation from banknotes in circulation in areas surrounding Chiang Mai University Hospital in Chiang Mai Province. (continues)

Microorganisms Bacteria	Frequency of isolation as total viable counts* (x 10 ² CFU) Banknotes (denominations; Baht)					Total viable countx10 ² CFU (%)
	20 Baht	50 Baht	100 Baht	500 Baht	1000 Baht	
Other gram-positive bacteria	78±1.02	28±1.03	63±0.46	70±0.43	38 ± 0.34	276±3.28 (2.4)
Gram-positive bacteria number/ denomination	1778±4.60	569±5.82	1618±3.77	1426±4.38	831±4.31	6222 (53.8)
<i>Enterobacter cloacae</i>	294±0.18	79±0.19	227±0.32	238±0.43	141±0.47	979±1.59 (8.5)
<i>Enterobacter aerogenes</i>	24±0.87	16±0.32	16±0.12	22±0.21	17±0.32	94±1.84 (0.8)
<i>Enterobacter sakazakii</i>	30±0.78	16±0.32	65±0.97	13±0.86	15±0.54	138±3.47 (1.2)
<i>Klebsiella ozaenae</i>	114±0.23	48±0.54	194±1.02	179±0.99	56±0.76	592±3.54 (5.1)
<i>Klebsiella pneumoniae</i>	89±0.78	48±0.46	97±0.43	119±0.14	35±0.43	388±2.24 (3.4)
<i>Citrobacter koseri</i>	68±0.33	32±0.12	32±0.89	99±0.53	35±0.77	267±2.64 (2.3)
<i>Escherichia coli</i>	23±0.39	14±1.12	45±0.39	50±0.88	10±0.88	142±3.66 (1.2)
<i>Acinetobacter baumannii</i>	254±0.87	111±0.57	162±0.34	269±0.33	113±0.34	909±2.45 (7.9)
<i>Acinetobacter lwoffii</i>	51±0.90	32±0.87	162±0.46	179±0.87	28±0.88	453±3.98 (3.9)
<i>Pseudomonas aeruginosa</i>	130±0.98	58±0.12	97±0.32	90±0.11	37±0.21	411±1.74 (3.6)
<i>Stenotrophomonas maltophilia</i>	23±0.33	48±0.78	65±0.98	90±0.76	15±0.34	240±3.19 (2.1)
<i>Pantoea agglomerans</i>	126±0.23	16±0.33	162±0.21	90±1.09	28±0.65	421±2.51 (3.6)
<i>Neisseria</i> spp.	33±0.43	35±0.22	32±0.54	47±0.78	13±0.34	161±2.31 (1.4)
Other gram-negative bacteria	43±0.33	16±0.78	32±0.45	16±0.33	35±0.24	141±2.13 (1.2)
Gram-negative bacteria number/denomination	1302±7.63	567±6.74	1389±7.44	1500±8.31	579±7.17	5337 (46.2)
Total bacterial number	3080	1136	3007	2927	1409	11559 (100)

* Values are means of three replicates for each denomination.

Table 2 Amount of bacterial isolation from Thai coins in circulation in areas surrounding Chiang Mai University Hospital in Chiang Mai Province.

Microorganisms Bacteria	Frequency of isolation as total viable counts (x 10 ² CFU) Coins (denominations; Baht)						Total viable countx10 ² CFU (%)
	25 Satang	50 Satang	1 Baht	2 Baht	5 Baht	10 Baht	
Coagulase-negative staphylococci	7±0.42	8±0.63	11±0.56	9±0.67	12±0.98	11±1.13	58±4.39 (12.4)
<i>Staphylococcus aureus</i>	4±0.12	5±0.44	7±0.73	5±1.01	9±0.78	8±0.23	38±3.31 (8.2)
<i>Streptococcus</i> spp.	3±0.22	4±0.21	4±0.22	4±0.31	3±0.32	4±0.07	22±1.35 (4.7)
<i>Enterococcus</i> spp.	3±0.23	3±0.43	4±1.01	3±0.32	3±0.33	3±0.23	19±2.55 (4.1)
<i>Bacillus</i> spp.	7±0.88	8±0.43	11±0.21	9±0.13	11±0.43	12±0.54	58±2.62 (12.4)
Diphtheroid bacilli	3±0.76	3±0.45	3±0.23	2±0.43	3±0.31	3±0.15	17±2.33 (3.6)
<i>Micrococcus</i> spp.	2±0.10	2±0.76	2±0.33	2±0.14	1±0.22	1±0.43	10±1.98 (2.1)
Other gram-positive bacteria	3±0.65	3±0.53	4±1.13	3±0.67	4±0.33	3±0.87	20±4.18 (4.3)
Gram-positive bacteria number/denomination	32±3.38	36±3.88	46±4.42	37±3.68	46±3.70	45±3.65	242 (51.9)
<i>Enterobacter cloacae</i>	4±0.18	5±0.24	7±0.32	6±0.43	6±0.14	4±0.56	32±1.87 (6.9)
<i>Enterobacter aerogenes</i>	4±0.5	4±0.33	5±0.70	4±0.23	4±0.87	5±0.32	26±2.95 (5.6)
<i>Klebsiella ozaenae</i>	4±0.64	4±0.53	5±0.71	4±0.23	4±0.78	4±1.01	25±3.90 (5.4)
<i>Klebsiella pneumoniae</i>	2±0.24	3±0.32	3±0.11	2±0.87	3±0.56	4±0.89	17±2.99 (3.6)
<i>Escherichia coli</i>	2±0.31	3±0.45	4±0.67	3±0.43	3±0.88	3±0.44	18±3.18 (3.9)
<i>Acinetobacter baumannii</i>	4±0.21	5±1.01	6±0.43	3±0.32	5±0.55	3±0.45	26±2.97 (5.6)
<i>Acinetobacter lwoffii</i>	4±0.89	4±0.77	5±0.64	2±0.98	4±0.35	3±1.1	22±4.73 (4.7)
<i>Pseudomonas aeruginosa</i>	4±0.24	5±0.31	7±0.23	5±0.22	6±0.12	5±0.21	32±1.33 (6.9)
<i>Neisseria</i> spp.	1±0.98	1±0.43	2±0.32	1±0.22	1±0.53	1±0.35	7±2.83 (1.5)
Other gram-negative bacteria	3±0.54	3±0.31	4±0.75	3±0.31	3±1.03	3±0.43	19±3.37 (4.1)

Table 2 Amount of bacterial isolation from Thai coins in circulation in areas surrounding Chiang Mai University Hospital in Chiang Mai Province. (continues)

Microorganisms Bacteria	Frequency of isolation as total viable counts (x 10 ² CFU) Coins (denominations; Baht)						Total viable countx10 ² CFU (%)
	25 Satang	50 Satang	1 Baht	2 Baht	5 Baht	10 Baht	
Gram-negative bacteria number/denomination	32±4.73	37±4.70	48±4.88	33±4.24	39±5.81	35±5.76	224 (48.1)
Total bacterial number	64	73	94	70	85	80	466 (100)

* Values are means of three replicates for each denomination.

Study of tolerance of bacteria on Thai currency

Four species of isolated bacteria from banknotes and coins, including *Staphylococcus aureus* (gram-positive cocci), *E. coli* (coliform gram-negative bacilli), *Pseudomonas aeruginosa* and *Acinetobacter baumannii* (non-fermenting gram-negative bacilli), were selected for the bacterial tolerance test. Three bacterial isolates of each species were randomly selected for the bacterial tolerance test. The currency, including 25 Satang coins (copper coin), 1 Baht coin (nickel alloy coin), 20 and 100 Baht banknotes were used in the bacterial tolerance study. We also compared the bacterial tolerance between unused and used denominations of coins and banknotes by detecting the viability of bacteria after inoculating bacteria for 0 to 360 minutes.

In the study of bacterial tolerance of banknotes, the decrease of viability of bacteria was observed in the same pattern as the test between used and unused 20 and 100 Baht banknotes (Figure 1). *Staphylococcus aureus* showed viability on used and unused banknote by persisting longer than 6 hours (Figure 1B). Moreover, *S. aureus* showed more tolerance than *E. coli*, *P. aeruginosa* and *A. baumannii* on

banknotes at 360 minutes (Figure 1B, 1F, 1H). In addition, these microorganisms showed more tolerance on banknotes than on coins at 360 minutes (Figure 1A, 1B).

Studying bacterial tolerance on coins, *Staphylococcus aureus* showed viability on 25 Satang copper coins test until 6 hours in unused and used coins and more tolerance on 1 Baht nickel coins test by persistence longer than 6 hours (Figure 1A). The gram-negative bacteria, *E. coli* and *P. aeruginosa* showed low viability at 1 hour on coins (Figure 1C, 1E), whereas *A. baumannii* showed low viability at 30 minutes on both unused and used 25 Satang copper coins (Figure 1G). The viability of *E. coli*, *P. aeruginosa* and *A. baumannii* on nickel coins indicated low viability at 60 minutes on both unused and used coins (Figure 1C, 1E, 1G).

These studies have illustrated that bacteria generally has better tolerance on banknotes than on coins. The decrease of viability of bacteria was observed in the same pattern when comparing unused and used coins and banknotes. The viability of all tested bacteria decreased considerably in the first hour on the surface of the currency (Figure 1).

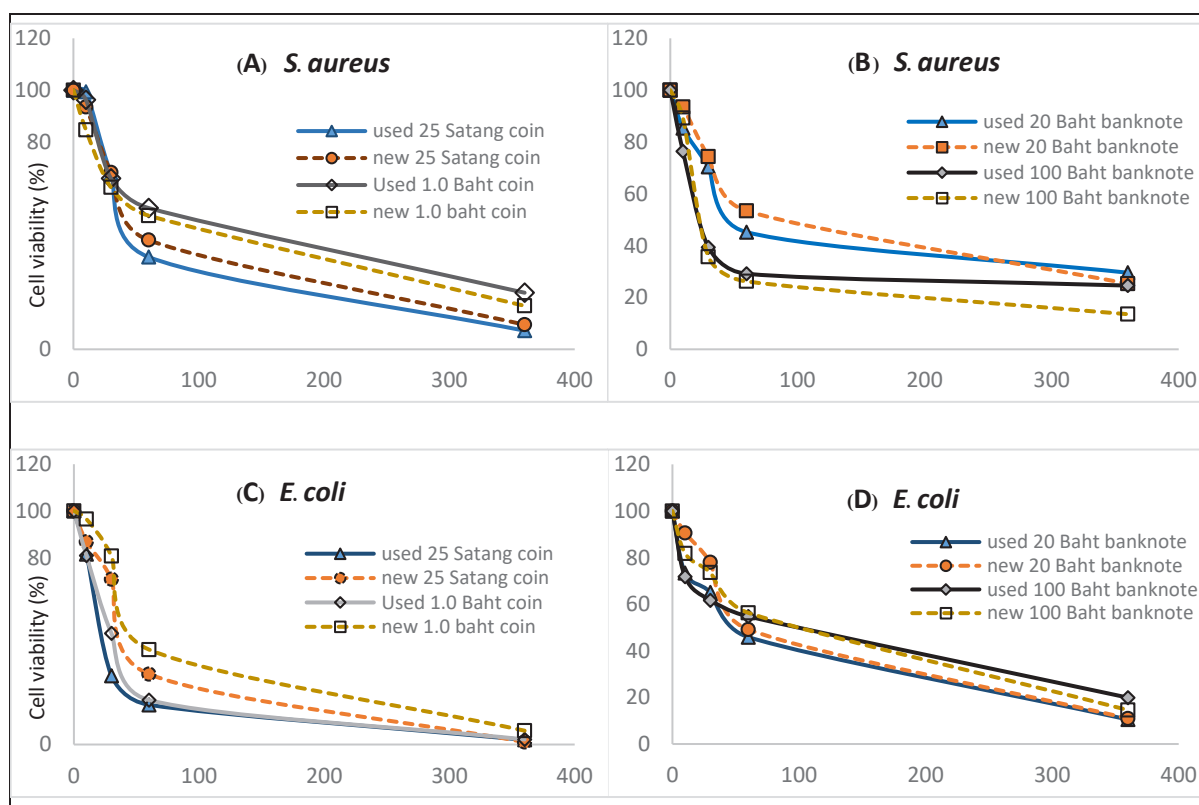


Figure 1 Cell viability of bacteria during exposure for 0 to 360 minutes on surface of new and used 25 Satang and 1 Baht coins, *Staphylococcus aureus* (A), *Escherichia coli* (C), *Pseudomonas aeruginosa* (E) and *Acinetobacter baumannii* (G). Cell viability of bacteria during exposure for 0 to 360 minutes on surface of new and used 20, 100 Baht banknotes, *Staphylococcus aureus* (B), *Escherichia coli* (D), *Pseudomonas aeruginosa* (F) and *Acinetobacter baumannii* (H).

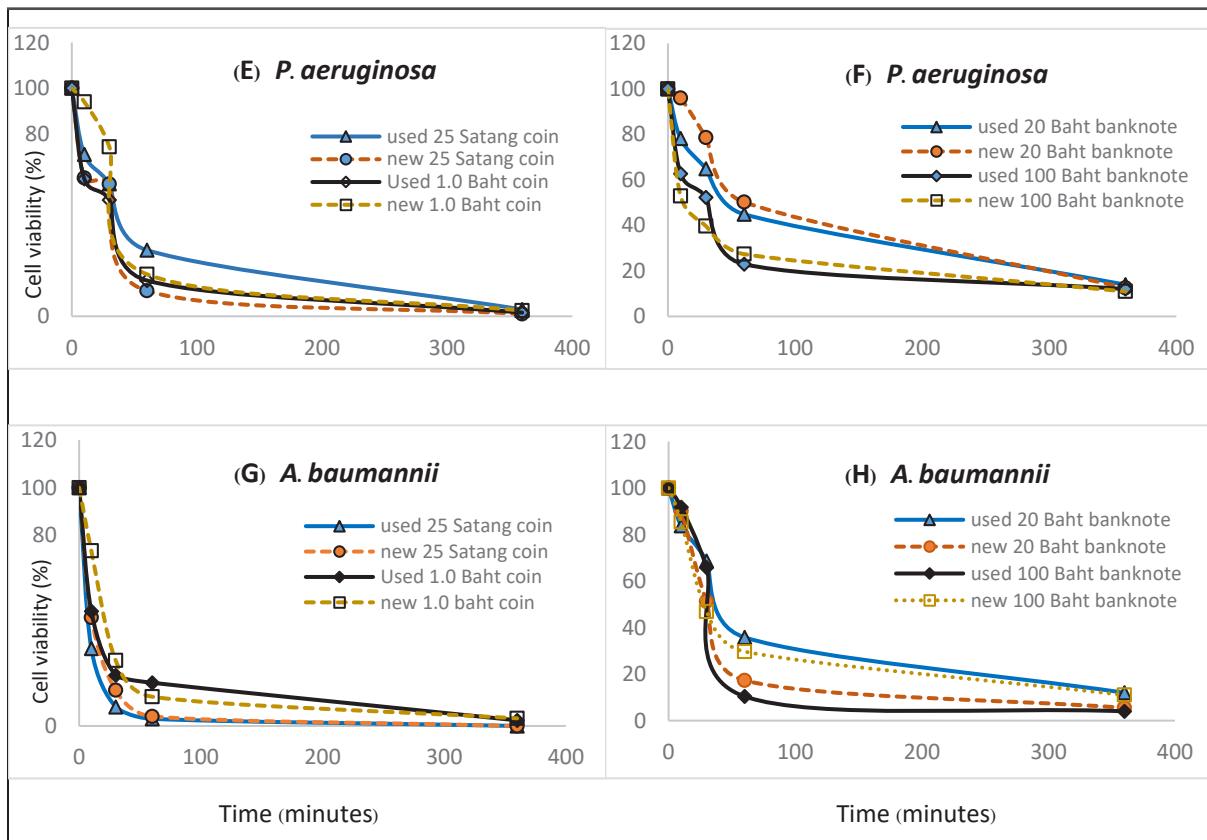


Figure 1 Cell viability of bacteria during exposure for 0 to 360 minutes on surface of new and used 25 Satang and 1 Baht coins, *Staphylococcus aureus* (A), *Escherichia coli* (C), *Pseudomonas aeruginosa* (E) and *Acinetobacter baumannii* (G). Cell viability of bacteria during exposure for 0 to 360 minutes on surface of new and used 20, 100 Baht banknotes, *Staphylococcus aureus* (B), *Escherichia coli* (D), *Pseudomonas aeruginosa* (F) and *Acinetobacter baumannii* (H).

Discussion

Banknotes and coins are used in everyday life by everybody; however, they might be a source of bacterial contamination and even a source of infections. In general, we usually use currency without the awareness of the danger from potential bacterial infections in different parts of the body. This may be due to a lack of information related to bacterial prevalence on the currency used. Therefore, studying the type, number and the persistence of bacteria on the currency can provide significant baseline data for the prevention of bacterial infection that may occur. In this study, the quantity and types of bacterial contamination on banknotes and coins circulating in the area surrounding Chiang Mai University Hospital in Chiang Mai province were disclosed. The tolerances of bacteria on the currency were also revealed.

In this study, the experiments were carried out by conventional culture methods which are related to many studies.^{13, 18} We found that 100% of used currency samples collected in the area surrounding Chiang Mai University Hospital in Chiang Mai province were contaminated with bacteria. In contrast, unused new banknotes and coins tested under the same conditions showed no presence of bacterial contamination. We speculated that new currency from the production line was subjected to a cleaning or sanitization process which can destroy bacterial contamination. The contamination found in the used currency might have come from bacteria deposited during daily use.

In this study, we found that bacterial contamination was higher in banknotes than in coins. This may be because banknotes contain many fibers that form a porous surface,¹⁹ which can easily trap bacteria. In contrast, the physical structure of coins is smooth and contains metals, such as copper, exhibiting anti-bacterial properties.²⁰ Moreover, a higher number of bacterial contamination on used currency corresponds to a lower value of the currency, such as 20 Baht banknotes or 1 Baht coins being the most contaminated; this may be due to a higher frequency of usage. Our results are compatible with a report from the Bank of Thailand that the denominations of banknote used most frequently, from highest to lowest, are 20, 100, 1000, 50 and 500 Baht, respectively.⁹ In agreement with the report from the Treasury Department that the large amount of coin currency used in circulation, the highest number was 1 Baht coins, and the number decreased respectively in 25 Satang, 5 Baht, 50 Satang, 10 and 2 Baht.

On both banknotes and coins, gram-positive bacteria were found in higher numbers than gram-negative bacteria. The predominate gram-positive bacterial contaminations were gram-positive bacilli, especially *Bacillus* spp. which is normally found in nature and human natural skin flora.¹³ Meanwhile, *Staphylococcus* spp. was the predominate gram-positive and catalase-positive cocci, including coagulase-negative staphylococci, which is normally detected in human skin flora,^{3, 15} and *Staphylococcus aureus* that can cause skin infection, abscess, furuncle, boil and

a number of diseases. *Bacillus* spp. and *Staphylococcus* spp. were predominately found on copper coins, in line with that report from Santo et al., 2012.

Furthermore, in this study, gram-negative bacteria were also recovered, especially in the Enterobacteriaceae group. The *Enterobacter* and *Klebsiella* that were found on the tested currency are related to enteric bacteria. Interestingly, coliform bacteria such as *Escherichia coli*, which can be detected in the gastrointestinal system of humans, were also found in the tested currency. This bacterial species is an indicator of fecal contamination.²¹ This is a useful data to raise awareness of personal hygiene related to fecal-oral route transmission and infection. Moreover, non-fermenting gram-negative bacteria were also recovered from the currency circulating in Chiang Mai province. Most contaminate non-fermenters are *Acinetobacter* spp. and *Pseudomonas* spp. Bacteria in these groups can be found in the environment and can cause hospital acquired infection and a high number of drug resistant bacteria were reported.¹⁷ Moreover, *Stenotrophomonas maltophilia*, an emerging multidrug-resistant, globally opportunistic bacteria, was also detected. These bacteria are normally found in the hospital,²² which is in concordance to the places of collected currency samples in this study, i.e. the area surrounding Chiang Mai University Hospital. Therefore, some types of bacteria recovered from this study include pathogenic bacteria and may cause disease in humans that the general population should be aware of. This detection showed the possibility of bacteria spreading from hospital to community via banknotes and coins.

In the tolerance test of bacteria, four bacterial species were selected in the study. *Staphylococcus aureus*, the gram-positive cocci that can cause skin infection in humans²³ were used as representative of gram-positive bacteria. *Escherichia coli*, the gram-negative bacilli normally found in the small and large intestines²⁴ were used as representative of gram-negative fecal coliform bacteria. In addition to *Pseudomonas aeruginosa* and *Acinetobacter baumannii*, gram-negative bacilli that might cause hospital acquired infection and environmental infection, were selected as representative of non-fermenting gram-negative bacilli. We found that many bacteria can survive only a few days on coins and banknotes. This data, however, was different from the studies of Kramer et al., 2006, which showed that many bacteria including *Streptococcus pyogenes*, *Staphylococcus aureus*, *Klebsiella* spp., *Acinetobacter* spp., *E. coli* and *Pseudomonas aeruginosa* may survive for months on dry surfaces.²⁵ We speculated that the different climate in the studied area and the currency component of banknotes and coins studied may cause the different results. The survival viability of bacteria indicated that gram-positive bacteria such as *Staphylococcus* spp. can survive longer than gram-negative bacteria. Previous reports showed that gram-positive bacteria are comprised of thick cell walls, which made them tolerant to the environment.²⁰ On the other hand, gram-negative bacilli contain thinner cell walls, causing a shorter time of survival in a non-optimal environment. While the results showed that gram-positive and gram-negative bacterial persistence was short lived,

we still detected bacteria; this might be because bacteria were being transferred from hand or from the environment onto money continuously. Therefore, some of the bacteria detected may have been a transient bacterial contamination. In order to prevent and control infection from the use of cash, the currency should be cleaned, as reported in Japan, by heat-sterilization of money or replacement with polymer banknotes.¹⁸

Used and unused currency may show different structural changes and differences in chemical contamination, which may affect the survival of bacteria on them. Thus, the study of tolerance of bacteria on currency was conducted with used and unused, sterile currency. However, the results of the tolerance study of bacteria in used and unused currency showed no difference. This might be because bacteria used in this study, including *Staphylococcus aureus*, a gram-positive cocci, has a thick cell wall that provides durability on the surface of used and unused currency.²⁰ However, gram-negative bacilli studied, including *P. aeruginosa*, *A. baumannii* and *E. coli*, are able to adapt themselves to the surface of currency.²⁶ In addition, time used in this study of was limited to 6 hours. Some bacteria were still alive. The result of tolerance of bacteria on used and unused cash, therefore, showed no difference.

Furthermore, this study has some limitations. Firstly, bacterial contamination on Thai currency in this study was cultured in simple media. Therefore, it was possible that fastidious bacteria (bacteria that have a complex nutritional requirement) was not detected in this study. Secondly, it was conducted to study only bacterial contamination on currency and not other microorganisms, including fungus, virus and parasite. Consequently, other microorganism should be identified in further studies. Thirdly, currency samples studied were collected in a limited area surrounding the university hospital and the Faculty of Associated Medical Sciences. However, samples should be collected in many places in order to get more information of bacterial contamination on currency. Fourthly, in the study of tolerance of bacteria on currency, there were four bacteria species tested. However, these bacteria might not be representative of all bacteria species. For additional benefits, the inclusion of other bacteria species is needed for further studies. Finally, time used in the study of tolerance of bacteria ranged from 0 to 6 hours; the result was that some bacteria were still alive. Therefore, tolerance should be studied for longer than 6 hours.

Taken together, in this study we presented information about bacteria contamination on banknotes and coins in Chiang Mai province. We, however, believe that the same situation might be occurring in other provinces of Thailand. The information obtained from this study might have some advantages, including: i) the baseline information of the amount and types of bacteria on the currency used in Chiang Mai province; ii) the prevalence of the contaminated bacteria on new and used coins and banknotes; and iii) the tolerance of gram-positive and gram-negative bacteria on new and used coins and banknotes. This study demonstrated that banknotes and coins in circulation have much bacterial contamination, some of which might contain pathogens

and are dangerous to human users. This knowledge is beneficial for people in general, as awareness of these harmful bacteria points to the necessity of cleaning and washing hands after using banknotes and coins for preventing bacterial contamination on coins and banknotes.

Conflict of interest:

The authors declare no conflict of interest.

Acknowledgements

This work was supported by The Faculty of the Associated Medical Sciences, Chiang Mai University grant in 2016. The authors wish to acknowledge Prof. Dr. Watchara Kasinrerk of the Faculty of Associated Medical Sciences, Chiang Mai University, for his suggestions, reading and helpful guidance in the preparation of this manuscript. The authors acknowledge Mrs. Pornpimon Khaipa and Mr. Tanasak Limpipatchai for their assistance in sample collection.

References

- [1] El-Dars FM, Hassan WM. A preliminary bacterial study of Egyptian paper money. *Int J Environ Health Res.* 2005; 15(3): 235-9.
- [2] Basavarajappa KG, Rao PN, Suresh K. Study of bacterial, fungal, and parasitic contamination of currency notes in circulation. *Indian J Pathol Microbiol.* 2005; 48(2): 278-9.
- [3] Xu J, Moore JE, Millar BC. Ribosomal DNA (rDNA) identification of the culturable bacterial flora on monetary coinage from 17 currencies. *J Environ Health.* 2005; 67(7): 51-5.
- [4] Khin NO, Phyu PW, Aung MH, Aye T. Contamination of currency notes with enteric bacterial pathogens. *J. Diarrhoeal. Dis. Res.* 1989, 7(3-4): 92-4.
- [5] Kuria JK, Wahome RG, Jobalamin M, Kariuki SM. Profile of bacteria and fungi on money coins. *East Afr Med J.* 2009; 86(4): 151-5.
- [6] Yazah AJ, Yusuf J, Agbo J. Bacterial contaminants of Nigerian currency notes and associated risk factors. *Res J Med Sci.* 2012; 6(1): 1-6.
- [7] Kalita M, Palusińska-Szyszk M, Turska-Szewczuk A, Wdowiak-Wrobel S, Urbanik-Sypniewska T. Isolation of cultivable microorganisms from Polish notes and coins. *Pol J Microbiol.* 2013; 62(3): 281-6.
- [8] The Treasury Department: Thai coins [Internet]. Bangkok; 2561 [cited 2018 5 May]. Available from: https://www.m-society.go.th/ewt_news.php?nid=16328.html.
- [9] The Bank of Thailand: Volume and Value of Notes in Circulation [Internet]. Bangkok; 2561 [cited 2018 5 May]. Available from: <https://www.bot.or.th/Thai/Banknotes/Pages/banknoteinfo.aspx.html>.
- [10] Hugo WB, Denyer SP, Hodges NA, Gorman SP, Russel AD. *Pharmaceutical Microbiology.* Oxford: Blackwell Scientific; 1983.
- [11] Igumbor EO, Obi CL, Bessong PO, Potgieter N, Mkasi TC. Microbiological analysis of banknotes circulating in the Venda region of Limpopo province, South Africa. *S Afr J Sci.* 2007; 103(9-10): 365-6.
- [12] Vriesekoop F, Chen J, Oldaker J, Besnard F, Smith R, Leversha W, et al. Dirty money: A matter of bacterial survival, adherence, and toxicity. *Microorganisms.* 2016; 4(4): 42.
- [13] Vriesekoop F, Russell C, Alvarez-Mayorga B, Aidoo K, Yuan Q, Scannell A, et al. Dirty money: an investigation into the hygiene status of some of the world's currencies as obtained from food outlets. *Foodborne Pathog Dis.* 2010; 7(12): 1497-502.
- [14] Mackintosh CA, Hoffman PN. An extended model for transfer of micro-organisms via the hands: differences between organisms and the effect of alcohol disinfection. *J. Hyg.* 1984; 92(3): 345-55.
- [15] Sawalha H, Mowais MA. Bacterial contamination of paper banknotes in circulation; A case study in the Jenin district, Palestine. *J Sci.* 2012; 1(2): 36-9.
- [16] de Carvalho CC, Caramujo MJ. Bacterial diversity assessed by cultivation-based techniques shows predominance of *Staphylococcus* species on coins collected in Lisbon and Casablanca. *FEMS Microbiol Ecol.* 2014; 88(1):26-37.
- [17] Mehrad B, Clark NM, Zhanel GG, Lynch JP. Antimicrobial resistance in hospital-acquired gram-negative bacterial infections. *Chest.* 2015; 147(5): 1413-21.
- [18] Prasai T, Yami KD, Joshi DR. Microbial load on paper/polymer currency and coins. *Nepal J Sci Technol.* 2008; 9: 105-9.
- [19] Lopez GU, Gerba CP, Tamimi AH, Kitajima M, Maxwell SL, Rose JB. Transfer efficiency of bacteria and viruses from porous and nonporous fomites to fingers under different relative humidity conditions. *Appl Environ Microbiol.* 2013; 79(18): 5728-34.
- [20] Santo CE, Quaranta D, Grass G. Antimicrobial metallic copper surfaces kill *Staphylococcus haemolyticus* via membrane damage. *MicrobiologyOpen.* 2012 ; 1(2): 46-52.
- [21] Odonkor ST, Ampofo JK. *Escherichia coli* as an indicator of bacteriological quality of water: an overview. *Microbiol Res* 2013; 4: 5-11.
- [22] Brooke JS. *Stenotrophomonas maltophilia*: an emerging global opportunistic pathogen. *Clin Microbiol Rev.* 2012; 25(1): 2-41.
- [23] Miller LG, Eells SJ, David MZ, Ortiz N, Taylor A, Kumar N, et al. *Staphylococcus aureus* skin infection recurrences among household members: An examination of host, behavioral, and pathogen-level predictors. *Clin Infect Dis* 2015; 60(5): 753-63.
- [24] Conway T and Cohen PS. Commensal and pathogenic *Escherichia coli* metabolism in the gut. *Microbiol Spectr.* 2015; 3(3): 343-62.

[25] Kramer A, Schwebke I, Kampf G. How long do nosocomial pathogens persist on inanimate surfaces? A systematic review. *BMC Infect Dis* 2006; 6: 130.

[26] Roy H, Dare K, Ibba M. Adaptation of the bacterial membrane to changing environments using aminoacylated phospholipids. *Mol Microbiol.* 2009; 71(3): 547–50.

Instructions for Authors

Instructions for Authors

Original article/thesis can be submitted through the on-line system via website <https://www.tci-thaijo.org/index.php/bulletinAMS/>

General Principles

Journal of Associated Medical Sciences is a scientific journal of the Faculty of Associated Medical Sciences, Chiang Mai University. The articles submitted to the journal that are relevant to any of all aspects of Medical Technology, Physical Therapy, Occupational Therapy, Radiologic Technology, Communication Disorders, and other aspects related to the health sciences are welcome. Before publication, the articles will go through a system of assessment and acceptance by at least three experts who are specialized in the relevant discipline. All manuscripts submitted to Journal of Associated Medical Sciences should not have been previously published or under consideration for publication elsewhere. All publications are protected by the Journal of Associated Medical Sciences' copyright.

Manuscript categories

1. **Review articles** must not exceed 20 journal pages (not more than 5,000 words), including 6 tables/figures, and references (maximum 75, recent and relevant).
2. **Original articles** must not exceed 15 journal pages (not more than 3,500 words), including 6 tables/figures, and 40 reference (maximum 40, recent and relevant).
3. **Short communications** including technical reports, notes, and letter to editor must not exceed 5 journal pages (not more than 1,500 words), including 2 tables/figures, and references (maximum 10, recent and relevant).

Manuscript files

To submit your manuscript, you will need the following files:

1. A Title page file with the names of all authors and corresponding authors*
2. Main document file with abstract, keywords, main text and references
3. Figure files
4. Table files
5. Any extra files such as Supplemental files or Author Biographical notes

Manuscript Format

1. **Language:** English, Caribri 10 for text and 7 for all symbols. PLEASE be informed that the Journal only accept the submission of English manuscript.
2. **Format:** One-side printing, double spacing. Use standard program and fonts and, add page and line number for all pages.
3. **A Title page:** Include article title, names of all authors and co-authors, name of the corresponding author and acknowledgements. Prepare according to following contents;
 - *Title of the article:* Concise and informative. Titles are often used in information-retrieval systems. Avoid abbreviations and formulate where possible.
 - *Author names and affiliation:* Where the family name may be ambiguous (e.g. a double name), please indicate this clearly. Present the authors' affiliation addresses (where the actual work was done) below the names. Indicate all affiliations with superscript number immediately after author's name and in front of appropriate address. Provide the full postal address of each affiliation, including the province, country and, if available, the e-mail address of each author.
 - *Corresponding author:* Clearly indicate who will handle correspondence at all stages of refereeing and publication, also post-publication, ensure that telephone and fax numbers (with postal area code) are provided in addition to the e-mail address and the complete postal address. Contact details must be kept up to date by the corresponding author.
 - *Acknowledgements:* Acknowledgements will be collated in a separate section at the end of the article before the references in the stage of copyediting. Please, therefore, include them on the title page, List here those individuals who provided help during the research (e.g. providing language help, writing assistance or proof reading the article, etc.)
4. **Main article structure:** The manuscripts should be arranged in the following headings: Title, Abstract, Introduction, Materials and Methods, Results, Discussion and Conclusion, and Reference. Prepare according to following contents;
 - *Abstract:* Not exceeding 400 words, abstract must be structured with below headings in separated paragraph:
 - Background,
 - Objectives,
 - Materials and methods,
 - Results,
 - Conclusion, and
 - Keywords (3-5 keywords should be included)
 - *Introduction:* State the objectives of work and provide an adequate background, avoiding a detailed literature survey or a summary of the results.
 - *Materials and Methods:* Provide sufficient detail to allow the work to be reproduced. Methods already published should be indicated by a reference, only relevant modifications should be described. Ensure that each table, graph, or figure is referred in the text. According to the policy of ethical approval, authors must state the ethical approval code and conduct informed consent for human subject research (If any) and for animal research, authors must include a statement or text describing the experimental procedures that affirms all appropriate measures (if any) in this section.
 - *Results:* Results should be clear and concise. Present the new results of the study such as tables and figures mentioned in the main body of the article and numbered in the order in which they appear in the text or discussion.
 - *Discussion:* This should explore the significance of the results of the work, not repeat them. A combined Results and Discussion

section is often appropriate. Avoid extensive citations and discussion of published literature.

- **Conclusion:** The main conclusions of the study may be presented in a short Conclusions section, which may stand alone or form a subsection of a "Discussion" or "Results and Discussion".
- **Conflict of interest:** All authors must declare any financial and personal relationship with other people or organization that could inappropriately influence (bias) their work. If there is no interest to declare, then please state this: "The authors declare no conflict of interest".
- **Ethic approval:** Ethic clearance for research involving human and animal subjects.
- **References:** Vancouver's style.

5. Artwork Requirements

- Each table, graph and figure should be self-explanatory and should present new information rather than duplicating what is in the text. Prepare one page per each and submit separately as supplementary file(s).
- Save the figures as high resolution JPEG or TIFF files.

Note: Permission to reprint table(s) and/or figure(s) from other sources must be obtained from the original publishers and authors and submitted with the typescript.

Ensuring a blind peer review

To ensure the integrity of the double-blinded peer-review for submission to this journal, every effort should be made to prevent the identities of the authors and reviewers from being known to each other. The authors of the document have deleted their names from the main text, with "Author" and year used in the references and footnotes, instead of the authors' name, article title, etc. After the journal was accepted, the name of authors and affiliation and the name of the corresponding author must be included into the document and re-submitted in the copyediting stage.

Proof correction

The Proofs of final paper approved for publication are to be returned by email to the researcher before publication.

Page charge

No page charge.

References Format

1. References using the Vancouver referencing style (see example below).
2. In-text citation: Indicate references by number(s) in the order of appearance in the text with superscript format. Reference numbers are to be placed immediately after the punctuation (with no spacing). The actual authors can be referred to, but the reference number(s) must always be given. When multiple references are cited at a given place in the text, use a hyphen to join the first and last numbers that are inclusive. Use commas (with no spacing) to separate non-inclusive numbers in a multiple citation e.g. (2-5,7,10). Do not use a hyphen if there are no citation numbers in between inclusive statement e.g. (1-2). Use instead (1,2).
3. References list: number the references (numbers in square brackets) in the list must be in the order in which they are mentioned in the text. In case of references source from non-English language, translate the title to English and retain "in Thai" in the parentheses.
4. Please note that if references are not cited in order the manuscript may be returned for amendment before it is passed on to the Editor for review.

Examples of References list

Multiple Authors: List up to the first 6 authors/editors, and use "et al." for any additional authors.

Journal Articles (print): In case of reference source contains DOI, retain doi: at the end of reference. Vancouver Style does not use the full journal name, only the commonly-used abbreviation: "Physical Therapy" is cited as "Phys Ther". As an option, if a journal carries continuous pagination throughout a volume (as many medical journals do) the month and/or issue number may be omitted. Allow one space after semi-colon and colon and end each reference with full stop after page number.

- Pachori P, Goyalwal R, Gandhi P. Emergence of antibiotic resistance *Pseudomonas aeruginosa* in intensive care unit; a critical review. *Genes Dis.* 2019; 6(2): 109-19. doi: 10.1016/j.gendis.2019.04.001.
- Hung Kn G, Fong KN. Effects of telerehabilitation in occupational therapy practice: A systematic review. *Hong Kong J Occup Ther.* 2019; 32(1): 3-21. doi: 10.1177/1569186119849119.
- Wijesooriya K, Liyanage NK, Kaluarachchi M, Sawkey D. Part II: Verification of the TrueBeam head shielding model in Varian VirtuaLinac via out-of-field doses. *Med Phys.* 2019; 46(2): 877-884. doi: 10.1002/mp.13263.
- Velayati F, Ayatollahi H, Hemmat M. A systematic review of the effectiveness of telerehabilitation interventions for therapeutic purposes in the elderly. *Methods Inf Med.* 2020; 59(2-03): 104-109. doi: 10.1055/s-0040-1713398.
- Junmee C, Siriwachirachai P, Chompoonimit A, Chanavirut R, Thaweewannakij T, Nualnetr N. Health status of patients with stroke in Ubolratana District, Khon Kaen Province: International Classification of Functioning, Disability and Health-based assessments. *Thai J Phys Ther.* 2021; 43(1): 45-63 (in Thai).

Book / Chapter in an Edited Book References

PLEASE be informed that references of books and chapter in edited book should not be include in the research article, but others manuscript categories.

- Grove SK, Ciper DJ. Statistics for Nursing Research: A Workbook for Evidence-Based Practice. 3rd Ed. St. Louis, Missouri: Elsevier; 2019.
- Perrin DH. The evaluation process in rehabilitation. In: Prentice WE, editor. Rehabilitation techniques in sports medicine. 2nd Ed. St Louis, Mo: Mosby Year Book; 1994: 253–276.

E-book

- Dehkharghani S, editor. Stroke [Internet]. Brisbane (AU): Exon Publications; 2021 [cited 2021 Jul 31]. Available from: <https://www.ncbi.nlm.nih.gov/books/NBK572004/> doi: 10.36255/exonpublications.stroke.2021.
- Tran K, Mierzwinski-Urban M. Serial X-Ray Radiography for the Diagnosis of Osteomyelitis: A Review of Diagnostic Accuracy, Clinical Utility, Cost-Effectiveness, and Guidelines [Internet]. Ottawa (ON): Canadian Agency for Drugs and Technologies in Health; 2020 [cited 2021 Jul 31]. Available from: <https://www.ncbi.nlm.nih.gov/books/NBK562943/>

Dissertation/Thesis

- Borkowski MM. Infant sleep and feeding: a telephone survey of Hispanic Americans [Dissertation]. Mount Pleasant (MI): Central Michigan University; 2002.
- On-Takrai J. Production of monoclonal antibody specific to recombinant gp41 of HIV-1 subtype E [Term paper]. Faculty of Associated Medical Sciences: Chiang Mai University; 2001 [in Thai].

Conference Proceedings

- Lake M, Isherwood J, Clansey. Determining initial knee joint loading during a single limb drop landing: reducing soft tissue errors. Proceedings of 34th International Conference of Biomechanics in Sport; 2016 Jul 18-22; Tsukuba, Japan, 2016. Available from: <https://ojs.ub.uni-konstanz.de/cpa/article/view/7126>.
- Ellis MD, Carmona C, Drogos J, Traxel S, Dewald JP. Progressive abduction loading therapy targeting flexion synergy to regain reaching function in chronic stroke: preliminary results from an RCT. Proceedings of the 38th Annual International Conference of the IEEE Engineering in Medicine and Biology Society; 2016: 5837-40. doi: 10.1109/EMBC.2016.7592055.

Government Organization Document

- Australian Government, Department of Health. Physical activity and exercise guidelines for all Australian. 2021 [updated 2021 May 7; cited 15 Jul 2021]. Available from: <https://www.health.gov.au/health-topics/physical-activity-and-exercise/physical-activity-and-exercise-guidelines-for-all-australians>.
- Department of Health. Situation survey on policy and implementation of physical activity promotion in schools for first year 2005. (in Thai). Nonthaburi: Ministry of Public Health; 2005.
- Department of Local Administration, Ministry of Interior Affairs. Standard of Sports Promotion. (in Thai). Bangkok. 2015:7–9.
- World Health Organization. WHO guidelines on physical activity and sedentary behaviour. Geneva: World Health Organization; 2020. Licence: CC BY-NC-SA 3.0 IGO.

Journal History

Established in 1968

- 1968-2016 As the Bulletin of Chiang Mai Associated Medical Sciences
 - Vol1, No1 - Vol.49, No3
- 2017, the Journal of Associated Medical Sciences
 - Vol.50, No1 and forward.

Journal Sponsorship Publisher

Faculty of Associated Medical Sciences, Chiang Mai University

Sponsors

Faculty of Associated Medical Sciences, Chiang Mai University

Sources of support

Faculty of Associated Medical Sciences, Chiang Mai University

